22. Review of Some Fundamentals of Data Processing

This chapter is devoted to reviewing some fundamental transforms and analysis procedures commonly used for both signal and data processing in fluid mechanics measurements. The chapter begins with a brief review of the Fourier transform and its digital counterpart the discrete Fourier transform. In particular its use for estimating power spectral density is discussed in detail. This is followed by an introduction of the correlation function and its relation to the Fourier transform. The Hilbert transform completes the introductory topics. The chapter then turns to a rigorous presentation of the proper orthogonal decomposition (POD) in the context of the approximation theory and as an application of singular value decomposition (SVD). The relationship between POD and SVD is discussed and POD is described in a statistical setting using an averaging operation for use with turbulent flows. The different POD approaches are briefly introduced, whereby the main differences between the classical POD and the snapshot POD are highlighted. This section closes with a presentation of the POD as a generalization of the classical Fourier analysis to inhomogeneous directions. The chapter continues with a discussion of conditional averages and stochastic estimation as a means of studying coherent structures in turbulent flows before moving in a final section to a comprehensive discussion of wavelets as a combination of data processing in time and frequency domain. After first introducing the continuous wavelet transform and orthogonal wavelet transform their application in experimental fluid mechanics is illustrated through numerous examples.

22.1 Fourier Transform

The Fourier transform (FT) is an integral transform with orthogonal sinusoidal basis functions of different frequencies. The result represents the frequency spectrum of the signal. Depending on the characteristics of the original (time) signal, different variants of the transform are defined.

A continuous periodic signal $x(t) = x(t+T)$ with the period T can be decomposed into an infinite series

of sinusoidal functions (*Fourier series*), whose linear combination reproduces the original function

$$x(t) = x(t+T) = \sum_{k=-\infty}^{\infty} a_k \cos\left(\frac{2\pi kt}{T}\right) + \sum_{k=-\infty}^{\infty} b_k \sin\left(\frac{2\pi kt}{T}\right) . \tag{22.1}$$

The Fourier coefficients a_k and b_k are given by

$$a_k = \frac{1}{T}\int_0^T x(t)\cos\left(\frac{2\pi kt}{T}\right) \mathrm{d}t ,$$

$$b_k = \frac{1}{T}\int_0^T x(t)\sin\left(\frac{2\pi kt}{T}\right) \mathrm{d}t . \tag{22.2}$$

Using

$$\mathrm{e}^{\mathrm{i}x} = \cos(x) + \mathrm{i}\sin(x) , \tag{22.3}$$

the Fourier coefficients a_k and b_k can be combined to a complex value $\underline{c}_k$ and the Fourier series can be extended easily for complex function $\underline{x}(t)$ yielding

$$\underline{x}(t) = \underline{x}(t+T) = \sum_{k=-\infty}^{\infty} \underline{c}_k \exp\left(\frac{2\pi \mathrm{i}kt}{T}\right) \tag{22.4}$$

with

$$\underline{c}_k = \frac{1}{T}\int_0^T \underline{x}(t)\exp\left(-\frac{2\pi \mathrm{i}kt}{T}\right) \mathrm{d}t . \tag{22.5}$$

Note that, even for a real function $x(t)$, the Fourier coefficients are complex values. The real part is associated with the cosine function and the imaginary part with the sine function. Thus, the real part represents contributions to the signal, which are symmetric about zero and the imaginary part describes the asymmetric contributions.

By using $T \to \infty$, for a continuous complex signal $\underline{x}(t)$ with finite energy content the superposition of the Fourier series becomes

$$\underline{x}(t) = \int_{-\infty}^{\infty} \underline{X}(f)\exp(2\pi \mathrm{i}ft)\,\mathrm{d}f \tag{22.6}$$

with

$$\underline{X}(f) = \int_{-\infty}^{\infty} \underline{x}(t)\exp(-2\pi \mathrm{i}ft)\,\mathrm{d}t . \tag{22.7}$$

Signal with finite energy fulfill $\int_{-\infty}^{\infty} |\underline{x}(t)|\,\mathrm{d}t < \infty$. This implies that the signal is nonperiodic.

The result of the decomposition $\underline{X}(f)$ is called the *continuous Fourier transform* (CFT). It is a continuous, infinite, non-periodic, complex frequency spectrum, which fulfills the Plancherel theorem

$$\int_{-\infty}^{\infty} |\underline{X}(f)|^2\,\mathrm{d}f = \int_{-\infty}^{\infty} |\underline{x}(t)|^2\,\mathrm{d}t , \tag{22.8}$$

indicating the conservation of energy by the Fourier transform. Note that upper- and lower-case notation will be used for the frequency and time domains, respectively.

A finite series of complex values $\underline{x}_n = x(t = n\Delta t_\mathrm{s})$ with $n = 0,\ 1, \ldots ,\ N-1$, sampled at equal time intervals and over the time duration $0 \le t < T = N\Delta t_\mathrm{s}$ can be decomposed into a finite sum of complex Fourier coefficients $\underline{X}_k$, yielding the discrete Fourier transform (DFT). The DFT is defined as

$$\underline{X}_k = \underline{X}(f = k\Delta f) = \mathrm{FT}(\underline{x}_n) = \sum_{n=0}^{N-1} \underline{x}_n \exp\left(-\mathrm{i}\frac{2\pi nk}{N}\right)$$
$$k = 0,\ 1, \ldots ,\ (N-1) \tag{22.9}$$

and its inverse transform as

$$\underline{x}_n = \mathrm{FT}^{-1}\{\underline{X}_k\} = \frac{1}{N}\sum_{k=0}^{N-1} \underline{X}_k \exp\left(+\mathrm{i}\frac{2\pi nk}{N}\right) ,$$
$$n = 0,\ 1, \ldots ,\ (N-1) , \tag{22.10}$$

where n is the data sample index at time intervals of Δt_s and with the corresponding sample frequency of f_s. The spectral coefficients are computed for the equally spaced frequencies given by

$$f_k = \frac{k}{N\Delta t_\mathrm{s}} = \frac{kf_\mathrm{s}}{N} , \quad k = 0,\ 1, \ldots ,\ (N-1) . \tag{22.11}$$

The frequency spacing of the resulting Fourier coefficients is therefore

$$\Delta f_\mathrm{s} = \frac{1}{N\Delta t_\mathrm{s}} = \frac{1}{T} = \frac{f_\mathrm{s}}{N} . \tag{22.12}$$

This is also the lowest frequency that can be resolved.

The power spectral density (PSD) is given by the squared magnitude of the spectral coefficients

$$S_k = S(f = f_k) = \frac{1}{Nf_\mathrm{s}}\underline{X}_k^*\underline{X}_k = \frac{1}{Nf_\mathrm{s}}|\underline{X}_k|^2 ,$$
$$k = 0,\ 1, \ldots ,\ (N-1) . \tag{22.13}$$

This function represents the distribution of the total signal power between the frequencies 0 and f_s. The

term density is used because power per frequency bandwidth Δf_s is being considered. The PSD is symmetric about $k = N/2$ and has a periodicity every N samples. Therefore, an alternative representation is the use of negative and positive frequencies. For this case, all values of $k \geq N/2$ are interpreted as negative frequency values and the spectrum is symmetric about $k = 0$. In this case, the function is known as the two-sided spectrum. The one-sided PSD simply considers the symmetry of the two-sided spectrum around 0 and yields the spectral distribution between $k = 0$ and $k = N/2$. It is given by

$$G_k = G(f = f_k) = \frac{2}{N f_s} \underline{X}_k^* \underline{X}_k = \frac{2}{N^2 \Delta f_s} \underline{X}_k^* \underline{X}_k \,,$$
$$k = 0, 1, \ldots, \frac{N}{2} \,. \qquad (22.14)$$

Note that the total power of this spectrum is not the same because $f = 0$ and $f = f_s/2$ are also doubled.

The maximum resolvable frequency is half the sampling frequency $f_{max} = f_s/2 = f_{N/2}$ (the Nyquist frequency) and the resolution is determined by the data set duration $\Delta f_s = 1/T$. Graphically the PSD and the parameters involved in computing it are shown in Fig. 22.1.

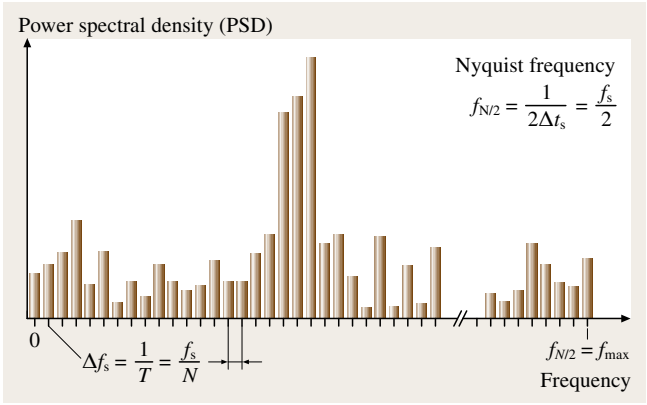

Fig. 22.1 The power spectral density and the sampling parameters

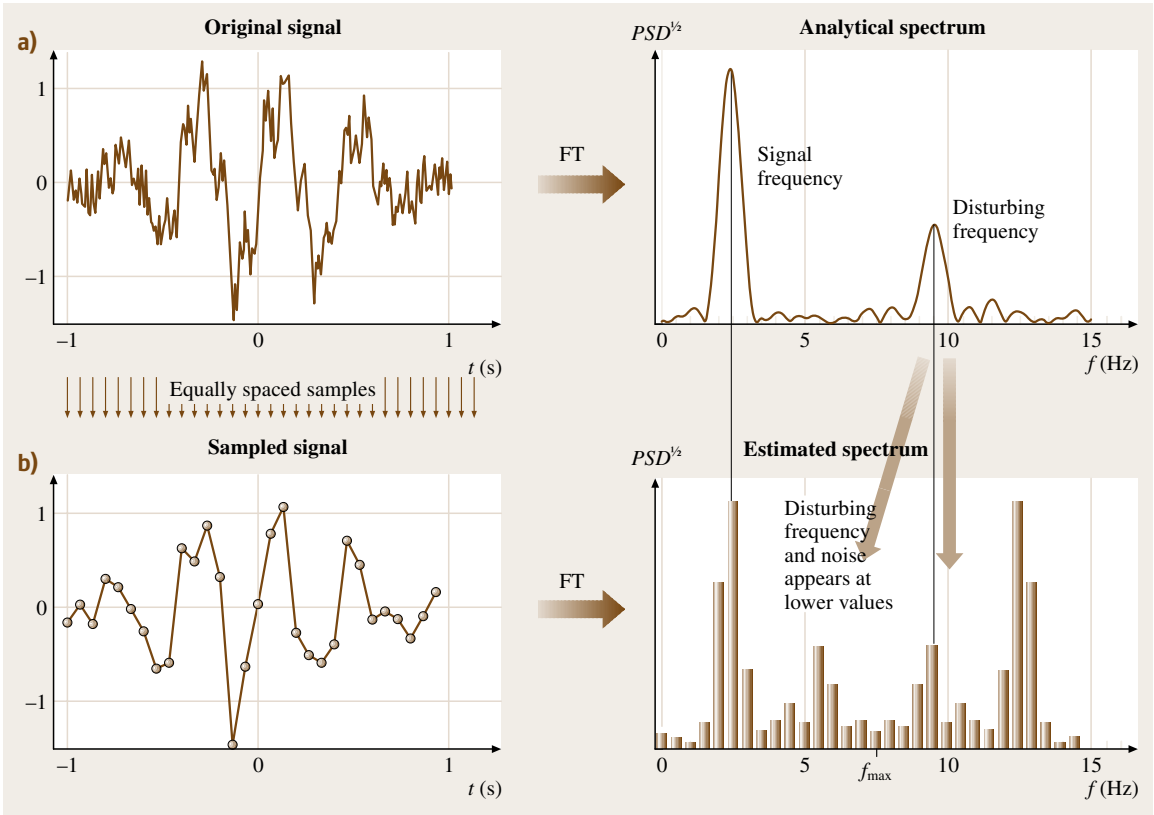

Fig. 22.2a,b Aliasing error in a spectrum due to signal frequencies occurring above the Nyquist frequency. **(a)** Original signal and spectrum, **(b)** sampled signal and falsified spectrum

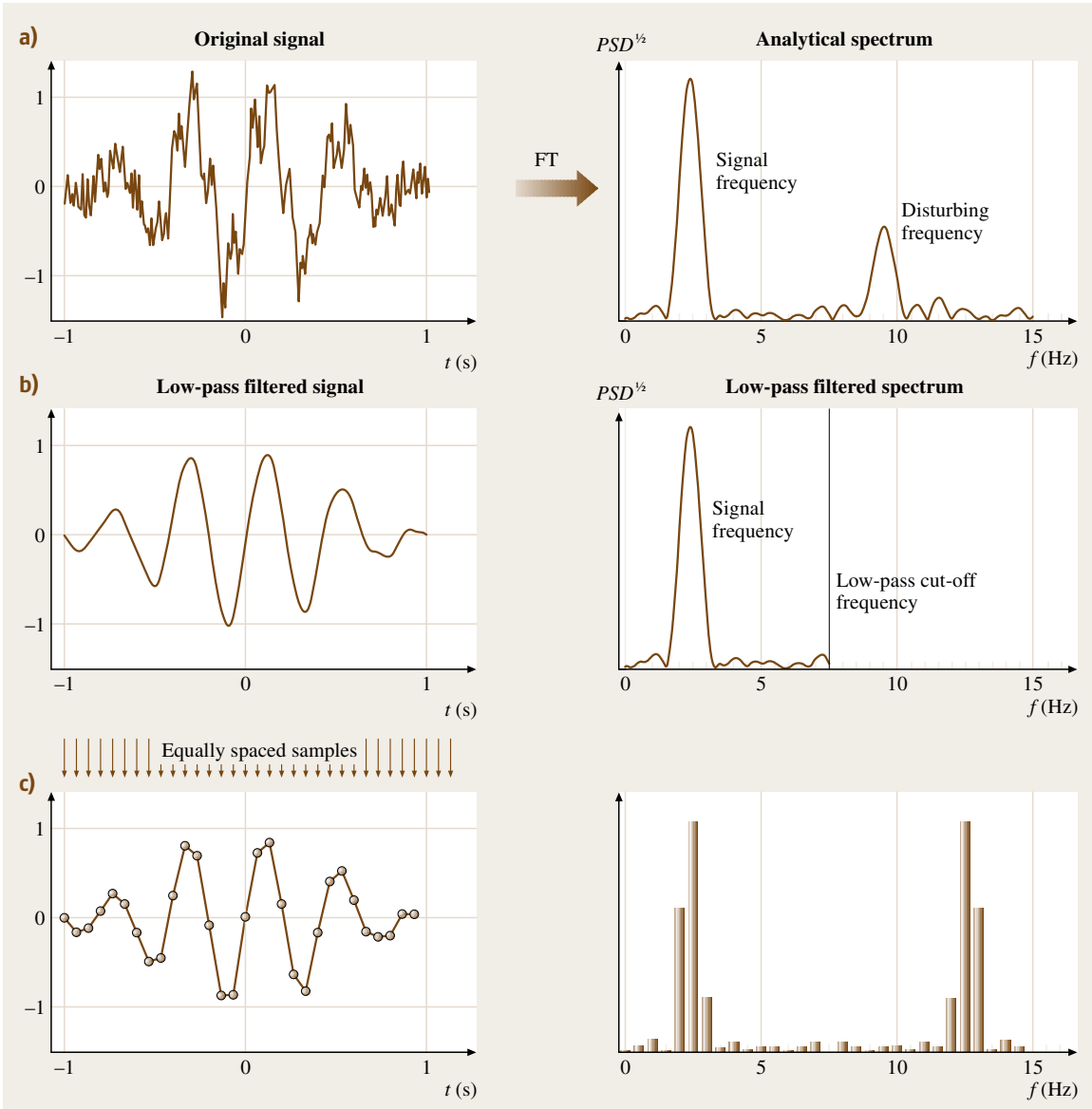

Fig. 22.3a–c Elimination of the aliasing error by use of a low-pass, anti-aliasing filter. **(a)** Original signal and spectrum, **(b)** low-pass filtered signal and spectrum, **(c)** sampled signal and non-aliased spectrum

Two properties of the DFT deserve particular attention. Since the time between the sample points is not infinitely small, the power in the signal at frequencies above f_{max} will appear in the PSD at lower frequencies, an effect known as aliasing. This falsifies the spectrum at the lower frequencies. An example of aliasing is given in Fig. 22.2. The signal in Fig. 22.2a contains two frequency peaks at 2.4 Hz and 9.5 Hz, as can be seen in the correct spectrum illustrated in Fig. 22.2a. By sampling the signal at 15 Hz, the maximum resolvable frequency is 7.5 Hz and thus, the Nyquist criterion is not fulfilled for the signal power at 9.5 Hz. The spectral portion above 7.5 Hz is mirrored about the Nyquist frequency and results in an additional peak at 5.5 Hz (Fig. 22.2b). Furthermore the signal noise at frequencies above f_{max} also increases the noise level at frequencies below f_{max}.

Aliasing errors in estimates of PSD are avoided by applying an analog anti-aliasing, low-pass filter with a sharp cut-off at half the sampling frequency. This procedure is illustrated in Fig. 22.3, using the same signal as used in Fig. 22.2. Before sampling the signal, a low-pass filter removes the frequencies higher than the Nyquist frequency f_{max} (Fig. 22.3b). The spectrum of the filtered and sampled signal in Fig. 22.3c contains no additional frequency peak. Furthermore, the noise level is reduced to the same as in the original signal in Fig. 22.3a.

Besides the periodicity after every N samples of the DFT in (22.9) and the PSD in (22.13), the inverse DFT in (22.10) also has a period of N samples. This effectively means that the DFT perceives and acts on an infinite juxtaposition of the input data record and the inverse DFT effectively transforms an infinite juxtaposition of the spectrum. This is illustrated in Fig. 22.4 for a time series.

If the beginning and end of the record do not merge smoothly into one another, sudden amplitude jumps are perceived, which give rise to additional frequency components in the spectrum. These *end effects* are unimportant for records of long duration; however, they deserve attention with short records. These effects are diminished by applying window functions in the time domain. Window functions scale the input data amplitude and force a tapering to zero at the beginning and end of the signal [22.1].

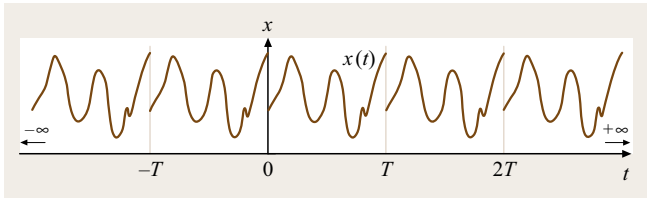

Fig. 22.4 Implicit periodicity of acquired signal when processing using the finite-length DFT

A further consequence of a finite input record duration is spectral broadening. A spectrum of an infinitely long sine wave is a delta function at the signal frequency. A finite-length sine wave yields however a broadened peak, in which the peak width is inversely proportional to the input signal duration. This process is graphically illustrated in Fig. 22.5. The spectrum of an infinite sine wave is a delta function at the signal frequency (Fig. 22.5a). A finite duration sine wave can be viewed as the product of an infinite sine wave with a rectangular window of duration T (Fig. 22.5b). The spectrum of

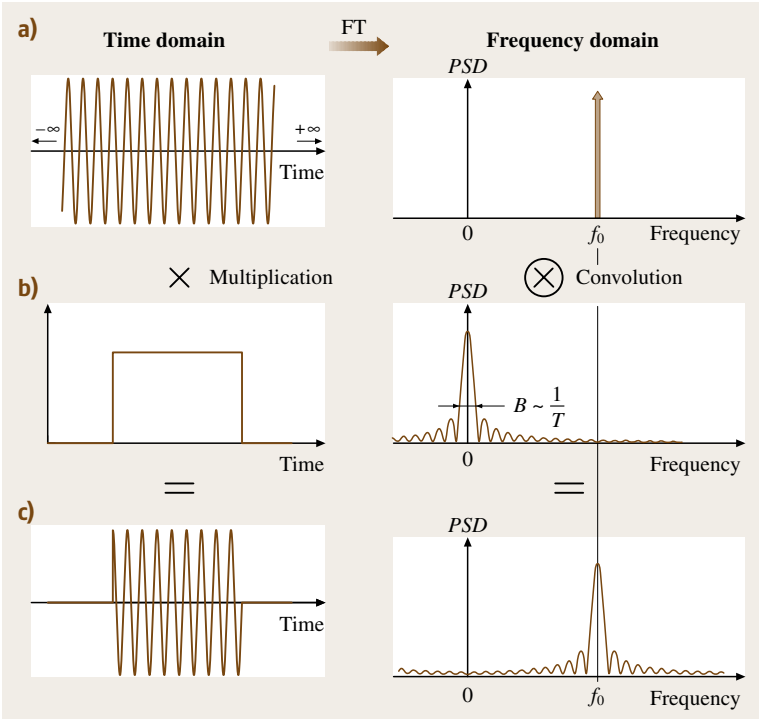

Fig. 22.5a–c A multiplication of two signals in the time domain is equivalent to a convolution in the frequency domain. This can be used to explain spectral broadening due to finite record lengths. **(a)** Infinite sine function and related spectrum, **(b)** rectangular function and related spectrum, **(c)** finite sine function and related spectrum

the finite sine wave will therefore be the convolution of the delta function with the magnitude of a sinc function, the transform of a rectangular window (Fig. 22.5c).

This can be easily illustrated using the following relations. If a signal $y(t)$ is given in the time domain as the product of two other signals, $x(t)$ and $h(t)$

$$y(t) = x(t)h(t) \tag{22.15}$$

then the Fourier transform of $y(t)$ is given by the convolution of the Fourier transforms of $x(t)$ and $h(t)$ [22.2].

$$\underline{Y}(f) = \underline{X}(f) \otimes \underline{H}(f) = \int_{-\infty}^{\infty} \underline{X}(\alpha) H(f-\alpha)\,\mathrm{d}\alpha\,. \tag{22.16}$$

The power spectral density of $y(t)$ is then

$$S_k = \frac{1}{N f_s} \underline{Y}_k^* \underline{Y}_k\,, \quad k = 0, 1, \ldots, (N-1)\,. \tag{22.17}$$

An obvious consequence of spectral broadening is that the resolution of distinct signal frequencies in the PSD can be improved by sampling a longer portion of the signal.

In practical implementations of the DFT, (22.9) is not used directly but rather a recursive form known as the fast Fourier transform (FFT) is used. There are many realizations of the FFT, but they share one feature in common, namely, that they normally operate on 2^n points: sample records are restricted to values such as 16, 32, 64, 128, ... The calculation time of the DFT implemented with (22.9) increases with N^2. The FFT algorithm reduces the computation time to the order of $N \log N$. Algorithms exist for FFTs using other record lengths, especially prime number decompositions; however, these are not in widespread use.

A commonly used technique with the FFT is that of zero padding. Without changing the spectral content of the signal, zero padding forces the FFT algorithm to estimate the spectrum at additional frequencies between zero and $f_{\max}$, thus improving the resolution. This is easily seen by examining a signal doubled in length by adding zeros. Instead of (22.9) the transform becomes

$$\underline{X}_k = \sum_{n=0}^{2N-1} \underline{x}_n \exp\left(-\mathrm{i}\frac{2\pi nk}{2N}\right),$$
$$k = 0, 1, \ldots, (2N-1)\,. \tag{22.18}$$

However, since $\underline{x}_n = 0$ for $n = N, N+1, \ldots, (2N-1)$, this can be written as

$$\underline{X}_k = \sum_{n=0}^{N-1} \underline{x}_n \exp\left(-\mathrm{i}\frac{2\pi n\,(k/2)}{N}\right),$$
$$k = 0, 1, \ldots, (2N-1) \tag{22.19}$$

which is identical to the N-point transform for every other k value. However now $\underline{X}_k$ is also computed at intermediate k values. The spectral content of the signal has in no way been altered, but with the intermediate estimates, interpolation of peak locations can be improved. Zero padding can also be used to extend input data records up to a length of 2^n values, in preparation for an FFT.

22.2 Correlation Function

The (temporal) autocorrelation function of a signal $x(t)$ is defined as

$$R(\tau) = E[x(t)x(t+\tau)]\,. \tag{22.20}$$

It is a symmetric function. Principally, the information available in spectral domain is also available in the correlation domain, since the autocorrelation function $R(\tau)$ forms a Fourier transform pair with the power spectral density (Wiener–Khinchine relation).

$$S(f) = \mathrm{FT}\{R(\tau)\} = \int_{-\infty}^{\infty} R(\tau)\,\mathrm{d}\tau\,, \tag{22.21}$$

$$R(\tau) = \mathrm{FT}^{-1}\{S(f)\} = \int_{-\infty}^{\infty} S(f)\,\mathrm{d}f\,. \tag{22.22}$$

In digital form this can be expressed as

$$R_n = R(\tau = n\Delta\tau) = \frac{f_s}{N} \sum_{k=0}^{N-1} S_k \exp\left(+\mathrm{i}\frac{2\pi nk}{N}\right),$$
$$n = 0, 1, \ldots, N-1\,, \tag{22.23}$$

$$S_k = S(f = f_k) = \frac{1}{f_s} \sum_{n=0}^{N-1} R_n \exp\left(-\mathrm{i}\frac{2\pi kn}{N}\right),$$
$$k = 0, 1, \ldots, N-1\,, \tag{22.24}$$

where $\Delta\tau = \Delta t_s$ is the time lag interval. The autocorrelation function is by definition symmetric about $\tau = 0$, as the auto spectral density is about $f = 0$, yielding the

alternative expressions

$$
\begin{aligned}
R_n &= R(\tau = n\Delta\tau) \\
&= \frac{f_s}{2N} \sum_{k=-N/2}^{N/2-1} G_{|k|} \exp\left(+\mathrm{i}\frac{2\pi nk}{N}\right) \\
&= \frac{f_s}{2N}\left[G_0 + (-1)^n G_{N/2} \right. \\
&\quad \left. + 2\sum_{k=1}^{N/2-1} G_k \cos\left(\frac{2\pi nk}{N}\right)\right], \\
n &= 0, 1, \ldots, \frac{N}{2}, \qquad (22.25)
\end{aligned}
$$

$$
\begin{aligned}
G_k &= G(f = f_k) \\
&= \frac{2}{f_s} \sum_{n=-N/2}^{N/2-1} R_{|n|} \exp\left(-\mathrm{i}\frac{2\pi kn}{N}\right) \\
&= \frac{2}{f_s}\left[R_0 + (-1)^k R_{N/2} \right. \\
&\quad \left. + 2\sum_{n=1}^{N/2-1} R_n \cos\left(-\frac{2\pi kn}{N}\right)\right], \\
k &= 0, 1, \ldots, \frac{N}{2}. \qquad (22.26)
\end{aligned}
$$

With the mean removed, the autocorrelation function is known as the autocovariance function; however, these two terms will be used interchangeably, always assuming a mean-free input signal.

A computation of R_n using the FFT, first to compute the PSD and then to transform to the correlation domain, exhibits a speed advantage that increases with increasing data record length $N \log N$ compared to N^2 for a direct calculation of the correlation function shown below. However, there are some subtle drawbacks of using the estimate of (22.25). The most important of these is the so-called wrap-around error [22.2], which has its origins in the finite-length DFT, (22.9). The inherent periodicity in time, which is implied by (22.9) and illustrated in Fig. 22.4, essentially means that the correlation function computed according to (22.25) assumes an infinite juxtaposition of the input signal in time. The derived autocorrelation function will also be based on this assumption and is, therefore, known as the circular autocorrelation. This error is avoided by first padding the input signal with zeros at the beginning and end of the original signal to double its length.

The autocorrelation function will exhibit a periodicity at the same period as the original signal. For instance, the autocorrelation of an infinite sine wave will be an infinite cosine wave, as illustrated in Fig. 22.6a. Thus, the signal frequency can be estimated by measuring the elapsed time over one or more zero crossings of the autocorrelation function (period timing).

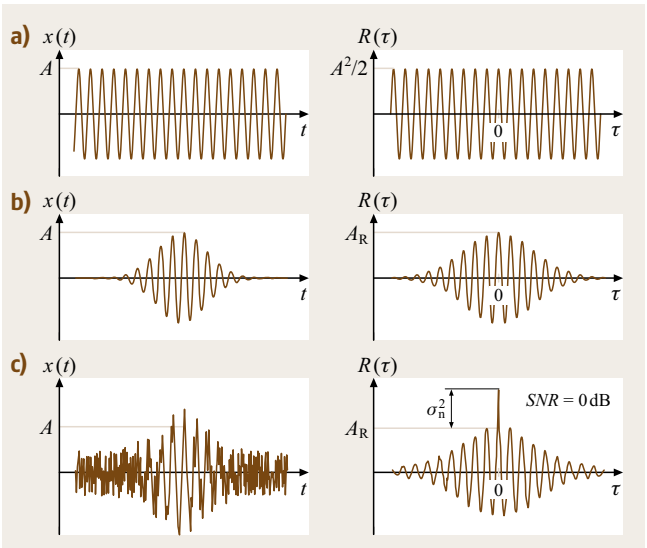

Fig. 22.6a–c Input signal and autocorrelation function. **(a)** Sine wave, **(b)** noise-free Doppler signal, **(c)** noisy Doppler signal

The autocorrelation of a Gaussian-windowed sine wave centered around $t = 0$, as shown in Fig. 22.6b, will yield as a correlation function a cosine wave with an amplitude decay directly related to the window width. Of particular interest is the effect of signal noise on the correlation function. As illustrated in Fig. 22.6c, the contribution of signal noise can be found entirely in the first coefficient of the autocorrelation function, i. e., at $\tau = 0$. This is because the signal noise has no inherent time scale, meaning that it is completely random and not correlated with itself over any length of time. This last property of the autocorrelation function is particularly interesting for signal processing, because it provides a means of separating the noise effects from the signal, thus, improving the estimation of signal frequency and other signal parameters.

The correlation function can also be computed directly. The estimator

$$
\begin{aligned}
R_n &= R(n\Delta\tau) = \frac{1}{N}\sum_{i=0}^{N-1} x_i x_{i+n}, \\
n &= 0, 1, \ldots, (N-1) \qquad (22.27)
\end{aligned}
$$

with periodic boundary conditions ($x_{n\pm N} = x_n$) yields the same estimate of the correlation function as obtained

with the FFT. Due to the assumption of the periodicity of the signal, it has systematic errors, as described above. The estimator

$$R_n = R(n\Delta\tau) = \frac{1}{N}\sum_{i=0}^{N-n-1} x_i x_{i+n} \,,$$
$$n = 0, 1, \ldots, (N-1) \qquad (22.28)$$

is equivalent to the FFT-based estimation with zero padding (doubling the signal length). This estimator has systematic errors due to the decreasing number of products in the sum for increasing time lags $n\Delta\tau$, while the sum is always divided by N. Dividing the sum by the number of products in the sum yields the estimator

$$R_n = R(n\Delta\tau) = \frac{1}{N-n}\sum_{i=0}^{N-n-1} x_i x_{i+n} \,,$$
$$n = 0, 1, \ldots, (N-1) \,, \qquad (22.29)$$

which is unbiased. On the other hand, this estimator has a time-lag-dependent estimation variance, which increases with time lag. The alternative estimator

$$R_n = R(n\Delta\tau) = \frac{\sum_{i=0}^{N-1} x_i^2 \sum_{i=0}^{N-n-1} x_i x_{i+n}}{\sqrt{\sum_{i=0}^{N-n-1} x_i^2}\sqrt{\sum_{i=0}^{N-n-1} x_{i+n}^2}} \,,$$
$$n = 0, 1, \ldots, (N-1) \qquad (22.30)$$

first calculates the correlation coefficient using a normalization with estimates of the variance based on the same x_i as used for the summation with products $x_i x_{i+n}$. Then the correlation coefficient is denormalized to a correlation function using a variance estimate based on all available signal samples. This estimator has a small estimation variance. However, this estimator is only asymptotically bias-free for a sufficiently large N.

22.3 Hilbert Transform

The Hilbert transform of a function $x(t)$ is defined by

$$y(t) = \mathrm{HT}\{x(t)\} = \frac{1}{\pi}\int_{-\infty}^{\infty} \frac{x(\tau)}{t-\tau}\,\mathrm{d}\tau \qquad (22.31)$$

and is an integral transform, where the Cauchy principal value is taken in the integral. The function $y(t)$ is produced by passing $x(t)$ through a filter with the transfer function

$$H(f) = -\mathrm{i}\,\mathrm{sgn}(f) \,. \qquad (22.32)$$

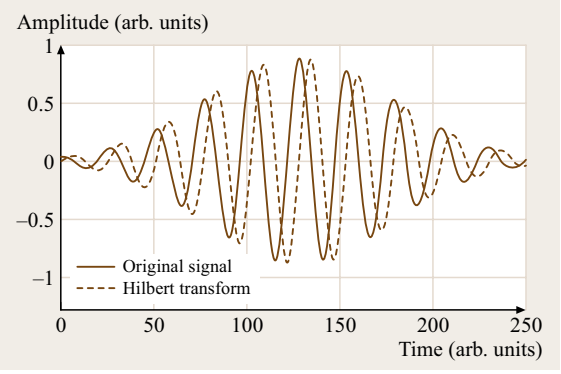

Fig. 22.7 A sample signal and its Hilbert transform illustrating the −90° phase shift

A singularity exists at the value $f = 0$, which, however, does not cause any computational problems. On the other hand, the infinite integral causes problems for signals that are not mean-free. Thus, when processing signals with the Hilbert transform, it is necessary first to remove the mean.

The magnitude and phase of $H(f)$ are

$$|H(f)| = 1 \,, \qquad (22.33)$$
$$\arg\{H(f)\} = -\frac{\pi}{2}\mathrm{sgn}(f) \,. \qquad (22.34)$$

The inverse of the Hilbert transform is given by

$$x(t) = \mathrm{HT}^{-1}\{y(t)\} = -\mathrm{HT}\{y(t)\} = \frac{1}{\pi}\int_{-\infty}^{\infty} \frac{y(\tau)}{\tau - t}\,\mathrm{d}\tau \,. \qquad (22.35)$$

Table 22.1 Some sample Hilbert transform pairs

$x(t)$	$y(t) = \mathrm{HT}\{x(t)\}$
Const.	Defined as 0
$ax_1(t) + bx_2(t)$	$ay_1(t) + by_2(t)$
$x(at)$	$y(at)$
$x(t - t_0)$	$y(t - t_0)$
$\int_{-\infty}^{\infty} x(t)x(t-\tau)\,\mathrm{d}t$	$\int_{-\infty}^{\infty} y(t)y(t-\tau)\,\mathrm{d}t$
$a\sin bt$	$-a\cos bt$
$a\cos bt$	$a\sin bt$
$\delta(t-a)$	$\frac{1}{\pi}\frac{1}{t-a}$

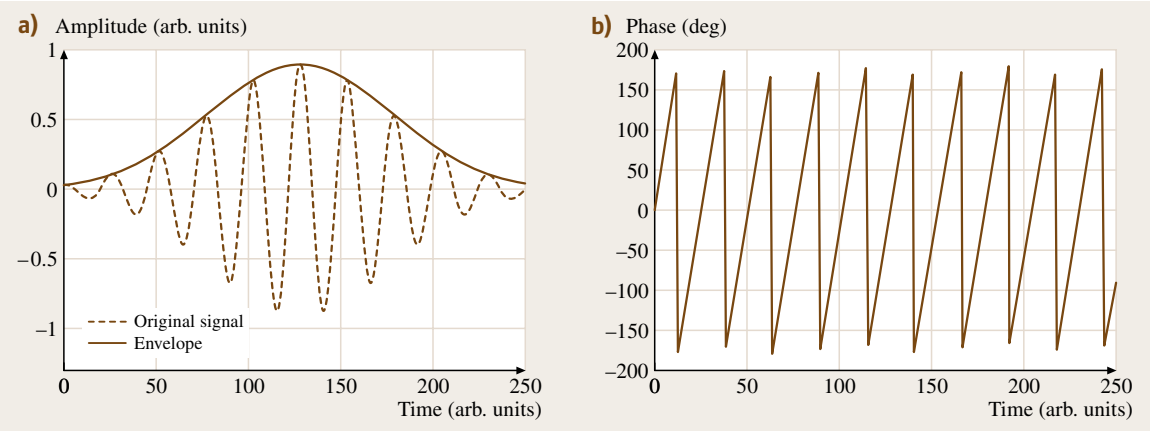

Fig. 22.8 **(a)** Input signal and computed envelope amplitude, **(b)** instantaneous phase of the input signal

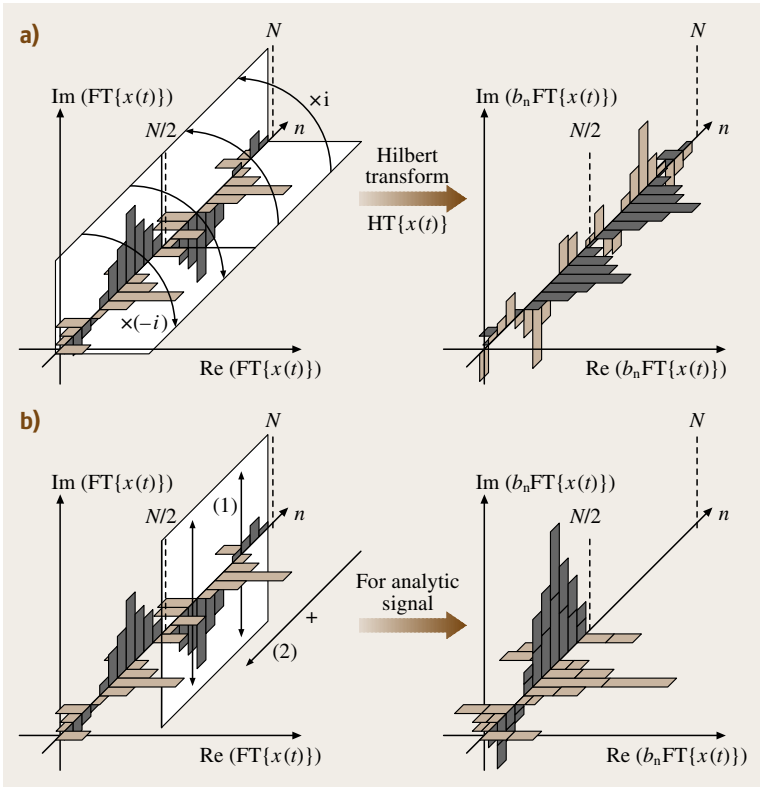

Fig. 22.9 **(a)** Fourier coefficients modified for the Hilbert transform, **(b)** modified coefficients for analytical signal

Some typical examples of Hilbert transform pairs are given in Table 22.1.

A sample signal and its Hilbert transform are shown in Fig. 22.7. For a given input signal $x(t)$ the Hilbert transform is the signal $y(t)$ shifted by $-90°$ in phase for all frequencies.

An analytical (complex) function for a given input signal $x(t)$ can be defined as

$$\underline{z}(t) = x(t) + \mathrm{iHT}\{x(t)\}\,, \tag{22.36}$$

which has spectral values only for frequencies larger than or equal to zero ($f \geq 0$). Its Fourier transform is zero

for all negative frequencies, or in the discrete case for all frequencies $f \geq N/2$. This analytical signal can be used to derive the signal envelope $A(t)$ and the instantaneous signal phase $\varphi(t)$,

$$A(t) = |\underline{z}(t)| \,, \tag{22.37}$$

$$\varphi(t) = \arg\{\underline{z}(t)\} \,. \tag{22.38}$$

The envelope and phase of the Doppler-like signal from Fig. 22.7 are shown in Fig. 22.8.

The calculation of the Hilbert transform for a discrete signal of finite length $x_n = x(t = t_n)$, $t_n = n/f_s$, $n = 0, 1, \ldots, (N-1)$ can be performed in the frequency domain using the discrete Fourier transform or its fast implementation, the FFT

$$\aleph\{x_n\} = \mathrm{FT}^{-1}\{b_n \mathrm{FT}\{x_n\}\} \tag{22.39}$$

with

$$b_n = \begin{cases} -\mathrm{i} & \text{for } 0 \leq n < N/2 \\ \mathrm{i} & \text{for } N/2 \leq n < N \,. \end{cases} \tag{22.40}$$

The analytical signal defined in (22.36) can be obtained as

$$\underline{z}_n = \underline{z}(t = t_n) = \mathrm{FT}^{-1}\{b_n \mathrm{FT}\{x_n\}\} \tag{22.41}$$

with

$$b_n = \begin{cases} 2 & \text{for } 0 \leq n < N/2 \\ 0 & \text{for } N/2 \leq n < N \end{cases} \,. \tag{22.42}$$

These expressions are illustrated graphically in Fig. 22.9, in which the real and imaginary Fourier coefficients of a real input signal are shown. The modified coefficients used in the inverse transform to obtain the Hilbert transform (22.39) are shown in Fig. 22.9a, and the modified coefficients used in the inverse transform to obtain the analytical function (22.41) are shown in Fig. 22.9b. From this figure it becomes apparent that the Hilbert transform can be implemented using very simple operations in combination with the Fourier transform.

22.4 Proper Orthogonal Decomposition: POD

22.4.1 Basics

Collecting very large amounts of data by numerical simulations or experimental approaches is a common situation in almost any scientific field. There is therefore a great need to have specific postprocessing techniques able to extract from these large quantities of high-dimensional data, synthetic information essential to understand and eventually to model the processes under study. The proper orthogonal decomposition (POD) is one of the most powerful method of data analysis for multivariate and non linear phenomena. Essentially, POD is a linear procedure that takes a given collection of input data and creates an orthogonal basis constituted by functions estimated as the solutions of an integral eigenvalue problem known as a Fredholm equation (22.60). These eigenfunctions are by definition (22.58) characteristic of the most probable realizations of the input data. Moreover, it can be shown that they are optimal in terms of representation of the energy present within the data (Sect. 22.4.3).

Historical Background of POD

Historically, the proper orthogonal decomposition was introduced in the context of turbulence by *Lumley* [22.3] as an objective definition of what was previously called *big eddies* by *Townsend* [22.4] and which is now widely known as coherent structures (CS, see [22.5] for a detailed discussion of CS and an overview of their detection methods). According to Yaglom [22.6], the POD is a natural idea to replace the usual Fourier decomposition in nonhomogeneous directions. The POD method was then introduced for different purposes independently by several scientists, in particular, by *Kosambi* [22.7], *Loève* [22.8, 9], *Karhunen* [22.10], *Pougachev* [22.11], and *Obukhov* [22.12, 13]. This technique then became known under a variety of names: Karhunen–Loève decomposition or expansion, principal component analysis [22.14] or hotelling analysis [22.15], and singular value decomposition [22.16]. Naturally, the proper orthogonal decomposition has been used widely in studies of turbulence but other popular applications involve random variables [22.17], image processing such as characterization of human faces [22.18], signal analysis [22.19], data compression [22.20], and more recently optimal control [22.21, 22].

From a mathematical point of view, the proper orthogonal decomposition is just a transformation that diagonalizes a given matrix A and brings it to a canonical form $A = U \Sigma V^{\dagger}$, where Σ is a diagonal matrix (see the

paragraph on *singular value decomposition* for a complete description). The mathematical content of POD is therefore classical and is based on the spectral theory of compact, self-adjoint operators [22.23]. Two geometric interpretations of this mathematical procedure are discussed later.

POD and Turbulent Flows

A complete literature review on applications of POD to turbulence is far beyond the scope of this handbook: good reviews can be found in *Holmes* et al. [22.24], *Delville* et al. [22.25] and in the appendix of *Gordeyev* [22.26]. In the following, we provide a brief reminder of the insight that can be gained from the use of POD for eduction and modeling of the coherent structures observed in most turbulent flows.

For our purposes, it is sufficient to bear in mind [22.27] that CS identification has to be done for at least two reasons: firstly, from an energetic point of view because the relative energy content of the CS compared with the total turbulent energy can be from 10% (for boundary layers, far jets) up to 20% (far wakes, plane mixing layers) or 25% (near wakes or jets) [22.28]; secondly, because the dynamical properties of CS play an essential role in mixing processes, drag, noise emission, etc. For these reasons, the idea of controlling turbulent flows by means of influencing their coherent structures seems promising [22.29, 30].

Several characteristics of the proper orthogonal decomposition technique, as introduced by *Lumley* [22.3], are quite attractive in terms of CS identification. Firstly, compared to many other classical methods used for large-scale identification (flow visualization, conditional methods, VITA (Variable Integration Time Average), pattern recognition analysis), no a priori is needed for the eduction scheme. CS are defined in an objective and unique manner as the flow realization that possesses the largest projection onto the flow field (22.58). Secondly, the POD yields an optimal set of basis functions in the sense that no other decomposition of the same order captures an equivalent amount of kinetic energy. Up to now, POD is only presented as a data analysis method that takes as input an ensemble of data, obtained from physical experiments or from detailed numerical simulations, and extracts basis functions optimal in terms of the representativeness of the data. For illustrative purposes of the ability of the proper orthogonal decomposition to educe CS, POD is applied in *Cordier* and *Bergmann* [22.31] to a database obtained by large-eddy simulation of a three-dimensional plane turbulent mixing layer. However, proper orthogonal decomposition can also be used as an efficient procedure to compute low-dimensional dynamical models of the CS. Reduced-order modeling by POD is based on projecting the governing equation of motion onto subspaces spanned by the POD basis functions (Galerkin projection) yielding a simple set of ordinary differential equations (ODEs). Finally, due to the optimality of convergence in terms of kinetic energy of the POD functions, only a small number of POD modes are necessary to represent the dynamical evolution of the flow correctly. Reduced-order modeling based on POD has recently received an increasing amount of attention for applications to optimal control problems for partial differential equations [22.32–35]. In *Cordier* and *Bergmann* [22.31], a low-order model based on POD is developed for the incompressible unsteady wake flow behind a circular cylinder at a Reynold's number of 200. In particular, it was demonstrated how the control action could be incorporated into the low-dimensional model.

22.4.2 POD: An Approximation Method

In this chapter, we decide to follow the view of *Chatterjee* [22.36] and to introduce the singular value decomposition and its generalization, the proper orthogonal decomposition (Sect. 22.4.3), in the general context of approximation theory [22.37].

Suppose we want to approximate a possibly vector-valued function $u(\boldsymbol{x}, t)$ over some domain of interest $\mathcal{D} = \Omega \times [0; T]$ as a finite sum in the separated-variables form:

$$u(\boldsymbol{x}, t) \simeq \sum_{k=1}^{K} a^{(k)}(t)\phi^{(k)}(\boldsymbol{x}) \,. \tag{22.43}$$

For simplicity and because it will be the case in fluid mechanics applications, $\boldsymbol{x}$ can be viewed as a spatial coordinate and t as a temporal coordinate.

Our expectation is that this approximation becomes exact as $K \longrightarrow +\infty$. The representation (22.43) is clearly not unique. A classic way to solve this approximation problem is to use for the basis functions $\phi^{(k)}(\boldsymbol{x})$, functions given a priori, for example Fourier series, Legendre polynomials or Chebyshev polynomials. An alternative approach could be to determine the functions $\phi^{(k)}(\boldsymbol{x})$ that are naturally intrinsic for the approximation of the function $u(\boldsymbol{x}, t)$. As will be explained in the following, this particular approach corresponds to the proper orthogonal decomposition (POD).

An additional difficulty is that a different sequence of time functions $a^{(k)}(t)$ corresponds to each choice of basis functions $\phi^{(k)}(\boldsymbol{x})$. So, given $\phi^{(k)}(\boldsymbol{x})$, how can we determine the coefficients $a^{(k)}(t)$? Suppose we have chosen

orthonormal basis functions, i. e.,

$$\int_{\Omega} \phi^{(k_1)}(\boldsymbol{x})\phi^{(k_2)}(\boldsymbol{x})\,\mathrm{d}\boldsymbol{x} = \delta_{k_1 k_2}\,, \tag{22.44}$$

where

$$\delta_{k_1 k_2} = \begin{cases} 0 & \text{for } k_1 \neq k_2, \\ 1 & \text{for } k_1 = k_2 \end{cases}$$

is the Kronecker delta symbol, then:

$$a^{(k)}(t) = \int_{\Omega} u(\boldsymbol{x}, t)\phi^{(k)}(\boldsymbol{x})\,\mathrm{d}\boldsymbol{x}\,.$$

Therefore for orthonormal basis functions, $a^{(k)}(t)$ depends only on $\phi^{(k)}(\boldsymbol{x})$ and not on the other ϕ. So for selecting the function $\phi^{(k)}(\boldsymbol{x})$, it would be useful to use the orthonormality condition.

Moreover, while an approximation to any desired accuracy can always be obtained if K can be chosen large enough, we may like to find, once and for all, a sequence of orthonormal functions $\phi^{(k)}(\boldsymbol{x})$ in such a way that the approximation for each K is as good as possible in a least-squares sense. Now consider that we can measure (experimentally or numerically) at N_t different instants of time, M realizations of $u(\boldsymbol{x}, t)$ at M different locations $x_1, x_2, \ldots, x_M$. The approximation problem (22.43) is then equivalent to finding the orthonormal functions $\{\phi^{(k)}(\boldsymbol{x})\}_{k=1}^{K}$ with $K \leq N_\mathrm{t}$ that solve:

$$\min \sum_{i=1}^{N_\mathrm{t}} \|u(\boldsymbol{x}, t_i) - \sum_{k=1}^{K} \left[u(\boldsymbol{x}, t_i), \phi^{(k)}(\boldsymbol{x})\right]\phi^{(k)}(\boldsymbol{x})\|_2^2\,, \tag{22.45}$$

where $\|\cdot\|_2$ define the norm associated with the usual L^2 inner product $(.,.)$. Remind that, for any vector $\boldsymbol{y} \in \mathbb{R}^M$, we have

$$\boldsymbol{y} = \begin{pmatrix} y_1 \\ \vdots \\ y_M \end{pmatrix} \Longrightarrow \|\boldsymbol{y}\|_2 = (\boldsymbol{y}, \boldsymbol{y})^{1/2} = \sqrt{\boldsymbol{y}^\mathrm{T}\boldsymbol{y}} = \sqrt{y_1^2 + \ldots + y_M^2}\,. \tag{22.46}$$

The practical method of solving the minimization problem (22.45) is to arrange the data set $\mathcal{U} = \{u(\boldsymbol{x}, t_1), \ldots, u(\boldsymbol{x}, t_{N_\mathrm{t}})\}$ in an $M \times N_\mathrm{t}$ matrix A called the snapshot data matrix

$$A = \begin{pmatrix} u(x_1, t_1) & u(x_1, t_2) & \cdots & u(x_1, t_{N_\mathrm{t}}) \\ u(x_2, t_1) & u(x_2, t_2) & \cdots & u(x_2, t_{N_\mathrm{t}}) \\ \vdots & \vdots & \vdots & \vdots \\ u(x_M, t_1) & u(x_M, t_2) & \cdots & u(x_M, t_{N_\mathrm{t}}) \end{pmatrix}\,,$$

$$A \in \mathbb{R}^{M \times N_\mathrm{t}}\,. \tag{22.47}$$

Each column $A_{:,i} \in \mathbb{R}^M$ of the snapshot data matrix represents a single snapshot $u(\boldsymbol{x}, t_i)$ of the input ensemble $\mathcal{U}$. We note that, if the snapshot data are assumed to be linearly independent (this will be the case in particular for the snapshot POD method for reasons explained in Sect. 22.4.6), the snapshot data matrix has full column rank.

The solutions of the minimization problem (22.45) are given by the truncated singular value decomposition of length K of the matrix A. For this reason, the singular value decomposition of a matrix is reviewed below. The relationship between the proper orthogonal decomposition and the singular value decomposition is addressed later in Sect. 22.4.2.

Singular Value Decomposition (SVD)

Definition of SVD. Let A be a general complex $M \times N_\mathrm{t}$ matrix. The singular value decomposition (SVD) of A is the factorization [22.16]:

$$A = U\Sigma V^\dagger\,, \tag{22.48}$$

where U and V are (non-unique) unitary $M \times M$ and $N_\mathrm{t} \times N_\mathrm{t}$ matrices, respectively, i. e. $UU^\dagger = I_M$ and $VV^\dagger = I_{N_\mathrm{t}}$, and $\Sigma = \mathrm{diag}(\sigma_1, \ldots, \sigma_r,)$ with $\sigma_1 \geq \sigma_2 \geq \ldots \geq \sigma_r \geq 0$ where $r = \min(M, N_\mathrm{t})$. The rank of A equals the number of nonzero singular values it has. Here, $V^\dagger$ denotes the adjoint matrix of V defined as the conjugate transpose of V. Remind that for a unitary matrix $A^{-1} = A^\dagger$. If $A \in \mathbb{R}^{M \times N_\mathrm{t}}$ then $V^\dagger = V^\mathrm{T}$, and V is said to be orthogonal.

The σ_i are called the singular values of A (and of $A^\dagger$), the first r columns of $V = (v_1, v_2, \ldots, v_{N_\mathrm{t}})$ are the right singular vectors, and the first r columns of $U = (u_1, u_2, \ldots, u_M)$ are the left singular vectors. Since the singular values are arranged in a specific order, the index i of the i-th singular value will be called the singular value number.

Geometric Interpretations of SVD.

Geometric Structure of a Matrix. By definition of a matrix, an $M \times N_\mathrm{t}$ matrix A is a linear operator that maps

vectors from an N_t-dimensional space, say $\mathcal{E}_{N_t}$, to an M-dimensional space, say $\mathcal{E}_M$. Imagine the unit sphere in $\mathcal{E}_{N_t}$ (the set of vectors of unit magnitude). Multiplication of these vectors by the matrix A results in a set of vectors that defines an r-dimensional ellipsoid in $\mathcal{E}_M$, where r is the number of nonzero singular values. The singular values $\sigma_1, \sigma_2, \ldots, \sigma_r$ are the lengths of the principal radii of that ellipsoid (Fig. 22.10). Intuitively, the singular values of a matrix describe the extent to which multiplication by the matrix distorts the original vector. Moreover, since the matrix V is unitary, (22.48) becomes $AV = U\Sigma$. The consequences are that the directions of these principal radii are given by the columns of U and the pre-images of these principal radii are the columns of V. A second geometric interpretation is given in the next section.

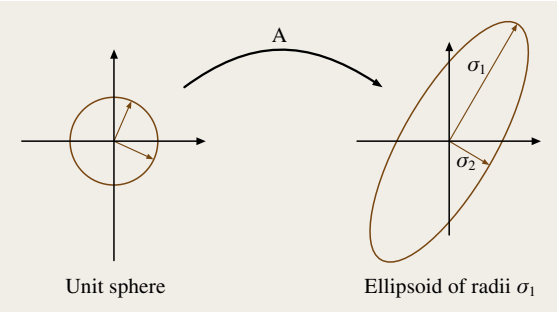

Fig. 22.10 Geometric interpretation of the SVD of the matrix A: image by A of a unit sphere

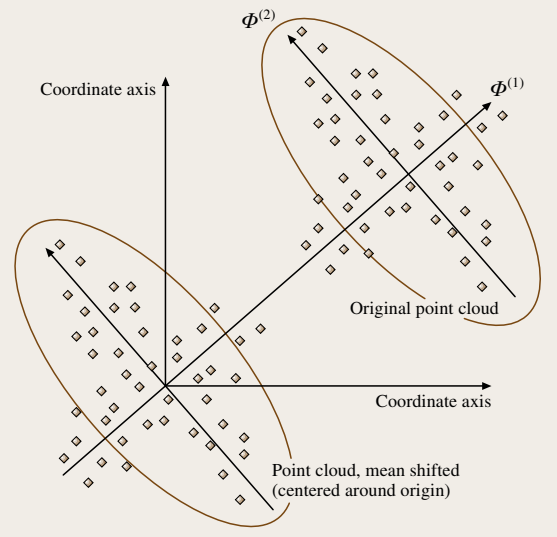

Fig. 22.11 Geometric interpretation of the SVD of the matrix A: phase-space rotation

Due to the interpretation of the matrix A in terms of linear algebra, it is now obvious that the 2-induced norm of A is σ_1

$$\|A\|_2 = \max_{\|x\|=1} \|Ax\|_2 = \sigma_1 \,. \tag{22.49}$$

SVD as a Phase-Space Rotation. A second geometric interpretation may be attributed to SVD applications. We now view the $M \times N_t$ matrix A as a list of coordinates of M points denoted $P_1, P_2, \ldots, P_M$ in an N_t-dimensional space. Each point P_i is represented in Fig. 22.11 by a diamond. For any $k \leq N_t$, we seek a k-dimensional subspace for which the mean square distance of the points, from the subspace, is minimized, i. e., we search a vector $\boldsymbol{\Phi}^{(1)}$ (Fig. 22.11) such that $\sum_{i=1}^{M} |\boldsymbol{H_i P_i}|^2$ is minimized, where H_i are the orthogonal projection of P_i onto the line of direction vector $\boldsymbol{\Phi}^{(1)}$. This mathematical procedure can be geometrically interpreted (Fig. 22.11) as a rotation of the phase space from the original basis into a new coordinate system whose orthogonal axes coincide with the axes of inertia of the data. This formulation of the SVD problem corresponds exactly to the way principal component analysis is commonly introduced in the literature [22.14].

When the singular value decomposition is used for data analysis, the SVD algorithm is generally applied to a matrix deduced from the snapshot matrix A by subtracting from each column of A the mean of that column. This mean shift ensures that the M-point cloud is now centered around the origin of the coordinate (Fig. 22.11).

Relationships Between SVD and Eigenvalue Problems

In this section, we present how the singular values and the right and left singular vectors of a rectangular matrix A can also be computed by solving symmetric eigenproblems with, e.g., the matrices $A^\dagger A$ or $AA^\dagger$, instead of computing the SVD of A. In this case, $A^\dagger A$ and $AA^\dagger$ represent a finite-dimensional version of the two-point space–time correlation R introduced in Sect. 22.4.3. The results of this section will be used later.

Let $A = U\Sigma V^\dagger$ be a singular value decomposition of $A \in \mathbb{R}^{M \times N_t}$. Then $A^\dagger A = V\Sigma U^\dagger U\Sigma V^\dagger = V\Sigma^2 V^\dagger$, where Σ^2 is a diagonal matrix. Since $A^\dagger A$ is an Hermitian matrix, its eigenvalue decomposition can be written: $A^\dagger A = W\Lambda W^{-1} = W\Lambda W^\dagger$, where W is an $N_t \times N_t$ unitary matrix. By comparing the two expression of A, we conclude that $\Sigma^2 = \Lambda$, and $W = V$. In other words $\sigma_i = \sqrt{\lambda_i}$, and (V, Λ) is the eigenvector–eigenvalue decomposition of $A^\dagger A \in \mathbb{R}^{N_t \times N_t}$.

The same development applied to the matrix $AA^\dagger$ leads to $AA^\dagger = U\Sigma V^\dagger V\Sigma U^\dagger = U\Sigma^2 U^\dagger = W\Lambda W^\dagger$, so (U, Λ) is the eigenvector–eigenvalue decomposition of $AA^\dagger \in \mathbb{R}^{M\times M}$.

At this point, we remark that the eigenvalue problem associated with $A^\dagger A$ is more practical to solve than the eigenvalue problem associated with $AA^\dagger$ in cases where the input collection N_t is significantly smaller than the number of coefficients needed to represent each item of the collection M. This remark explains why two different POD approaches exist: the classical POD (Sect. 22.4.5) and the snapshot POD (Sect. 22.4.6).

Lower-Rank Approximation to A

Given $A \in \mathbb{R}^{M\times N_t}$, the computation of a matrix $X \in \mathbb{R}^{M\times N_t}$ with $\mathrm{rank}(X) = k < \mathrm{rank}(A)$ such that an appropriate norm of the error $E = A - X$ is minimized is a classical problem. This problem can be solved explicitly if we take as the norm the Frobenius norm, defined as the square root of the sums of squares of all the elements and denoted by $\|\cdot\|_F$ or any unitarily invariant norm. The solution is given by the Eckart–Young theorem [22.38] which states that

$$\min_{\mathrm{rank}(X)\le k} \|A - X\|_F = \|A - A_k\|_F = \sqrt{\sum_{i=k+1}^{r} \sigma_i^2(A)}\,, \tag{22.50}$$

where

$$A_k = U\begin{pmatrix}\Sigma_k & 0\\ 0 & 0\end{pmatrix}V^\dagger = \sigma_1 u_1 v_1^\dagger + \ldots + \sigma_k u_k v_k^\dagger$$

where Σ_k is the matrix obtained by setting $\sigma_{k+1} = \sigma_{k+2} = \ldots = \sigma_r = 0$ in Σ.

For example, the 2-norm defined by (22.49) can be used. In this case, the Eckart–Young theorem (22.50) yields [22.39]:

$$\min_{\mathrm{rank}(X)\le k} \|A - X\|_2 = \|A - A_k\|_2 = \sigma_{k+1}(A)\,.$$

Remark: This theorem establishes a relationship between the rank k of the approximant, and the $(k+1)$-th largest singular value of A. Therefore, if the singular values decrease is fast, we can hope to find an approximant with small rank (see the section on *Examples of Image Processing by SVD* below).

Relationship Between POD and SVD

Here, we discuss the close relationship between POD and SVD. Our presentation follows the view of *Fahl* [22.34] but similar treatments can be found in *Atwell* and *King* [22.40]. The reader is referred to *Volkwein* [22.41] for the mathematical demonstrations.

Suppose that each member of the input collection $\mathcal{U}$ defined in Sect. 22.4.2 can be written in terms of n-th-order finite-element basis functions $\{\varphi^{(j)}(\boldsymbol{x})\}_{j=1}^n$, i. e.,

$$u(\boldsymbol{x}, t_i) = u^n(\boldsymbol{x}, t_i) = \sum_{j=1}^{n} u^{(j)}(t_i)\varphi^{(j)}(\boldsymbol{x})\,,$$

where the superscript n denotes a high-order finite-element discretization.

The inner product can then be defined by:

$$(u, v)_{\mathcal{M}} = \boldsymbol{u}^{\mathrm{T}}\mathcal{M}\boldsymbol{v}\,, \tag{22.51}$$

where $\mathcal{M} \in \mathbb{R}^{n\times n}$ is the finite-element mass matrix and $\boldsymbol{u}, \boldsymbol{v} \in \mathbb{R}^n$ are the finite-element coefficient vectors for a given t_i. Employing a Cholesky factorization $\mathcal{M} = \mathcal{M}^{1/2}(\mathcal{M}^{1/2})^{\mathrm{T}}$, the $\mathcal{M}$ inner product (22.51) can be transformed to the standard Euclidean inner product (22.46) such that the condition

$$\|u\|_{\mathcal{M}} = (u, u)_{\mathcal{M}}^{1/2} = \|(\mathcal{M}^{1/2})^{\mathrm{T}}\boldsymbol{u}\|_2$$

holds. The minimization problem (22.45) can then be reformulated for the $\mathcal{M}$ inner product as

$$\min \sum_{i=1}^{N_t} \|u^n(\boldsymbol{x}, t_i) - \sum_{k=1}^{K} \left[u^n(\boldsymbol{x}, t_i), \phi^{(k)}(\boldsymbol{x})\right]_{\mathcal{M}} \phi^{(k)}(\boldsymbol{x})\|_{\mathcal{M}}^2\,, \tag{22.52}$$

where the POD basis functions $\{\phi^{(k)}\}_{k=1}^K$ are assumed to be in the linear space spanned by the finite-element basis functions $\{\varphi^{(j)}(\boldsymbol{x})\}_{j=1}^n$, i. e.,

$$\phi^{(k)}(\boldsymbol{x}) = \sum_{j=1}^{n} \phi_j^{(k)}\varphi^{(j)}(\boldsymbol{x})\,.$$

To reformulate the minimization problem (22.52) in a matrix approximation context, let $\Phi \in \mathbb{R}^{n\times K}$ denote a matrix collecting the finite-element coefficients of the unknown POD functions. Since for any matrix $\hat{A} \in \mathbb{R}^{n\times N_t}$, $\sum_{i=1}^{N_t} \|\hat{A}_{:,i}\|_2^2 = \|\hat{A}\|_F$, where $\|\cdot\|_F$ denotes the Frobenius norm defined earlier (22.50), the problem (22.52) is equivalent to solving:

$$\min_{Z\in\mathbb{R}^{n\times K}} \|\hat{A} - ZZ^{\mathrm{T}}\hat{A}\|_F^2 \quad \text{s.t.} \quad Z^{\mathrm{T}}Z = I_K \tag{22.53}$$

with $\hat{A} = (\mathcal{M}^{1/2})^{\mathrm{T}} A$ and $Z = (\mathcal{M}^{1/2})^{\mathrm{T}} \Phi$, where $Z \in \mathbb{R}^{n \times K}$.

Equation (22.53) indicates that we are looking for a K dimensional subspace with orthogonal matrix Z such that $X = ZZ^{\mathrm{T}}\hat{A}$ is the best approximation to $\hat{A}$ compared to all subspaces of dimension K. According to the Eckart–Young theorem (22.50), the solution to problem (22.53) is given by a truncated singular value decomposition of $\hat{A}$ of length K

$$\hat{A}_K = U_K \Sigma_K V_K^{\mathrm{T}} , \tag{22.54}$$

where U_K and V_K correspond to the first K columns of U and V, respectively. Finally, comparing $\hat{A}_K$ and the form of X, we find that the matrix Φ solves

$$(\mathcal{M}^{1/2})^{\mathrm{T}} \Phi = U_K \in \mathbb{R}^{n \times K} . \tag{22.55}$$

The finite-element coefficients of the POD basis functions can then be computed by solving the linear system (22.55) where the left singular vectors U of $\hat{A} = U\Sigma V^{\mathrm{T}}$ can be obtained directly as the eigenvalues of the previous $\hat{A}\hat{A}^{\mathrm{T}}$ matrix. However, as was previously remarked at the end of Sect. 22.4.2, when N_{t} is significantly smaller than n it is more practical to solve the eigenvalue problem $\hat{A}^{\mathrm{T}}\hat{A}$. It follows that, in this case, the right singular vectors V of $\hat{A}$ are obtained and U must be deduced from V by the equation $U = \Sigma^{-1}\hat{A}V$.

Remark: The eigenvalue problems can be solved with the library LAPACK [22.42] and efficient algorithms for POD computations based on Lanczos iterations can be found in *Fahl* [22.34].

Examples of Image Processing by SVD

As an illustration of the SVD process for computing low-rank approximations to data matrices, consider a time-independent problem where the input collection consists of greyscale images. In Fig. 22.14a and Fig. 22.15a the *clown* picture and the *trees* picture from MatLab are considered. These images can be represented by means of a 200×330, and a 128×128 matrix, respectively, each entry (pixel) having a value between 0 (white) and 1 (black) in 64 levels of gray. Both matrices have full rank, i. e., 200 and 128, respectively. Their numerical ranks however are much lower. The singular values of these two images are shown in Fig. 22.12 on a semi-log scale; both sets of singular values fall off rapidly, and hence low-rank approximations with small errors are possible.

By comparing the spectrum of the two singular value plots, we can determine that the relative error for approximants of the same rank is greater for the *clown* image than for the *trees* image. Thus the *trees* image is easier to approximate.

The Eckart–Young theorem states that, for any matrix A of rank N, an approximation of rank $k \leq N$ of the matrix A can be obtained by

$$A = \sigma_1 u_1 v_1^{\dagger} + \sigma_2 u_2 v_2^{\dagger} + \ldots + \sigma_k u_k v_k^{\dagger} .$$

Thus using the singular value decomposition, one can obtain a high-fidelity model, perhaps with large k. In order to obtain a lower-rank representation of these images, singular modes corresponding to small singular values are neglected. So if the spectrum of the singu-

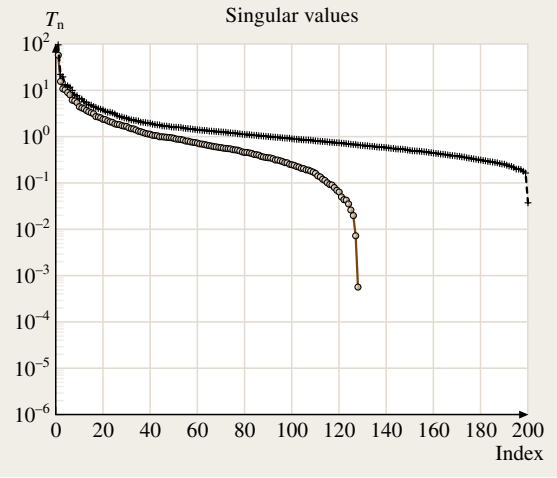

Fig. 22.12 Singular values for the *clown* image (*crosses*) and the *trees* image (*open circles*)

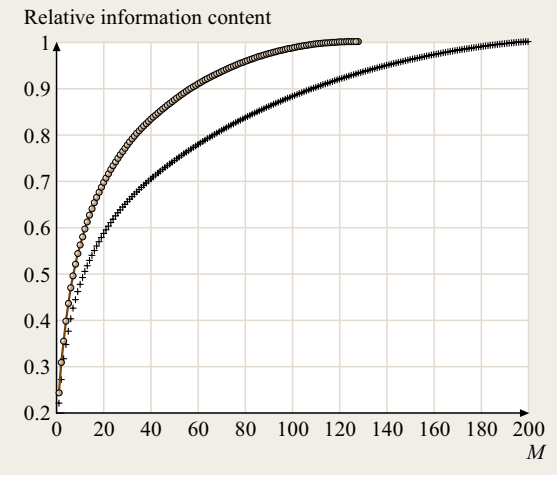

Fig. 22.13 Relative information content for the *clown* image (*crosses*) and the *trees* image (*open circles*)

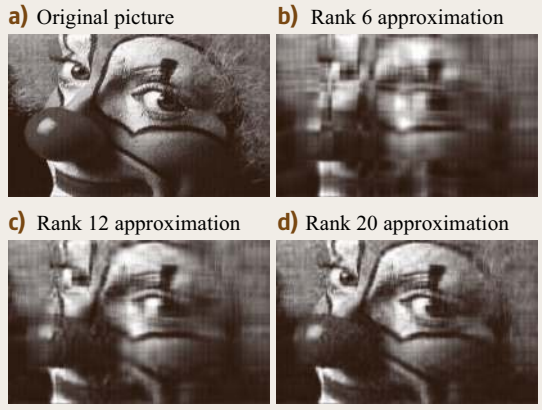

Fig. 22.14a–d Approximations of the *clown* image from MatLab by images of lower rank. **(a)** Original picture. **(b)** Rank 6 approximation. **(c)** Rank 12 approximation. **(d)** Rank 20 approximation

lar values decays fast, one can choose a cutoff value $M \ll N$ and carry out an approximation of A with a reduced number of singular modes. To make this idea more precise, one can define the *relative information content* (RIC) of the singular value decomposition of A by

$$\mathrm{RIC}(M) = \frac{\sum_{i=1}^{M} \sigma_i}{\sum_{i=1}^{N} \sigma_i} \,. \tag{22.56}$$

If the low-rank approximation is required to contain $\delta\%$ of the total information contained in the original image, the dimension M of the subspace D_M^{SVD} spanned by the M first singular modes is determined by

$$M = \mathrm{argmin}\{\mathrm{RIC}(M);\, \mathrm{RIC}(M) \geq \delta\} \,. \tag{22.57}$$

Another way to measure the degree of order of the signal u contained in the snapshot data matrix A is to define a global entropy [22.43] as

$$H(u) = -\frac{1}{\log N} \sum_{k=1}^{N} p_k \log(p_k)$$

with

$$p_k = \frac{\sigma_k}{\sum_{i=1}^{N} \sigma_i} \,.$$

If the information is uniformly distributed among all the modes, the entropy is maximal and equal to one.

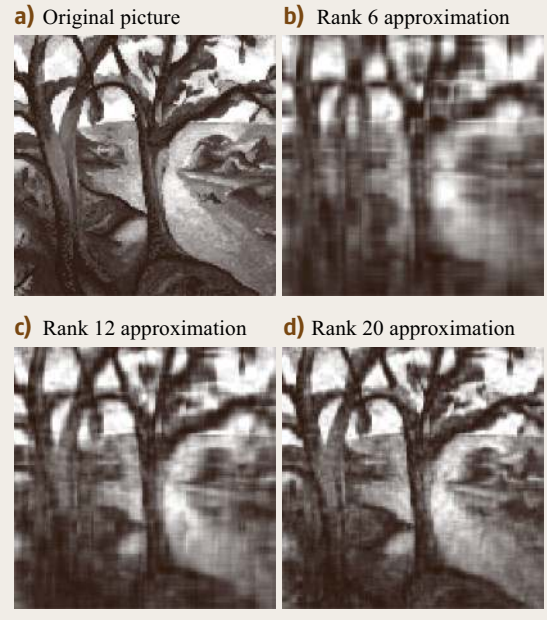

Fig. 22.15a–d Approximations of the *trees* image from MatLab by images of lower rank. **(a)** Original picture. **(b)** Rank 6 approximation. **(c)** Rank 12 approximation. **(d)** Rank 20 approximation

Similarly, if there is only one nonzero singular value, then the entropy is zero. At intermediate states, $H(u)$ keeps increasing as more modes become necessary to represent the data.

In Fig. 22.13, the relative information content for the *clown* image and the *trees* image are shown. The same result as previously mentioned for the two images when the singular values spectrum was discussed is evidenced. For a given number of singular modes, say $M = 20$, respectively, 60% and 70% of the information content of the original *clown* image and *trees* image are contained in the approximation. This clearly demonstrates that the *trees* image is easier to approximate by a lower-rank image than the *clown* image.

Lastly, we present in Figs. 22.14 and 22.15, clockwise from the top, the original picture, and approximants of rank 6, rank 20, and rank 12, for the *clown* image and *trees* image, respectively.

22.4.3 The Proper Orthogonal Decomposition (POD)

This section introduces the proper orthogonal decomposition in the spirit of *Holmes* et al. [22.24], as a technique

that can contribute to a better understanding of turbulent flows. Here, POD is not reduced to an advanced processing method that allows the extraction of coherent structures from experimental or numerical data. Rather, POD is used to provide a set of basis functions with which to identify a low-dimensional subspace on which to construct a dynamical model of the coherent structures by projection on the governing equations. This idea was first applied in *Aubry* et al. [22.29] to model the near-wall region of a turbulent boundary layer and more recently by *Ukeiley* et al. [22.30] to study the dynamics of the coherent structures in a plane turbulent mixing layer.

The Fredholm Equation

Let $\{\boldsymbol{u}(\boldsymbol{X}), \boldsymbol{X} = (\boldsymbol{x}, t_n) \in \mathcal{D} = \mathbb{R}^3 \times \mathbb{R}^+\}$ denote the set of observations (also called *snapshots*) obtained at N_t different time steps t_n over a spatial domain of interest Ω ($\boldsymbol{x} = (x, y, z) \in \Omega$). These snapshots could be experimental measurements or numerical solutions of velocity fields, vorticity fields, temperatures, etc. taken at different time steps and/or different physical parameters, for example Reynolds number [22.44]. The underlying problem is to extract from this ensemble of random vector fields a coherent structure. Following *Lumley* [22.3], a coherent structure is defined as *the deterministic function which is best correlated on average with the realizations* $\boldsymbol{u}(\boldsymbol{X})$. In other words, we look for a function $\boldsymbol{\Phi}$ that has the largest mean square projection onto the observations $|(\boldsymbol{u}, \boldsymbol{\Phi})|^2$. Since it is only the parallelism between $\boldsymbol{\Phi}$ and the observations that is of interest, the dependence on the amplitude of $\boldsymbol{\Phi}$ must be removed. One way is to normalize the amplitude of $\boldsymbol{\Phi}$. It is then natural to look at a space of functions $\boldsymbol{\Phi}$ for which the inner product exists, i. e., to impose $\boldsymbol{\Phi}$ to be an element of $L^2(\mathcal{D})$, the collection of square-integrable functions defined on the flow region $\mathcal{D}$. Finally, in order to include the statistics, we must maximize the expression:

$$\frac{\langle|(\boldsymbol{u}, \boldsymbol{\Phi})|^2\rangle}{\|\boldsymbol{\Phi}\|^2}$$

in some average sense (temporal, spatial, ensemble, or phase average), denoted here by $\langle\cdot\rangle$, to be specified for each application. The choice of the average operator is at the heart of the different POD approaches and a detailed discussion of this point is postponed to Sect. 22.4.4.

Hence, mathematically, the function $\boldsymbol{\Phi}$ corresponds to the solution of the constrained optimization problem:

$$\max_{\boldsymbol{\Psi}\in L^2(\mathcal{D})} \frac{\langle|(\boldsymbol{u}, \boldsymbol{\Psi})|^2\rangle}{\|\boldsymbol{\Psi}\|^2} = \frac{\langle|(\boldsymbol{u}, \boldsymbol{\Phi})|^2\rangle}{\|\boldsymbol{\Phi}\|^2} \qquad (22.58)$$

with respect to

$$(\boldsymbol{\Phi}, \boldsymbol{\Phi}) = \|\boldsymbol{\Phi}\|^2 = 1 \,.$$

Here $(.,.)$ and $\|\cdot\|$ denote the usual L^2 inner product and L^2 norm over $\mathcal{D}$:

$$\begin{aligned}(\boldsymbol{u}, \boldsymbol{\Phi}) &= \int_{\mathcal{D}} \boldsymbol{u}(\boldsymbol{X}) \cdot \boldsymbol{\Phi}^*(\boldsymbol{X}) \mathrm{d}\boldsymbol{X} \\ &= \sum_{i=1}^{n_c} \int_{\mathcal{D}} u_i(\boldsymbol{X}) \Phi_i^*(\boldsymbol{X}) \mathrm{d}\boldsymbol{X} \,; \quad \|\boldsymbol{u}\|^2 = (\boldsymbol{u}, \boldsymbol{u}) \,,\end{aligned}$$

where the superscript asterisk indicates the complex conjugate and n_c is the number of vectorial components of $\boldsymbol{u}(\boldsymbol{X})$. Note that L^2 seems to be a natural space in which to do fluid mechanics since it corresponds to flow having finite kinetic energy, but the choice of other norms for the POD basis computation is possible, see Sect. 22.4.4 for a discussion.

The maximization problem (22.58) can be cast in an equivalent eigenvalue problem. To see this, let us define the operator $\mathcal{R} : L^2(\mathcal{D}) \longrightarrow L^2(\mathcal{D})$ by

$$\mathcal{R}\boldsymbol{\Phi}(\boldsymbol{X}) = \int_{\mathcal{D}} R(\boldsymbol{X}, \boldsymbol{X}') \boldsymbol{\Phi}(\boldsymbol{X}') \mathrm{d}\boldsymbol{X}' \,,$$

where $R(\boldsymbol{X}, \boldsymbol{X}') = \langle \boldsymbol{u}(\boldsymbol{X}) \otimes \boldsymbol{u}^*(\boldsymbol{X}') \rangle$ is the two-point space–time correlation tensor ($\otimes$ is the dyadic product).

Then, straightforward calculations reveal that

$$\begin{aligned}&(\mathcal{R}\boldsymbol{\Phi}, \boldsymbol{\Phi}) \\ &= \left(\int_{\mathcal{D}} \langle \boldsymbol{u}(\boldsymbol{X}) \otimes \boldsymbol{u}^*(\boldsymbol{X}') \rangle \boldsymbol{\Phi}(\boldsymbol{X}') \mathrm{d}\boldsymbol{X}', \boldsymbol{\Phi}(\boldsymbol{X}) \right) \\ &= \int_{\mathcal{D}} \int_{\mathcal{D}} \langle \boldsymbol{u}(\boldsymbol{X}) \otimes \boldsymbol{u}^*(\boldsymbol{X}') \rangle \boldsymbol{\Phi}(\boldsymbol{X}') \mathrm{d}\boldsymbol{X}' \boldsymbol{\Phi}^*(\boldsymbol{X}) \mathrm{d}\boldsymbol{X} \\ &= \left\langle \int_{\mathcal{D}} \boldsymbol{u}(\boldsymbol{X}) \boldsymbol{\Phi}^*(\boldsymbol{X}) \mathrm{d}\boldsymbol{X} \int_{\mathcal{D}} \boldsymbol{u}^*(\boldsymbol{X}') \boldsymbol{\Phi}(\boldsymbol{X}') \mathrm{d}\boldsymbol{X}' \right\rangle \\ &= \langle |(\boldsymbol{u}, \boldsymbol{\Phi})|^2 \rangle \geq 0\end{aligned}$$

Furthermore, it follows that:

$$(\mathcal{R}\boldsymbol{\Phi}, \boldsymbol{\Psi}) = (\boldsymbol{\Phi}, \mathcal{R}\boldsymbol{\Psi}) \text{ for any } (\boldsymbol{\Phi}, \boldsymbol{\Psi}) \in [L^2(\mathcal{D})]^2 \,.$$

We suppose that the probabilistic structure of the ensemble of observations is such that the average and integrating operations can be interchanged [22.45].

Then $\mathcal{R}$ is linear and self-adjoint, i. e., $\mathcal{R}^\dagger = \mathcal{R}$, where the adjoint of $\mathcal{R}$, $\mathcal{R}^\dagger$, is defined by

$$(\mathcal{R}\boldsymbol{u}, \boldsymbol{v}) = (\boldsymbol{u}, \mathcal{R}^\dagger \boldsymbol{v})$$

for all $\boldsymbol{u} \in L^2(\mathcal{D})$ and $\boldsymbol{v} \in L^2(\mathcal{D})$.

nonnegative operator on $L^2(\mathcal{D})$, i.e. $(\mathcal{R}\boldsymbol{u}, \boldsymbol{u}) \geq 0$ for all $\boldsymbol{u} \in L^2(\mathcal{D})$. Consequently, spectral theory applies [22.23, 46] and guarantees that the maximization problem (22.58) admits a solution, equal to the largest eigenvalue of the problem

$$\mathcal{R}\boldsymbol{\Phi} = \lambda\boldsymbol{\Phi}\,, \tag{22.59}$$

which can be written as a Fredholm integral eigenvalue problem

$$\sum_{j=1}^{n_c} \int_{\mathcal{D}} R_{ij}(\boldsymbol{X}, \boldsymbol{X}')\Phi_j(\boldsymbol{X}')\mathrm{d}\boldsymbol{X}' = \lambda\Phi_i(\boldsymbol{X})\,. \tag{22.60}$$

The properties of the empirical eigenfunctions $\Phi_i(\boldsymbol{X})$ obtained by solving the Fredholm equation (22.60) are fully discussed in Sect. 22.4.3. Here, it is sufficient to make some comments shedding light on the constraints linked to the POD method.

In (22.60), the integral $\int_{\mathcal{D}} .\,\mathrm{d}\boldsymbol{X}'$ is over the entire domain of interest $\mathcal{D}$. The consequence is that the two-point correlation tensor R_{ij} has to be known over all $\mathcal{D}$. Therefore, the data volume to handle can be very important (several gigabytes are not rare) and sometimes data compression is necessary to reduce the data storage requirements (see [22.31] for an example). Due to the important size of the data sets necessary to apply POD, renewed interest in POD only appeared in the 1990s, explained by the great advances in numerical simulation capability and measurement techniques.

Remark: An alternative approach for finding the solution to maximization of (22.58) is by directly solving a classical problem in the calculus of variations. Since $(\mathcal{R}\boldsymbol{\Phi}, \boldsymbol{\Phi}) = \langle|(\boldsymbol{u}, \boldsymbol{\Phi})|^2\rangle$, the problem (22.58) is equivalent to determining the $\boldsymbol{\Phi}$ that maximizes λ, where

$$\lambda = \frac{\langle|(\boldsymbol{u}, \boldsymbol{\Phi})|^2\rangle}{(\boldsymbol{\Phi}, \boldsymbol{\Phi})} = \frac{(\mathcal{R}\boldsymbol{\Phi}, \boldsymbol{\Phi})}{(\boldsymbol{\Phi}, \boldsymbol{\Phi})}\,. \tag{22.61}$$

Using the calculus of variations, $\boldsymbol{\Phi}$ is determining by imposing the condition $\mathrm{d}F(\epsilon)/\mathrm{d}\epsilon|_{\epsilon=0} = 0$ with

$$\begin{aligned} F(\epsilon) &= \frac{[\mathcal{R}(\boldsymbol{\Phi}+\epsilon\boldsymbol{\Upsilon}), (\boldsymbol{\Phi}+\epsilon\boldsymbol{\Upsilon})]}{[(\boldsymbol{\Phi}+\epsilon\boldsymbol{\Upsilon}), (\boldsymbol{\Phi}+\epsilon\boldsymbol{\Upsilon})]} \\ &= \frac{(\mathcal{R}\boldsymbol{\Phi}, \boldsymbol{\Phi}) + \epsilon(\mathcal{R}\boldsymbol{\Phi}, \boldsymbol{\Upsilon}) + \epsilon(\mathcal{R}\boldsymbol{\Upsilon}, \boldsymbol{\Phi}) + \epsilon^2(\mathcal{R}\boldsymbol{\Upsilon}, \boldsymbol{\Upsilon})}{(\boldsymbol{\Phi}, \boldsymbol{\Phi}) + \epsilon(\boldsymbol{\Phi}, \boldsymbol{\Upsilon}) + \epsilon(\boldsymbol{\Upsilon}, \boldsymbol{\Phi}) + \epsilon^2(\boldsymbol{\Upsilon}, \boldsymbol{\Upsilon})}\,. \end{aligned}$$

This leads one to verify for any $\boldsymbol{\Upsilon}$ the condition

$$(\mathcal{R}\boldsymbol{\Phi}, \boldsymbol{\Upsilon}) = \lambda(\boldsymbol{\Phi}, \boldsymbol{\Upsilon})\,,$$

which is equivalent to finding the eigenvalue of the eigenvalue problem (22.59).

Properties of the POD Basis Functions

Eight main properties can be derived.

1. For a bounded integration domain $\mathcal{D}$, Hilbert–Schmidt theory applies [22.46] and assures us that there is not one, but a denumerable infinity of solutions of (22.60). Then, the Fredholm equation (22.60) has a discrete set of solutions satisfying:

$$\sum_{j=1}^{n_c} \int_{\mathcal{D}} R_{ij}(\boldsymbol{X}, \boldsymbol{X}')\Phi_j^{(n)}(\boldsymbol{X}')\mathrm{d}\boldsymbol{X}' = \lambda^{(n)}\Phi_i^{(n)}(\boldsymbol{X})\,, \tag{22.62}$$

   where $\lambda^{(n)}$ and $\Phi_i^{(n)}$ denote, respectively, the POD eigenvalues and POD eigenvectors or eigenfunctions of order $n = 1, 2, 3, \ldots, +\infty$. Each new eigenfunction is sought as the solution problem of the maximization problem (22.58) subject to the constraint of being orthogonal to all previously found eigenfunctions. Hence, by construction, the eigenfunctions are mutually orthogonal but they can be chosen orthonormal (see item 4). Any d-fold degenerate eigenvalue is associated with d linearly independent eigenfunctions.
2. If $\mathcal{R}$ is a self-adjoint and nonnegative operator then all eigenvalues are real and positive:

$$\lambda^{(1)} \geq \lambda^{(2)} \geq \lambda^{(3)} \geq, \ldots \lambda^{(+\infty)} \geq 0 \tag{22.63}$$

   and the corresponding series converges:

$$\sum_{n=1}^{+\infty} \lambda^{(n)} < +\infty\,.$$

3. The eigenfunctions $\boldsymbol{\Phi}^{(n)}$ form a complete orthogonal set, which means that almost every member (except possibly on a set of measure zero, see [22.47]) of the snapshots can be reconstructed in the following way:

$$u_i(\boldsymbol{X}) = \sum_{n=1}^{+\infty} a^{(n)}\Phi_i^{(n)}(\boldsymbol{X})\,. \tag{22.64}$$

4. The eigenfunctions $\boldsymbol{\Phi}^{(n)}$ can be chosen to be mutually orthonormal:

$$\sum_{i=1}^{n_c} \int_{\mathcal{D}} \Phi_i^{(m)}(\boldsymbol{X})\Phi_i^{*(n)}(\boldsymbol{X})\mathrm{d}\boldsymbol{X} = \delta_{mn}$$

$$\text{where } \delta_{mn} = \begin{cases} 0 & \text{for } m \neq n\,; \\ 1 & \text{for } m = n\,. \end{cases} \tag{22.65}$$

Since $\mathcal{R}$ is a self-adjoint operator, orthogonality is verified necessarily. On the other hand, the choice of orthonormality for the eigenfunctions is rather arbitrary because they are determined relative to a real multiplicative constant. Hence, it is numerically equivalent to impose:

$$\sum_{i=1}^{n_c} \int_{\mathcal{D}} \Phi_i^{(m)}(\boldsymbol{X}) \Phi_i^{*(n)}(\boldsymbol{X}) \mathrm{d}\boldsymbol{X} = \lambda^{(m)} \delta_{mn} \quad (22.66)$$

for the eigenfunctions $\Phi_i^{(m)}(\boldsymbol{X})$ and the condition $\langle a^{(n)} a^{*(m)} \rangle = \delta_{mn}$ for the projection coefficient $a^{(n)}$ or to impose for the eigenfunctions the orthonormality condition (22.66) and the orthogonality condition (22.69) for the coefficients. For numerical reasons, it is easier to use (22.66) for *classical POD*, and (22.65) for *snapshot POD* [22.48].

5. The random coefficients $a^{(n)}$, projections of $\boldsymbol{u}$ onto $\boldsymbol{\Phi}$, are then calculated by using the orthonormality of the eigenfunctions $\boldsymbol{\Phi}$:

$$a^{(n)} = (\boldsymbol{u}, \boldsymbol{\Phi}) = \sum_{i=1}^{n_c} \int_{\mathcal{D}} u_i(\boldsymbol{X}) \Phi_i^{*(n)}(\boldsymbol{X}) \mathrm{d}\boldsymbol{X} \,. \quad (22.67)$$

6. The two-point space–time correlation tensor R_{ij} can be decomposed as a uniformly convergent series [22.23]:

$$R_{ij}(\boldsymbol{X}, \boldsymbol{X}') = \sum_{n=1}^{+\infty} \lambda^{(n)} \Phi_i^{(n)}(\boldsymbol{X}) \Phi_j^{*(n)}(\boldsymbol{X}') \,. \quad (22.68)$$

This result is known as Mercer's theorem.

7. The diagonal representation of the tensor R_{ij} combined with the decomposition of $\boldsymbol{u}$ onto the eigenfunctions $\boldsymbol{\Phi}$ and their orthogonality assure that the coefficients $a^{(n)}$ are mutually uncorrelated and that their mean square values are the eigenvalues themselves.

$$\langle a^{(n)} a^{*(m)} \rangle = \delta_{mn} \lambda^{(n)} \,. \quad (22.69)$$

Proof: This assertion derives directly from the representation of $R_{ij}(\boldsymbol{X}, \boldsymbol{X}')$, given in equation (22.68):

$$\begin{aligned} & R_{ij}(\boldsymbol{X}, \boldsymbol{X}') \\ &= \left\langle u_i(\boldsymbol{X}) u_j^*(\boldsymbol{X}') \right\rangle \\ &= \left\langle \sum_{n=1}^{+\infty} a^{(n)} \Phi_i^{(n)}(\boldsymbol{X}) \sum_{m=1}^{+\infty} a^{*(m)} \Phi_j^{*(m)}(\boldsymbol{X}') \right\rangle \\ &= \sum_{n=1}^{+\infty} \sum_{m=1}^{+\infty} \langle a^{(n)} a^{*(m)} \rangle \Phi_i^{(n)}(\boldsymbol{X}) \Phi_j^{*(m)}(\boldsymbol{X}') \,. \end{aligned}$$

But we know from the Mercer's theorem that

$$R_{ij}(\boldsymbol{X}, \boldsymbol{X}') = \sum_{n=1}^{+\infty} \lambda^{(n)} \Phi_i^{(n)}(\boldsymbol{X}) . \Phi_j^{*(n)}(\boldsymbol{X}') \,,$$

and so, since the $\boldsymbol{\Phi}^{(n)}(\boldsymbol{X})$ are an orthonormal family in $L^2(\mathcal{D})$, we see that $\langle a^{(n)} a^{*(m)} \rangle = \delta_{mn} \lambda^{(n)}$.

8. Finally, Mercer's theorem and the orthonormality of $\boldsymbol{\Phi}^{(n)}$ lead to

$$\sum_{i=1}^{n_c} \int_{\mathcal{D}} R_{ii}(\boldsymbol{X}, \boldsymbol{X}) \mathrm{d}\boldsymbol{X} = \sum_{n=1}^{+\infty} \lambda^{(n)} = E \,. \quad (22.70)$$

If $\boldsymbol{u}(\boldsymbol{X})$ is a velocity field, then E corresponds to the turbulent kinetic energy (TKE) integrated over the domain $\mathcal{D}$. In the same way, if $\boldsymbol{u}(\boldsymbol{X})$ is a vorticity field, as in *Sanghi* [22.49], this relation leads to the system enstrophy. So, whatever variable is considered for the POD, the eigenvalues $\lambda^{(n)}$ obtained by solving the Fredholm equation (22.60) are always homogeneous to energy but are not strictly speaking energy. Thinking of the POD eigenvalues as energy in a general mechanical context is incorrect in principle and may lead to misleading results. The interpretation of this equation is that every structure of order (n) makes an independent contribution to the TKE. Then, the amplitude of the eigenvalues $\lambda^{(n)}$ measure the relative importance of the different structures present within the flow.

Optimality of the POD Basis

Suppose that we have a signal $\boldsymbol{u}(\boldsymbol{X})$ with $\boldsymbol{u} \in L^2(\mathcal{D})$ and an approximation $\boldsymbol{u}^a$ of $\boldsymbol{u}$ with respect to an arbitrary orthonormal basis $\boldsymbol{\Psi}^{(n)}(\boldsymbol{X})$, $n = 1, 2, \ldots, +\infty$. One can write:

$$u_i^a(\boldsymbol{X}) = \sum_{n=1}^{+\infty} b^{(n)} \Psi_i^{(n)}(\boldsymbol{X}) \,.$$

Equations (22.70) and (22.69) clearly state that, if the $\Psi_i^{(n)}(\boldsymbol{X})$ have been nondimensionalized, $\langle b^{(n)} b^{*(n)} \rangle$ represents the average energy in the n-th mode. The following lemma establishes the notion of the optimality of the POD approach.

Lemma. Let $\{\boldsymbol{\Phi}^{(1)}(\boldsymbol{X}), \boldsymbol{\Phi}^{(2)}(\boldsymbol{X}), \ldots, \boldsymbol{\Phi}^{(\infty)}(\boldsymbol{X})\}$ denote an orthonormal set of POD basis elements, and $\{\lambda_1, \lambda_2, \ldots, \lambda_\infty\}$ denote the corresponding set of eigenvalues. If

$$u_i^P(\boldsymbol{X}) = \sum_{n=1}^{+\infty} a^{(n)} \Phi_i^{(n)}(\boldsymbol{X})$$

denotes the approximation to $\boldsymbol{u}$ with respect to this basis, then for any value of N [22.24]:

$$\sum_{n=1}^{N}\langle a^{(n)}a^{*(n)}\rangle = \sum_{n=1}^{N}\lambda^{(n)} \geq \sum_{n=1}^{N}\langle b^{(n)}b^{*(n)}\rangle \; .$$

Proof: It is straightforward [see the proof of (22.69)] to show that the kernel R_{ij} can be expressed in terms of $\boldsymbol{\Psi}^{(n)}$, $n = 1, \ldots, +\infty$ as

$$R_{ij}(\boldsymbol{X}, \boldsymbol{X}') = \sum_{n=1}^{+\infty}\sum_{m=1}^{+\infty}\langle b^{(n)}b^{*(m)}\rangle \Psi_i^{(n)}(\boldsymbol{X})\Psi_j^{*(m)}(\boldsymbol{X}') \; .$$

Therefore, the projection of the kernel R_{ij} in an N-dimensional space spanned by $\{\boldsymbol{\Psi}^{(n)}\}_{n=1}^{N}$ can be written in matrix form as

$$R = \begin{pmatrix} \langle b^{(1)}b^{*(1)}\rangle & \cdots & \langle b^{(1)}b^{*(N)}\rangle & 0 & \cdots & 0 \\ \langle b^{(2)}b^{*(1)}\rangle & \cdots & \langle b^{(2)}b^{*(N)}\rangle & 0 & \cdots & 0 \\ \vdots & & \vdots & \vdots & & \vdots \\ \langle b^{(N)}b^{*(1)}\rangle & \cdots & \langle b^{(N)}b^{*(N)}\rangle & 0 & \cdots & 0 \\ 0 & \cdots & 0 & 0 & 0 & 0 \\ \vdots & & \vdots & \vdots & & \vdots \end{pmatrix} \; .$$

The proof finally relies on a result for linear operators [22.50, p. 260] that states that the sum of the first N eigenvalues of a self-adjoint operator is greater than or equal to the sum of the diagonal terms in any N-dimensional projection of it:

$$\sum_{n=1}^{N}\lambda^{(n)} \geq \mathrm{Tr}(R) = \sum_{n=1}^{N}\langle b^{(n)}b^{*(m)}\rangle \; .$$

This lemma establishes that, among all *linear* decompositions, the POD is the most efficient, in the sense that, for a given number of modes, N, the projection on the subspace spanned by the N leading eigenfunctions will contain the greatest possible kinetic energy on average. The reader must remember that optimality of the POD functions is obtained only with respect to other linear representations.

Model Reduction Aspects

The energetic optimality of the POD basis functions suggests that only a very small number of POD modes, say M, may be necessary to describe any signal $\boldsymbol{u}(\boldsymbol{X})$ of the input data efficiently. The choice of M is then an important and critical task and adequate criteria for choosing M must be introduced.

Let N_{POD} denote the number of POD modes obtained by solving the Fredholm equation (22.60). The truncation error $\epsilon(M)$ due to the use of M instead of N_{POD} POD basis functions in representing the input data is given by

$$\epsilon(M) = \left\| \boldsymbol{u}(\boldsymbol{X}) - \sum_{n=1}^{M}[\boldsymbol{u}(\boldsymbol{X}), \boldsymbol{\Phi}^{(n)}(\boldsymbol{X})]\boldsymbol{\Phi}^{(n)}(\boldsymbol{X}) \right\|^2 = \left\| \sum_{n=M+1}^{N_{\mathrm{POD}}}[\boldsymbol{u}(\boldsymbol{X}), \boldsymbol{\Phi}^{(n)}(\boldsymbol{X})]\boldsymbol{\Phi}^{(n)}(\boldsymbol{X}) \right\|^2 \; . \tag{22.71}$$

It is immediate to deduce from (22.71) the equivalent forms for the two particular approaches of POD described in Sect. 22.4.4. The reader is referred to *Fahl* [22.34], where ϵ is defined for the snapshot POD.

The quantity $\epsilon(M)$ measures the accumulated squared error in representing the input snapshots, due to neglecting the POD basis elements that correspond to small POD eigenvalues.

However, in practice, this criterion is never used and the choice of M is rather based on heuristic considerations. As indicated in point 8 of Sect. 22.4.3 on the properties of the POD basis functions, $\sum_{i=1}^{M}\lambda^{(i)}$ represents in some sense the average energy contained in the first M POD modes. For turbulent flows, it corresponds exactly to the average turbulent kinetic energy. Therefore, to capture most of the energy contained in the N_{POD} POD modes, it suffices to choose M so that $\sum_{i=1}^{M}\lambda^{(i)} \simeq \sum_{i=1}^{N_{\mathrm{POD}}}\lambda^{(i)}$. By definition, the ratio $\sum_{i=1}^{M}\lambda^{(i)} / \sum_{i=1}^{N_{\mathrm{POD}}}\lambda^{(i)}$ yields the percentage of the total kinetic energy in the N_{POD} POD modes that is contained in the first M POD basis functions. For a predefined percentage of energy, δ, the dimension M of the subspace spanned by the M first POD functions is chosen such that the condition

$$\frac{\sum_{i=1}^{M}\lambda^{(i)}}{\sum_{i=1}^{N_{\mathrm{POD}}}\lambda^{(i)}} \geq \delta \tag{22.72}$$

holds [22.22, 31, 34]. The criterion (22.72) is equivalent to the one based on the relative information content used in Sect. 22.4.2 for the singular value decomposition (22.57). The POD reduced basis subspace is defined as $D_M^{POD} = \mathrm{span}\{\boldsymbol{\Phi}^{(1)}, \boldsymbol{\Phi}^{(2)}, \ldots, \boldsymbol{\Phi}^{(M)}\}$.

To this point we have only discussed the model reduction associated with using POD basis functions in the approximation of the input collection. Dynamical models based on POD have not been discussed.

Nevertheless, the optimal energetic convergence of the POD basis functions suggests that only a very small number of modes may be necessary to describe the dynamics of the system. Therefore, starting from data issued from high-dimensional models (experimental data or detailed simulations), it seems conceivable that POD modes can be efficiently used in Galerkin projections that yield low-dimensional dynamical models. Even though there are no theoretical guarantees of optimality in dynamical modeling, this method was already used in many cases, for turbulent flows or optimal control of fluids and reasonable to excellent models were obtained. The presentation of this approach can be found in *Cordier* and *Bergmann* [22.31]. For turbulent flows, POD is used to build low-dimensional models that address the role of coherent structures in turbulence generation [22.29, 30]. For the optimal control of fluids, POD is used to obtain reduced-order models of dynamics that reduce the computational complexity associated with high-complexity models such as the Navier–Stokes equations [22.21, 22, 32, 34]. In the control literature [22.40], several philosophies exist for using a reduced basis obtained by applying POD in low-order control design. A *reduce-then-design* approach involves reduction of the system model before control design, and the *design-then-reduce* approach, in which full-order model design is followed by full-order control design, and then control order reduction.

As a partial conclusion, note that the reduced-order models based on POD belong to a wider class of approximation methods, called singular-value-based methods by *Antoulas* and *Sorensen* [22.51]. These authors recently reviewed the state of the art in the area of model reduction of dynamical systems and distinguish three broad categories of approximation methods: singular-value-based methods, Krylov-based methods, and iterative methods combining aspects of both the SVD and Krylov methods. Since, the strengths and weaknesses of these methods are different, new insights can certainly be gained by applying these approximation methods to fluid flow control. For example, the reader is referred to *Allan* [22.52] for an application of the Krylov subspace method to derive an optimal feedback control design for driven cavity flow.

22.4.4 The Different POD Approaches

Except for the inner product, defined as the standard L^2 inner product for simplicity of presentation, the POD was derived in Sect. 22.4.3 in a general setting. The fundamental questions of the choice of

- the input collection
- the inner product
- the averaging operation $\langle\cdot\rangle$ (spatial or temporal)
- the variable $\boldsymbol{X}$ (spatial $\boldsymbol{x} = (x, y, z)$ or temporal t)

were not discussed. This section demonstrates that different orthogonal decompositions can be obtained depending, for example, on the way the averaging operator $\langle\cdot\rangle$ is defined to calculate the kernel of the Fredholm equation (22.60). In what follows, only two methods, classical POD (Sect. 22.4.5) and snapshot POD (Sect. 22.4.6), will be fully described. The reader is referred to *Aubry* et al. [22.53] for a presentation of the generalization of these two methods called *the biorthogonal decomposition*.

Choice of Input Collection

Choosing an input collection is a vital part of the proper orthogonal decomposition process since the POD basis only reflects information provided by the input collection. Indeed, the POD algorithm tries to remove *redundant* information (if any) from the database. As a consequence, the ability of POD modes to approximate any state of a complex system is totally dependent on the information originally contained in the snapshot set used to generate the POD basis. The POD eigenfunctions are intrinsically linked to the input data used to extract them. This is the source of the method's strengths as well as its limitations: extrapolation of the POD functions to different geometries or control parameters (Reynolds number, . . .), can be difficult to undertake (see [22.54, Chap. 4.6, p. 254] for a discussion).

When the POD basis is used for model reduction, an input collection of time snapshots is frequently chosen (Sect. 22.4.6). Typically, this data set comes from experimental measurement or numerical computations. Hence the data have some error associated with them. Therefore it is important to study the effect of these errors, assimilated to infinitesimal perturbations, on the outcome of the POD model-reduction procedure. This fundamental question has only recently been investigated theoretically, by *Rathinam* and *Petzold* [22.55]. These authors introduced the POD sensitivity factor as a nondimensional measure of the sensitivity of the resulting projection to perturbations in data. They found that the POD sensitivity is relevant in some applications while it is not in others. These theoretical results still need to be illustrated by realistic examples issued from fluid mechanics, for example. Now, consider the

ideal case with no perturbations in the input collection. Choosing a time snapshot input collection relevant for dynamical system description remains a difficult task because there is no definitive way to decide how many snapshots are necessary to capture the information content of the system, how long numerical simulations or experiments should be run to generate sufficiently resolved snapshots, and which initial conditions should be used. The reader should remember that the input collection corresponds to solutions belonging to the attractor of a dynamical system such as the Navier–Stokes equation in fluid mechanics. If this attractor is ergodic, the initial conditions are forgotten as time proceeds [22.24].

For control problems based on reduced-order models, an open question is how to incorporate control information in the model implicitly. A simple solution, and one that is generally used, is to generate snapshots using a variety of control inputs to excite system dynamics that arise when a control is applied [22.56]. Recently, *Burkardt* et al. [22.57] demonstrate that centroidal Voronoi tessellations could be one method of intelligent sampling in the control parameter space that can be employed for generating good snapshots set.

Choice of Inner Product and Norm

So far, POD was described in the context of the standard L^2 inner product for reasons of simplicity and, more importantly, because it corresponds to the general case for fluid flow applications for reasons explained later in Sect. 22.4.4. However, in a few cases it may be useful to use a different inner product to obtain different notions of optimality.

L^2 Inner Product. Let $L^2(\Omega)$ be the Hilbert space of square-integrable complex-valued functions defined on Ω. Square-integrable means that the functions $f(x)$ belonging to $L^2(\Omega)$ satisfy

$$\|f\| = (f, f)^{1/2} = \left[\int_\Omega |f|^2 \,\mathrm{d}x\right]^{1/2} < +\infty \,.$$

For vector-valued functions $\boldsymbol{u}$, such as the velocity field in a fluid flow, the inner product on $L^2(\Omega)$ is defined by

$$(\boldsymbol{u}, \boldsymbol{v}) = \int_\Omega \left(u_1 v_1^* + u_2 v_2^* + u_3 v_3^*\right) \mathrm{d}\boldsymbol{x} \,;$$
$$\|\boldsymbol{u}\|^2 = (\boldsymbol{u}, \boldsymbol{u}) \,, \qquad (22.73)$$

where Ω denotes the spatial domain occupied by the fluid. Moreover, its kinetic energy is proportional to $\|\boldsymbol{u}\|^2$. Therefore, L^2 is a natural space in which to do fluid mechanics since it corresponds to flow having finite kinetic energy. This is the reason why the L^2 inner product is the most commonly used to define the proper orthogonal decomposition.

H^1 Inner Product. Let $H^1(\Omega)$ be the Sobolev space of functions that, along with their first derivatives, belong to $L^2(\Omega)$.

In *Iollo* [22.58], it is found that the low-order model developed for the Euler equations by a straightforward Galerkin projection (see Sect. 22.4.10 for a description of the method) was unstable. Therefore, *Iollo* et al. [22.59] proposed a way to improve the numerical stability of the low-order model developed by Galerkin POD by redefining the norms involved in the POD definition as

$$(u, v)_\epsilon = \int_\Omega uv \,\mathrm{d}\boldsymbol{x} + \epsilon \int_\Omega (\nabla u \cdot \nabla v) \,\mathrm{d}\boldsymbol{x} \,, \qquad (22.74)$$

where ϵ is a parameter to take into account different metrics. Numerical experiments demonstrate the definite benefit of employing the H^1 formulation in the POD. Even though the use of the H^1 inner product seems beneficial for the robustness of the reduced-order model, we believe that it has not been given sufficient attention in the literature.

Inner Product for Compressible Flow. For compressible flow configurations, the velocity $\boldsymbol{u} = (u, v, w)$ and thermodynamic variables (e.g., density ρ, pressure p, enthalpy h) are dynamically coupled. This introduces questions of whether to treat the thermodynamic variables separately from the velocity, or together as a single vector-valued variable (e.g., $\boldsymbol{q}(\boldsymbol{x}) = (\rho, u, v, w, p)(\boldsymbol{x})$). For a scalar-valued POD, where separate POD modes are computed for each flow variable, the standard L^2 inner product defined by (22.73) can be used [22.60]. For vector-valued POD, where all the flow variables are written as a single vector $\boldsymbol{q}$, the standard inner product:

$$(\boldsymbol{q_1}, \boldsymbol{q_2}) = \int_\Omega (\rho_1\rho_2 + u_1u_2 + v_1v_2 + w_1w_2 + p_1p_2) \,\mathrm{d}\boldsymbol{x}$$

may not be a sensible choice for dimensional reasons. Of course, one could simply nondimensionalize the variables, but then the sense in which projections are optimal is rather arbitrary and depends on the nondimensionalization. *Rowley* [22.60] sought an inner product for compressible flow, which makes intuitive

sense in that the *energy* defined by the induced norm is a meaningful physical quantity. For a two-dimensional configuration, Rowley introduced a vector-valued variable $\boldsymbol{q} = (u, v, a)$, where u and v are the velocities and a is the local sound speed, and defined a family of inner products as

$$(\boldsymbol{q_1}, \boldsymbol{q_2})_\epsilon = \int_\Omega \left(u_1 u_2 + v_1 v_2 + \frac{2\epsilon}{\gamma(\gamma-1)} a_1 a_2 \right) \mathrm{d}\boldsymbol{x} \,, \tag{22.75}$$

where γ is the ratio of specific heats and ϵ is a parameter. If $\epsilon = \gamma$ then the induced norm gives $\|\boldsymbol{q}\|^2 = 2h_0$, i. e., twice the total enthalpy of the flow, and if $\epsilon = 1$ then the induced norm gives twice the total energy of the flow.

In spite of the proposals made by Rowley, the choice of the inner product best adapted to aeroacoustics still remains an open question.

To summarize: a POD approach is linked first to the definition of an inner product, which depends on the quantity to be investigated. When very different parameters have to be considered at the same time in this decomposition, weighting or proper normalization has to be considered in such a way that the behavior of these parameters is properly taken into account.

22.4.5 Classical POD or Direct Method

This approach was originated by *Lumley* [22.3]. In this case, the average $\langle\cdot\rangle$ is temporal:

$$\langle\cdot\rangle = \frac{1}{T}\int_T \cdot \,\mathrm{d}t$$

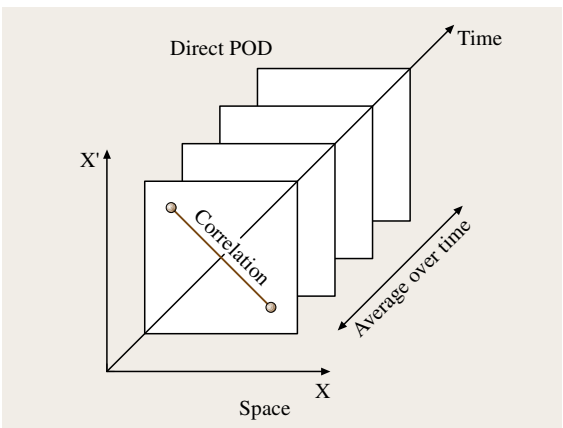

Fig. 22.16 Schematic view of the classical POD

and is evaluated as an ensemble average, based on the assumptions of stationarity and ergodicity. On the other hand, the variable $\boldsymbol{X}$ is assimilated to the space variable $\boldsymbol{x} = (x, y, z)$ defined over the domain Ω.

Figure 22.16 describes schematically the principle of the classical POD.

The corresponding eigenvalue problem is easily deduced from (22.62) by replacing the domain of integration $\mathcal{D}$ by Ω and the variable $\boldsymbol{X}$ by $\boldsymbol{x}$. The integral Fredholm equation to be solved is then given by

$$\sum_{j=1}^{n_c} \int_\Omega R_{ij}(\boldsymbol{x}, \boldsymbol{x}') \Phi_j^{(n)}(\boldsymbol{x}') \,\mathrm{d}\boldsymbol{x}' = \lambda^{(n)} \Phi_i^{(n)}(\boldsymbol{x}) \,, \tag{22.76}$$

where $R_{ij}(\boldsymbol{x}, \boldsymbol{x}')$ is the *two-point spatial correlation tensor* defined as

$$\begin{aligned} R_{ij}(\boldsymbol{x}, \boldsymbol{x}') &= \frac{1}{T}\int_T u_i(\boldsymbol{x}, t) u_j(\boldsymbol{x}', t)\,\mathrm{d}t \\ &= \sum_{n=1}^{N_{\mathrm{POD}}} \lambda^{(n)} \Phi_i^{(n)}(\boldsymbol{x}) \Phi_j^{(n)*}(\boldsymbol{x}') \end{aligned}$$

with T being a sufficiently long period of time for which the space–time signal $\boldsymbol{u}(\boldsymbol{x}, t)$ is known and with N_{POD} being the number of POD modes, i. e., the size of the eigenvalue problem (22.76). Note that the eigenfunctions arising from this decomposition are purely spatial.

Discussion of the Size of the Eigenvalue Problem

Given M, the number of spatial points of the snapshots data, and n_c, the number of components of the variable $\boldsymbol{u}$ used for the decomposition, $N_{\mathrm{POD}} = M \times n_c$, $M = N_x \times N_y \times N_z$, where N_x, N_y and N_z are the number of nodes of the experimental or numerical grid, respectively, in the X, Y and Z directions. Now, suppose one performs a detailed numerical simulation or one employs a modern measurement technique such as particle image velocimetry in fluid mechanics. In each case, a large number of grid points M can be obtained and the size of the POD problem can then quickly become too large to be solved with a good numerical precision even with numerical library dedicated to this kind of problem, like the ARPACK library [22.61].

Nevertheless, as will be demonstrated in Sect. 22.4.8, the POD method can be viewed as the generalization of the harmonic decomposition to the inhomogeneous directions. So one way to take into account this size constraint with the classical POD approach is to decompose

the flow directions in homogeneous and inhomogeneous directions as was done in general in experimental approaches [22.25, 30].

Now, suppose that the number of ensemble members deemed adequate for a description of the process is N_t with $N_t \ll M$ (the question of determining N_t is not addressed), then even if the eigenvalue problem can be accurately solved, time can be saved in solving an eigenvalue problem of size N_t. This remark is at the heart of the method of snapshots.

22.4.6 Snapshot POD

The snapshot POD method, suggested by *Sirovich* [22.62–64], is the exact symmetry of the classical POD. The average operator $\langle . \rangle$ is evaluated as a space average over the domain Ω of interest:

$$\langle \cdot \rangle = \int_{\Omega} \cdot \, \mathrm{d}\boldsymbol{x}$$

and the variable $\boldsymbol{X}$ is assimilated to time t.

The principle of the snapshot POD method is schematically described in Fig. 22.17.

The Discrete Eigenvalue Problem

To derive the discrete eigenvalue problem corresponding to the snapshot POD, we assume that $\boldsymbol{\Phi}$ has a special form in terms of the original data:

$$\boldsymbol{\Phi}(\boldsymbol{x}) = \sum_{k=1}^{N_t} a(t_k)\boldsymbol{u}(\boldsymbol{x}, t_k) \,, \tag{22.77}$$

where the coefficients $a(t_k)$, $k = 1, \ldots, N_t$ are to be determined so that $\boldsymbol{\Phi}$ given by (22.77) provides a maximum

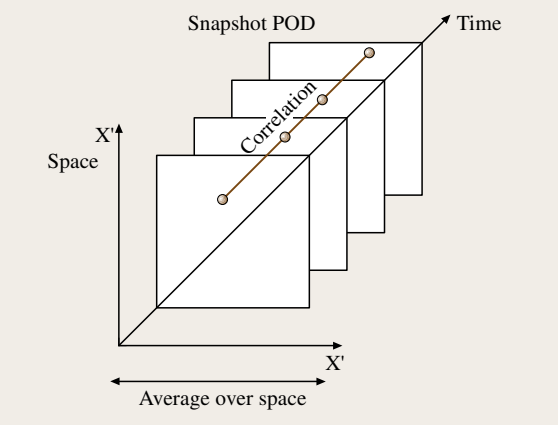

Fig. 22.17 Schematic view of the snapshot POD

for (22.58), i. e., is the solution of equation (22.76), written here for convenience as

$$\int_{\Omega} R(\boldsymbol{x}, \boldsymbol{x}')\boldsymbol{\Phi}(\boldsymbol{x}')\,\mathrm{d}\boldsymbol{x}' = \lambda\boldsymbol{\Phi}(\boldsymbol{x}) \,. \tag{22.78}$$

More exactly, the properties of the span of the POD eigenfunctions guarantee that such a development exists [22.24].

The two-point spatial correlation tensor $R(\boldsymbol{x}, \boldsymbol{x}')$ is estimated under stationarity and ergodicity assumptions as:

$$\begin{aligned} R(\boldsymbol{x}, \boldsymbol{x}') &= \frac{1}{T}\int_{T} \boldsymbol{u}(\boldsymbol{x}, t) \otimes \boldsymbol{u}^*(\boldsymbol{x}', t)\,\mathrm{d}t \\ &= \frac{1}{N_t}\sum_{i=1}^{N_t} \boldsymbol{u}(\boldsymbol{x}, t_i) \otimes \boldsymbol{u}^*(\boldsymbol{x}', t_i) \,. \end{aligned}$$

Substituting this expression of R and the decomposition (22.77) of $\boldsymbol{\Phi}$ into (22.78), we obtain

$$\begin{aligned} &\sum_{i=1}^{N_t}\left[\sum_{k=1}^{N_t}\frac{1}{N_t}\left(\int_{\Omega}\boldsymbol{u}(\boldsymbol{x}', t_k)\cdot\boldsymbol{u}^*(\boldsymbol{x}', t_i)\,\mathrm{d}\boldsymbol{x}'\right)a(t_k)\right] \\ &\quad\times\boldsymbol{u}(\boldsymbol{x}, t_i) \\ &= \lambda\sum_{k=1}^{N_t} a(t_k)\boldsymbol{u}(\boldsymbol{x}, t_k) \end{aligned}$$

and we conclude that a sufficient condition for the coefficients $a(t_k)$ to be a solution of (22.78) is to verify that

$$\begin{aligned} &\sum_{k=1}^{N_t}\frac{1}{N_t}\left[\boldsymbol{u}(\boldsymbol{x}', t_k), \boldsymbol{u}^*(\boldsymbol{x}', t_i)\right]a(t_k) = \lambda a(t_i) \,, \\ &i = 1, \ldots, N_t \,. \end{aligned} \tag{22.79}$$

This can be rewritten as the eigenvalue problem

$$\boldsymbol{C}\boldsymbol{V} = \lambda\boldsymbol{V} \,, \tag{22.80}$$

where

$$C_{ki} = \frac{1}{N_t}\int_{\Omega}\boldsymbol{u}(\boldsymbol{x}, t_k)\cdot\boldsymbol{u}^*(\boldsymbol{x}, t_i)\,\mathrm{d}\boldsymbol{x} \quad \text{and}$$

$$\boldsymbol{V} = [a(t_1), a(t_2), \ldots, a(t_{N_t})]^{\mathrm{T}} \,.$$

Note that, in order for (22.79) to be a necessary condition, one needs to assume that the observations $\boldsymbol{u}(\boldsymbol{x}, t_i)$, $i = 1, \ldots, N_\mathrm{t}$ are linearly independent.

Since C is a nonnegative Hermitian matrix, it has a complete set of orthogonal eigenvectors

$$\boldsymbol{V}^{(1)} = \left[a^{(1)}(t_1), a^{(1)}(t_2), \ldots, a^{(1)}(t_{N_\mathrm{t}})\right]^\mathrm{T},$$
$$\boldsymbol{V}^{(2)} = \left[a^{(2)}(t_1), a^{(2)}(t_2), \ldots, a^{(2)}(t_{N_\mathrm{t}})\right]^\mathrm{T}, \ldots,$$
$$\boldsymbol{V}^{(N_\mathrm{t})} = \left[a^{(N_\mathrm{t})}(t_1), a^{(N_\mathrm{t})}(t_2), \ldots, a^{(N_\mathrm{t})}(t_{N_\mathrm{t}})\right]^\mathrm{T}$$

along with a set of eigenvalues $\lambda^{(1)} \geq \lambda^{(2)} \geq \ldots \geq \lambda^{(N_\mathrm{t})} \geq 0$. Now, for reasons of simplicity, we can impose that the projection coefficients $a(t_k)$, $k = 1, \ldots, N_\mathrm{t}$ verify the same orthogonality conditions as for the classical POD. Then we can normalize the temporal eigenfunctions $\boldsymbol{V}^{(i)}$ by requiring that

$$\frac{1}{N_\mathrm{t}}(\boldsymbol{V}^{(n)}, \boldsymbol{V}^{(m)}) = \frac{1}{N_\mathrm{t}} \sum_{k=1}^{N_\mathrm{t}} a^{(n)}(t_k) a^{(m)*}(t_k) = \lambda^{(n)} \delta_{nm} .$$

It is now easy to check that, if the POD eigenfunctions $\boldsymbol{\Phi}^{(n)}(\boldsymbol{x})$ are not estimated via (22.77) but as

$$\boldsymbol{\Phi}^{(n)}(\boldsymbol{x}) = \frac{1}{N_\mathrm{t} \lambda^{(n)}} \sum_{k=1}^{N_\mathrm{t}} a^{(n)}(t_k) \boldsymbol{u}(\boldsymbol{x}, t_k) , \tag{22.81}$$

then the spatial modes are orthonormal

$$\int_\Omega \boldsymbol{\Phi}^{(n)}(\boldsymbol{x}) \cdot \boldsymbol{\Phi}^{(m)}(\boldsymbol{x}) \, \mathrm{d}\boldsymbol{x} = \delta_{nm} .$$

The Continuous Eigenvalue Problem

So far, the snapshot POD method was presented as by *Sirovich* in his original work [22.62–64]. Therefore the eigenvalue problem (22.80) is discrete and not continuous, as was defined the eigenvalue problem (22.76) derived for the classical POD. However, deducing an integral Fredholm equation from (22.80) is immediate; we obtain

$$\int_T C(t, t') a^{(n)}(t') \, \mathrm{d}t' = \lambda^{(n)} a^{(n)}(t) , \tag{22.82}$$

where $C(t, t')$ is the *two-point temporal correlation tensor* defined as

$$C(t, t') = \frac{1}{T} \int_\Omega u_i(\boldsymbol{x}, t) u_i(\boldsymbol{x}, t') \, \mathrm{d}\boldsymbol{x} = \frac{1}{T} \sum_{n=1}^{N_\mathrm{POD}} a^{(n)}(t) a^{(n)*}(t') .$$

where in this definition, the summation over i is implicit.

The main properties of the snapshot POD are the following:

1. The eigenfunctions are purely time dependent.
2. No cross-correlations appear in the kernel.
3. The homogeneity hypothesis is not required to lower the size of the eigenvalue problem.
4. Linear independence of the snapshots is assumed.
5. The size of the eigenvalue problem (22.82) is $N_\mathrm{POD} = N_\mathrm{t}$. Then, as was mentioned in Sect. 22.4.5, the snapshot POD drastically reduces the computational effort when M, the number of spatial points in the snapshots data, is much greater than N_t. For this reason, whenever this condition is fulfilled, the snapshot POD is preferred.

22.4.7 Common Properties of the Two POD Approaches

General Properties

Whatever the particular method used to determine the spatial and temporal POD eigenfunctions, they fulfil the following properties:

1. Each space–time realization $u_i(\boldsymbol{x}, t)$ can be expanded into orthogonal basis functions $\Phi_i^{(n)}(\boldsymbol{x})$ with uncorrelated coefficients $a^{(n)}(t)$:

$$u_i(\boldsymbol{x}, t) = \sum_{n=1}^{N_\mathrm{POD}} a^{(n)}(t) \Phi_i^{(n)}(\boldsymbol{x}) .$$

2. The spatial modes $\boldsymbol{\Phi}^{(n)}(\boldsymbol{x})$ are specified to be orthonormal:

$$\int_\Omega \boldsymbol{\Phi}^{(n)}(\boldsymbol{x}) \cdot \boldsymbol{\Phi}^{(m)}(\boldsymbol{x}) \, \mathrm{d}\boldsymbol{x} = \delta_{nm} .$$

3. The temporal modes $a^{(n)}(t)$ are orthogonal:

$$\frac{1}{T} \int_T a^{(n)}(t) a^{(m)*}(t) \, \mathrm{d}t = \lambda^{(n)} \delta_{nm} .$$

Incompressibility and Boundary Conditions

The spatial basis functions $\Phi_i^{(n)}(\boldsymbol{x})$ can be calculated from the velocities $u_i(\boldsymbol{x}, t)$ and the coefficients $a^{(n)}(t)$ by integrating over a sufficiently long period of time T and normalizing by the eigenvalues $\lambda^{(n)}$:

$$\Phi_i^{(n)}(\boldsymbol{x}) = \frac{1}{T\lambda^{(n)}} \int_T u_i(\boldsymbol{x}, t) a^{(n)*}(t)\,\mathrm{d}t\ . \tag{22.83}$$

The POD basis functions are then represented as linear combinations of instantaneous velocity fields. All the properties of the snapshots that can be written as linear and homogeneous equations pass directly to the POD basis functions. For example, if the snapshots are divergence free, then we obtain divergence-free POD basis functions

$$\nabla \cdot \boldsymbol{u} = 0 \Longrightarrow \nabla \cdot \boldsymbol{\Phi}^{(n)} = 0 \quad \forall n = 1, \ldots, N_{\mathrm{POD}}\ .$$

If the snapshots satisfy homogeneous Dirichlet boundary conditions then we also obtain POD basis functions satisfying homogeneous boundary conditions.

Snapshot or Classical POD?

As presented in Sect. 22.4.5, 4.6, two different POD approaches exist: the classical POD and the snapshot POD; how then can we choose the pertinent method for each practical configuration? The answer is mainly determined by the particular data set available for the evaluation of the kernels.

On the one hand, data obtained by numerical simulations like direct numerical simulation or large-eddy simulation can be highly resolved in space and time but due to cost considerations only a very short time sample is simulated. In the same vein, a good spatial resolution can be obtained by particle image velocimetry, but associated with a poor temporal resolution. These two configurations, characterized by a moderate time history and high spatial resolution, correspond to situations for which the two-point temporal correlation tensor $C(t, t')$ is statistically well converged.

On the other hand, experimental approaches such as hot-wire anemometry or laser Doppler anemometry provide a well-defined time description but with limited spatial resolution. These measurements techniques enabled long time histories and moderate spatial resolution. Therefore, the two-point spatial correlation tensor $R_{ij}(\boldsymbol{x}, \boldsymbol{x}')$ is statistically well converged.

In conclusion, the data issued from an experimental approach will generally be treated using the classical method and data issued from numerical simulations by the snapshots method. An exception is the case of data sets obtained from particle image velocimetry.

22.4.8 POD and Harmonic Analysis

As long as the domain $\mathcal{D}$ defined in (22.60) is bounded, the Hilbert–Schmidt theory applies [22.46], and all the properties stated in Sect. 22.4.3 hold. It is thus necessary to pay special attention to flow directions assumed to be homogeneous, stationary or periodic.

A First Approach: Homogeneity in One Direction

As a first approach, we can assume, for example, that the spatial direction OX_3 is homogeneous (a generalization including other directions is straightforward). If OX_3 is homogeneous then the two-point correlation $R(\boldsymbol{x}, \boldsymbol{x}')$ depends only on the difference $r_3 = x_3' - x_3$ of the two coordinates in the OX_3 direction:

$$\begin{aligned} &R_{ij}\left(x_1, x_1', x_2, x_2', x_3, x_3', t, t'\right) \\ &= R_{ij}\left(x_1, x_1', x_2, x_2', t, t'; r_3\right)\ . \end{aligned}$$

Splitting the space–time variable $\boldsymbol{X} = (x_1, x_2, x_3, t)$ into a homogeneous variable x_3 and an inhomogeneous variable $\boldsymbol{\chi} = (x_1, x_2, t)$, the integral Fredholm equation (22.60) is written

$$\begin{aligned} &\sum_{j=1}^{n_c} \int_{\mathcal{D}'} \int_{-\infty}^{+\infty} R_{ij}\left(\boldsymbol{\chi}, \boldsymbol{\chi}'; x_3 - x_3'\right) \Phi_j\left(\boldsymbol{\chi}', x_3'\right) \mathrm{d}\boldsymbol{\chi}'\,\mathrm{d}x_3' \\ &= \lambda \Phi_i(\boldsymbol{\chi}; x_3)\ . \end{aligned} \tag{22.84}$$

Under the homogeneity hypothesis, we may develop the spatial eigenfunction Φ_l in a Fourier series decomposition as:

$$\Phi_l(\boldsymbol{\chi}; r_3) = \sum_{k_3=-\infty}^{+\infty} \hat{\Phi}_l(\boldsymbol{\chi}; k_3) \exp(2\pi \mathrm{i} k_3 r_3) \tag{22.85}$$

and introduce Π_{ij}, the Fourier transform of R_{ij} in the direction OX_3:

$$\begin{aligned} &\Pi_{ij}\left(\boldsymbol{\chi}, \boldsymbol{\chi}'; k_3\right) \\ &= \int_{-\infty}^{+\infty} R_{ij}\left(\boldsymbol{\chi}, \boldsymbol{\chi}'; r_3\right) \exp(-2\pi \mathrm{i} k_3 r_3)\,\mathrm{d}r_3 \\ &= \int_{-\infty}^{+\infty} R_{ij}\left(\boldsymbol{\chi}, \boldsymbol{\chi}'; -r_3\right) \exp(2\pi \mathrm{i} k_3 r_3)\,\mathrm{d}r_3\ , \end{aligned} \tag{22.86}$$

where k_3 is the spatial wavenumber associated to r_3.

Substituting expression (22.85) in (22.84), we first obtain

$$\sum_{j=1}^{n_c}\sum_{k_3=-\infty}^{+\infty}\int_{\mathcal{D}'}\int_{-\infty}^{+\infty} R_{ij}(\boldsymbol{\chi},\boldsymbol{\chi}';-r_3)\hat{\Phi}_j(\boldsymbol{\chi}',k_3) \times\exp[2\pi \mathrm{i}k_3(x_3+r_3)]\,\mathrm{d}\boldsymbol{\chi}'\,\mathrm{d}r_3 = \sum_{k_3=-\infty}^{+\infty}\lambda(k_3)\hat{\Phi}_i(\boldsymbol{\chi};k_3).\exp(2\pi \mathrm{i}k_3x_3)\,. \quad (22.87)$$

Then, replacing the two-point correlation R_{ij} by his Fourier transform Π_{ij} defined by (22.86), the Fredholm equation becomes

$$\sum_{k_3=-\infty}^{+\infty}\left[\sum_{j=1}^{n_c}\int_{\mathcal{D}'}\Pi_{ij}(\boldsymbol{\chi},\boldsymbol{\chi}';k_3)\hat{\Phi}_j(\boldsymbol{\chi}',k_3)\,\mathrm{d}\boldsymbol{\chi}'\right] \times\exp(2\pi \mathrm{i}k_3x_3) = \sum_{k_3=-\infty}^{+\infty}\lambda(k_3)\hat{\Phi}_i(\boldsymbol{\chi};k_3).\exp(2\pi \mathrm{i}k_3x_3)\,. \quad (22.88)$$

Finally, the uniqueness of the Fourier series coefficients implies that the Fredholm equation (22.60) is equivalent to:

$$\sum_{j=1}^{n_c}\int_{\mathcal{D}'}\Pi_{ij}(\boldsymbol{\chi},\boldsymbol{\chi}';k_3)\hat{\Phi}_j(\boldsymbol{\chi}',k_3)\,\mathrm{d}\boldsymbol{\chi}' = \lambda(k_3)\hat{\Phi}_i(\boldsymbol{\chi};k_3)\,. \quad (22.89)$$

The conclusion is that the homogeneity hypothesis in the OX_3 direction decouples the initial POD problem into a set of lower-dimensional problems. For each Fourier wavenumber k_3 the eigenvalue problem to solve is:

$$\sum_{j=1}^{n_c}\int_{\mathcal{D}'}\Pi_{ij}(\boldsymbol{\chi},\boldsymbol{\chi}')\hat{\Phi}_j(\boldsymbol{\chi}')\mathrm{d}\boldsymbol{\chi}' = \lambda\hat{\Phi}_i(\boldsymbol{\chi}) \quad \forall k_3\,. \quad (22.90)$$

Another key result is that, in each homogeneous (or stationary) direction, harmonic functions are solutions of the integral Fredholm equations. Then, as a first approximation, the proper orthogonal decomposition can be viewed as the generalization of the harmonic decomposition to the inhomogeneous directions.

This result is especially useful in systems where the domain $\mathcal{D}$ is of higher dimension. For example, in the study of the three-dimensional turbulent plane mixing layer realized via the classical POD in *Delville* et al. [22.25] and *Ukeiley* et al. [22.30], we appeal to homogeneity in the spanwise (x_3) and streamwise (x_1) directions. Selecting the finite domain $[0, L_1]\times[0, L_3]$ in these variables, we use a mixed Fourier–empirical decomposition of the form:

$$\boldsymbol{u}(\boldsymbol{x},t) = \sqrt{L_1L_3}\int\!\!\int_{-\infty}^{+\infty}\sum_{n=1}^{N_{\mathrm{POD}}} a^{(n)}_{k_1,k_3}(t)\boldsymbol{\Phi}^{(n)}(x_2;k_1,k_3) \times\exp[2\pi \mathrm{i}(k_1x_1+k_3x_3)]\,\mathrm{d}k_1\,\mathrm{d}k_3\,.$$

As detailed in *Delville* et al. [22.25], time is mapped to the streamwise direction through Taylor's hypothesis.

The vector-valued eigenfunctions $\boldsymbol{\Phi}^{(n)}(x_2;k_1,k_3)$ are obtained by solving a Fredholm equation analogous to (22.60) in which the kernel R_{ij} is replaced by the cross-spectral tensor $\Psi_{ij}(x_2,x_2';k_1,k_3)$ defined as the streamwise and spanwise transform of the cross-correlation tensor. More details are given in *Cordier* [22.65]; see also *Delville* et al. [22.25] and *Ukeiley* et al. [22.30].

Phase Indetermination

The *phase indetermination* is one of the most important limitations of the POD. This indetermination is due to the use of two-point correlations and, as will be demonstrated in the following, appears only for directions where an harmonic decomposition is used.

Suppose that the eigenfunction $\hat{\Phi}_j(\boldsymbol{\chi}';k_3)$ is a solution of (22.89). Then it can easily be proven that every function $\hat{\Phi}_j(\boldsymbol{\chi}';k_3)\theta(k_3)$, where $\theta(k_3)$ is a random phase function, will also be a solution. The phase information between the different modes is lost, and the eigenfunctions $\hat{\Phi}_i(\boldsymbol{\chi};k_3)$ are known up to an arbitrary function $\theta(k_3)$, which needs to be determined. In particular, for classical POD, it is impossible to obtain directly a description of the preferred modes in the physical space. However, a description of the dominant modes can be obtained by using a complementary method called *the shot-noise theory* fully described in *Herzog* [22.66], and *Moin* and *Moser* [22.67]. The reader is referred to *Delville* et al. [22.25] for an application of the shot-noise theory to recover the dominant modes of a three-dimensional turbulent mixing layer from the POD eigenfunctions determined by classical POD.

An alternative way is to build, from the dominant POD eigenfunctions, a low-order model by use of a Galerkin projection of the governing equations onto

the POD modes, leading to a low-order dynamical system described by a set of ordinary differential equations. In this case, these equations themselves drive the missing spectral phase information. This approach has been successfully addressed for the wall region of a turbulent boundary layer in *Aubry* et al. [22.29] and for a plane turbulent mixing layer in *Ukeiley* et al. [22.30]. Naturally, this kind of low-order model is particularly suited for active flow control studies.

22.4.9 Typical Applications to Fluid Mechanics

POD in the Mixing Layer

In this section, we briefly present a few results obtained from the application of classical POD to experimental measurements obtained in a two-dimensional plane turbulent mixing layer [22.68]. The streamwise and transverse instantaneous velocity components are determined by using a rake of 12 equally spaced X-wires uniformly distributed according to the transverse y-direction of the flow. In the present study, only the spatial direction y (mean gradient, inhomogeneous) and the time delay τ are considered. The flow being stationary, a Fourier transform has to be used in the time direction before applying POD (Sect. 22.4.8). Of course, this approach is limited by the fact that the three-dimensional aspect of the flow cannot be assessed; only one slice of the flow is viewed here. Hence the full three-dimensional behavior of the flow is not analyzed. However, useful information on the global organization of the flow can be outlined.

Following the classical POD method described in Sect. 22.4.5, the dominant structure of the flow can be determined from the following Fredholm equation:

$$\sum_{j=1}^{n_c} \int_{\Omega} \Psi_{ij}(y, y'; f) \Phi_j^{(n)}(y'; f) \mathrm{d}y' = \lambda^{(n)}(f) \Phi_i^{(n)}(y; f) , \qquad (22.91)$$

where n_c is the number of velocity components on which POD is performed, and where the cross-spectrum $\Psi_{ij}(f)$ is the temporal Fourier transform of the two-point space–time correlations

$$R_{ij}(y, y'; \tau) = \left\langle u_i'(y, t) u_j'(y', t+\tau) \right\rangle .$$

The Fourier transform of the velocity can be retrieved from the eigenfunctions Φ_i

$$\hat{u}_i'(y; f) = \sum_{n=1}^{N_{\mathrm{POD}}} a^{(n)}(f) \Phi_i^{(n)}(y; f) ,$$

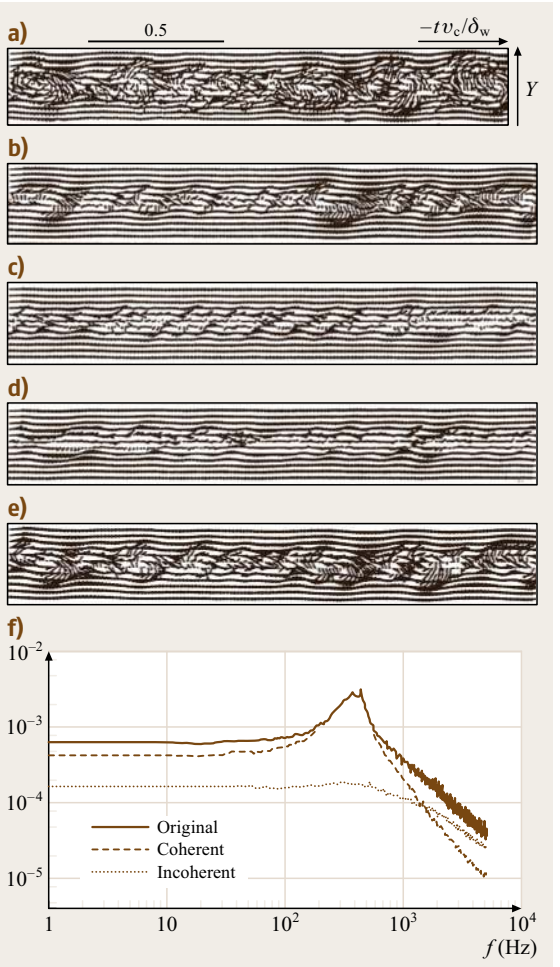

Fig. 22.18a–f Example of POD application in a turbulent plane mixing layer. A rake of 12 X-wire probes is used to measure the instantaneous distribution of two velocity components across the mixing layer. **(a)** Original measurements. **(b)** First POD mode. **(c)** Second POD mode. **(d)** Third POD mode. **(e)** Contribution of the first three POD modes. **(f)** Energy spectrum of the transverse velocity component. *Original* corresponds to the hot-wire measurements, *Coherent* to the contribution of the first three POD modes and *Incoherent* to the remaining POD modes

where $a^{(n)}(f)$ is found from

$$a^{(n)}(f) = \int_{\Omega} \hat{u}_i'(y; f) \Phi_i^{(n)}(y; f) \mathrm{d}y . \qquad (22.92)$$

In terms of structure identification, the participation of any POD mode in the instantaneous flow field can be

considered. Figure 22.18 shows, for a selected sample, an example of the instantaneous velocity field plotted in a frame moving with a constant convection velocity U_c using a Taylor hypothesis based on U_c for the longitudinal direction. Here, this convection velocity is chosen arbitrarily as the average of the two velocity streams of the mixing layer. The organization, which can be visually detected from the original velocities (Fig. 22.18a), is relatively well reconstructed by the first POD mode (Fig. 22.18b). However, the spatial extent of the events in the y direction is generally underestimated, and higher modes (Fig. 22.18c,d) are needed to improve this (Fig. 22.18e).

The power spectra deduced from the original, coherent, and incoherent contributions to the transverse velocity field are superimposed on Fig. 22.18f). The coherent flow field has a similar spectral distribution to the original (total) flow until the frequency 500 Hz, while the incoherent flow is uncorrelated and exhibits a flat energy spectrum in this frequency domain. We then see that the POD coherent component captures the strongest frequency peak, lying at around 400 Hz and associated with the two-dimensional Kelvin–Helmholtz instability. At high frequencies, the spectral slope obtained for the incoherent spectrum is similar to that deduced from the original spectrum, while the coherent spectrum exhibits a different slope. The spectral content of the small scales has then been well reconstituted with the POD incoherent field. Finally, the background fluctuations exhibit a spectrum corresponding to a quasihomogeneous equilibrium turbulence. This figure also shows that POD coherent structures are not localized in the spectral domain. They correspond to multiple scales and differ from the usual approaches of Fourier filtering in time or space.

The Complementary Technique in the Mixing Layer

In order to perform the projection required to obtain the random coefficients $a^{(n)}(f)$ from the POD, it is necessary to have knowledge of the flow field at all points in space (22.92). Depending on the measurement apparatus, this is not always possible. For example, it is sometimes difficult to operate several hot-wire probes simultaneously. On the other hand, the determination of the correlation tensor used for applying POD only requires a two-point measurement procedure. In this case, the linear stochastic estimation (see Sect. 22.4.6 for further details), also based on two-point correlations, allows the estimation of the raw data on which POD can be used as a structure identification process (by retaining only a small number of modes). This approach, called a complementary method, was introduced by *Bonnet* et al. [22.69].

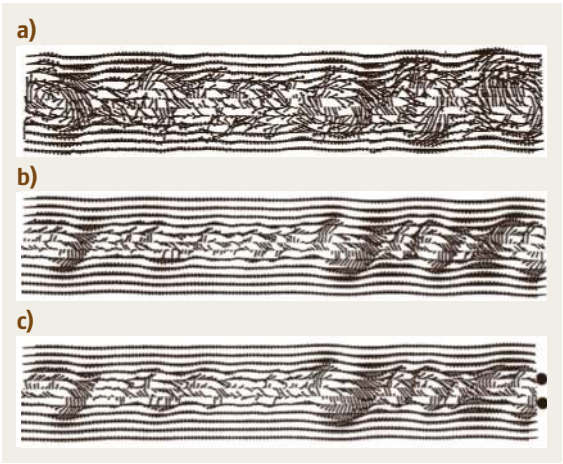

Fig. 22.19a–c Application of the complementary technique to the plane mixing layer. **(a)** Original measurements. **(b)** Direct application of POD. **(c)** Application of the complementary technique (two points of reference were used for the linear stochastic estimation)

Mathematically, the stochastic estimates of the random coefficients are now calculated from:

$$a_{\text{est}}^{(n)}(f) = \int_{\Omega} u'_{i,\text{est}}(y;\, f)\Phi_i^{(n)}(y;\, f)\,\mathrm{d}y\,,$$

where $u'_{i,\text{est}}(y;\, f)$ is either a single or multipoint linear stochastic estimate of the velocity field and $\Phi_i^{(n)}(y;\, f)$ is obtained from the original POD eigenvalue problem. The estimated velocity can be reconstructed in Fourier space by

$$\hat{u}'_i(y;\, f) = \sum_{n=1}^{N_{\text{POD}}} a_{\text{est}}^{(n)}(f)\Phi_i^{(n)}(y;\, f)\,,$$

and then inversely transformed to obtain $\hat{u}'_i(y, t)$. The example plotted in Fig. 22.19 illustrates this procedure applied to the same data as used in Fig. 22.18.

22.4.10 POD Galerkin

General Methodology

Before going into the details of the application of the Galerkin projection for the POD eigenfunctions, we first recall the basic ideas of Galerkin projection.

Galerkin projection is a special case of *weighted residual methods* [22.70]. These methods are dedicated

to solve functional equations, such as ordinary (ODE) or partial (PDE) differential equations, or integral equations. For example, consider the equation

$$\mathcal{L}(\boldsymbol{u}) = 0 \tag{22.93}$$

defined in a domain Ω, where $\mathcal{L}$ is some differential operator. The Galerkin method is an approximation to the true solution of (22.93) sought by weighting the residual of the differential equation. Assume that $\boldsymbol{U}$ is an approximate solution to (22.93). Substitution of $\boldsymbol{U}$ for $\boldsymbol{u}$ in (22.93) results in a nonzero residual $r = \mathcal{L}(\boldsymbol{U}) \neq 0$.

The best approximation for $\boldsymbol{U}$ is that which reduces the residual r to the least value at all points in the domain Ω. The weighted residual method enforces the condition

$$R_j = \int_{\Omega} w_j r \, \mathrm{d}\Omega = 0 \,, \tag{22.94}$$

where the R_j are the weighted residual integrals and w_j are the weighting functions. In the Galerkin method, the weighting functions are chosen to be the same as the basis functions used in the expansion of the approximate solution. Hence, if $\boldsymbol{U}$ is approximated by the expansion

$$\boldsymbol{U}(\boldsymbol{x}) = \sum_{i=1}^{\infty} \chi_i \boldsymbol{\varphi_i}(\boldsymbol{x}) \,, \tag{22.95}$$

where $\boldsymbol{\varphi_i}(\boldsymbol{x})$ are the basis functions and χ_i are the coefficients to be determined, then the weighting functions are selected as $w_j = \boldsymbol{\varphi_j}(\boldsymbol{x})$, $j = 1, \ldots, +\infty$. The fact that the unknown $\boldsymbol{u}$ solution of (22.93) is a member of an infinite-dimensional space is a practical difficulty. The discretization of the Galerkin procedure then consists of truncating the sum in (22.95) at a finite index $i_{\max}$, thus rendering the problem a finite dimensional one. Therefore, (22.94) becomes

$$\int_{\Omega} \boldsymbol{\varphi_j}(\boldsymbol{x}) \mathcal{L}(\boldsymbol{U}) \mathrm{d}\Omega = 0 \,, \quad j = 1, \ldots, i_{\max} \,. \tag{22.96}$$

If the definition (22.73) of the inner product is introduced, then equation (22.96) further simplifies to

$$\left\{ \mathcal{L}\left[\sum_{i=1}^{i_{\max}} \chi_i \boldsymbol{\varphi_i}(\boldsymbol{x}) \right], \boldsymbol{\varphi_j} \right\} = 0 \,, \quad j = 1, \ldots, i_{\max} \,. \tag{22.97}$$

Finally, the Galerkin Projection is equivalent to impose the $i_{\max}$ scalar products defined by equation (22.97) to vanish.

For such an approach to work [22.71], the two following requirements should be satisfied:

1. the function space $\{\boldsymbol{\varphi_i}\}$ of the basis functions $\boldsymbol{\varphi_i}(\boldsymbol{x})$ must be complete and for practical reasons to become clear in the next section, an orthonormal basis is especially desirable.
2. the basis functions $\boldsymbol{\varphi_i}(\boldsymbol{x})$ must meet the boundary conditions of the problem.

Reduced Order Models Based on POD

From the properties of the POD eigenfunctions $\boldsymbol{\Phi^m}(\boldsymbol{x})$ as described in Sect. 22.4.3 one can immediately see that these eigenfunctions are particularly suited for Galerkin projection.

The Navier–Stokes equations for incompressible flows can be written symbolically as

$$\frac{\partial \boldsymbol{u}}{\partial t} = \boldsymbol{F}(\boldsymbol{u}) \text{ with } \boldsymbol{u} = \boldsymbol{u}(\boldsymbol{x}, t) \boldsymbol{x} \in \Omega \text{ and } t \geq 0 \,, \tag{22.98}$$

where $\boldsymbol{F}$ is a differential operator that contains only spatial derivatives and where Ω is the spatial domain under study. The differential equation (22.98) is mathematically well posed if the system is completed by initial conditions:

$$\boldsymbol{u}(\boldsymbol{x}, t = 0) = \boldsymbol{u_0}(\boldsymbol{x}) \tag{22.99}$$

and boundary conditions. Here, we decide to follow the viewpoint of *Fahl* [22.34] and to formulate the differential equation (22.98) in the general context of boundary control problem for fluid flows. Hence, we assume that the boundary of the domain Γ, can be split into two parts such that Γ_c denotes that part of the boundary where the control is applied and $\Gamma \setminus \Gamma_c$ is the part of the boundary that is not controlled. Then, we can complete the (22.98) with the Dirichlet boundary conditions:

$$\boldsymbol{u}(\boldsymbol{x}, t) = \boldsymbol{h}[\boldsymbol{x}, t;\, \mathrm{d}(t)] \text{ with } \boldsymbol{x} \in \Gamma \text{ and } t \geq 0 \,, \tag{22.100}$$

where d is the control input. More precisely, the boundary conditions can be written as

$$\boldsymbol{h}[\boldsymbol{x}, t;\, \mathrm{d}(t)] = \begin{cases} \gamma(t)\boldsymbol{c}(\boldsymbol{x}) & \boldsymbol{x} \in \Gamma_c, t \geq 0 \,, \\ \boldsymbol{g}(\boldsymbol{x}) & \boldsymbol{x} \in \Gamma \setminus \Gamma_c, t \geq 0 \,, \end{cases} \tag{22.101}$$

where $\gamma(t)$ can be interpreted as the temporal variation of a prescribed control action defined by $\boldsymbol{c}(\boldsymbol{x})$, $\boldsymbol{x} \in \Gamma_c$. For example, this formulation corresponds to flow control

by blowing and suction along a portion of the boundary as considered in *Joslin* et al. [22.72].

The reduced-order model is then derived by Galerkin projection of the PDE (22.98) onto the POD subspace of dimension N_{POD}. The first step is to insert in (22.98) the development of $\boldsymbol{u}$ on the POD basis $\boldsymbol{\Phi}^{(m)}$:

$$\boldsymbol{u}(\boldsymbol{x},t)=\sum_{m=1}^{N_{\mathrm{POD}}} a^{(m)}(t)\boldsymbol{\Phi}^{(m)}(\boldsymbol{x})$$

to obtain (using the notation $\dot{a}=\mathrm{d}a/\mathrm{d}t$)

$$\sum_{m=1}^{N_{\mathrm{POD}}} \dot{a}^{(m)}(t)\boldsymbol{\Phi}^{(m)}(\boldsymbol{x})=\boldsymbol{F}\left(\sum_{m=1}^{N_{\mathrm{POD}}} a^{(m)}(t)\boldsymbol{\Phi}^{(m)}(\boldsymbol{x})\right) . \tag{22.102}$$

The set of spatial eigenfunctions $\boldsymbol{\Phi}^{(m)}(\boldsymbol{x})$ being a basis, the right-hand side of (22.102) can be written as a linear combination of $\boldsymbol{\Phi}$:

$$\boldsymbol{F}\left(\sum_{m=1}^{N_{\mathrm{POD}}} a^{(m)}(t)\boldsymbol{\Phi}^{(m)}(\boldsymbol{x})\right) =\sum_{n}\mathcal{F}^{(n)}\left(a^{(1)},a^{(2)},\dots\right)\boldsymbol{\Phi}^{(n)}(\boldsymbol{x}) .$$

Finally, the Galerkin projection of (22.98) onto the POD eigenfunctions is evaluated as

$$\left(\boldsymbol{\Phi}^{(n)},\frac{\partial \boldsymbol{u}}{\partial t}\right)=\left(\boldsymbol{\Phi}^{(n)},\boldsymbol{F}(\boldsymbol{u})\right)$$

for $n=1,\dots,N_{\mathrm{Gal}}$,

where N_{Gal} is the number of Galerkin modes kept in the projection. From the orthonormality of the eigenfunctions $\boldsymbol{\Phi}^{(m)}(\boldsymbol{x})$, the PDE (22.98) is replaced by a set of ODEs defined by

$$\dot{a}^{(n)}(t)=\mathcal{F}^{(n)}\left(a^{(1)}(t),\dots,a^{(n)}(t)\right) ,$$

$$\text{with } n=1,\dots,N_{\mathrm{Gal}} , \tag{22.103}$$

where

$$\mathcal{F}^{(n)}=\left[\boldsymbol{\Phi}^{(n)},\boldsymbol{F}\left(\sum_{m=1}^{N_{\mathrm{Gal}}} a^{(m)}(t)\boldsymbol{\Phi}^{(m)}(\boldsymbol{x})\right)\right] .$$

(The left-hand side of (22.103) is estimated as

$$\left(\boldsymbol{\Phi}^{(n)},\sum_{m}\dot{a}^{(m)}\boldsymbol{\Phi}^{(m)}(\boldsymbol{x})\right) =\sum_{m}\dot{a}^{(m)}(t)\left(\boldsymbol{\Phi}^{(n)},\boldsymbol{\Phi}^{(m)}\right) .$$

Hence, as previously noted at the beginning of this section, an orthonormal basis is especially desirable because we avoid inverting an $N_{\mathrm{Gal}}\times N_{Gal}$ matrix to solve for $\dot{a}^{(n)}(t)$)

The functions $\mathcal{F}^{(n)}$ are linear if $\boldsymbol{F}$ is a linear operator and, in our case, due to the convective terms in the Navier–Stokes equations, $\mathcal{F}^{(n)}$ are usually quadratic functions of $a^{(n)}$. In *Aubry* et al. [22.29] and *Ukeiley* et al. [22.30], the low-order dynamical system (22.103) have cubic terms because the velocity field is decomposed into mean and fluctuating components ($\boldsymbol{u}=\langle\boldsymbol{u}\rangle+\boldsymbol{u}'$), where the mean is slowly varying in time. The mean may then be described in terms of the fluctuations $\boldsymbol{u}'$, which give rise to Reynolds stresses and then to cubic equations for (22.103). Another enhancement to the basic theory described so far is the modeling of energy transfer to the higher modes (corresponding to the dissipative scales of the flow) neglected in the Galerkin projection procedure. In *Aubry* et al. [22.29], the influence of the missing scales is simply parameterized by a generalization of the Heisenberg spectral model in homogeneous turbulence [22.73] and in *Ukeiley* et al. [22.30] the mean velocity is split into a steady and time-dependent part by choosing cutoff wavenumbers. Other methods for improving the accuracy of the POD reduced-order model are discussed at the end of this section.

To obtain a well-posed mathematical problem, one needs to add a set of initial conditions to the reduced-order model (22.103) and to make sure that the problem (22.103) matches the original boundary conditions (22.100). The initial conditions can be directly inferred from the conditions (22.99) imposed to the original problem

$$a^{(n)}(t=0)=a_0^{(n)} \text{ , where } a_0^{(n)}=\left(\boldsymbol{u_0}(\boldsymbol{x}),\boldsymbol{\Phi}^{(n)}\right) .$$

For the boundary conditions, the answer is not so direct because it depends mainly of the type of boundary conditions applied, homogeneous or nonhomogeneous boundary conditions. For this reason, this question is postponed to the next subsection.

To sum up, combining the Galerkin projection methodology and the optimality of convergence of POD eigenfunctions (Sect. 22.4.3), we demonstrate that high-dimensional models represented by partial differential equations (PDE) can be replaced by low-dimensional dynamical models of nonlinear ordinary differential equations (ODE).

Problem of Boundary Conditions

According to (22.83), when the Navier–Stokes equations (NSE) are subjected to homogeneous Dirichlet boundary conditions (for example, $\boldsymbol{h}(\boldsymbol{x},t;c(t))=\boldsymbol{0}$), the POD

basis functions inherit these boundary conditions. Therefore, the reduced-order models developed by Galerkin projection of the NSE on the POD subspace are equivalent to the original NSE. More precisely, we can only argue that the system of ODEs (22.103) are mathematically equivalent to the original problem (22.98). We are sure that there exists a solution of the reduced-order model (22.103) that lies on the manifold that is defined by the boundary conditions of the original problem. However, the fundamental question if whether a flow can be represented exactly by a finite-dimensional basis of POD eigenfunctions and the question of stability of that manifold are still not fully answered. Issues concerning the stability and the accuracy of a Galerkin projection are discussed in *Iollo* [22.58] and *Iollo* et al. [22.59]. The possible connections between the stability properties of the manifold and the stability properties of the physical phenomenon are addressed in *Rempfer* [22.71]. The expansion coefficients $a_{DS}^{(n)}(t)$, $n = 1, \ldots, N_{Gal}$ that are solutions of the dynamical system (22.103) can then be used to compute the reduced-order solution

$$\boldsymbol{u}_{\mathrm{DS}}(\boldsymbol{x}, t) = \sum_{n=1}^{N_{\mathrm{Gal}}} a_{\mathrm{DS}}^{(n)}(t)\boldsymbol{\Phi}^{(n)}(\boldsymbol{x}) ,$$

where the subscript DS denotes the dynamical system approximation to the original solution $\boldsymbol{u}(\boldsymbol{x}, t)$ of the NSE.

Now we consider the NSE with nonhomogeneous Dirichlet boundary conditions defined by (22.101). Assume that the snapshots data $\boldsymbol{u}(\boldsymbol{x}, t_i)$, $i = 1, \ldots, N_{\mathrm{t}}$ of the input ensemble $\mathcal{U}$ satisfy the required (nonhomogeneous) boundary conditions. Due to (22.83), the POD basis functions are no longer suitable to use in a Galerkin projection. The solution of this problem is to transform the actual problem to a problem with homogeneous boundary conditions.

When $\boldsymbol{h}(\boldsymbol{x}, t; d(t))$ does not depend on time t, for example $\boldsymbol{h}(\boldsymbol{x}, t; d(t)) = \boldsymbol{g}(\boldsymbol{x})$ for all $\boldsymbol{x} \in \Gamma$ and $t \geq 0$, *Sirovich* [22.62] suggests overcoming this difficulty by computing the POD basis functions for the fluctuations around the mean flow field. Given N_{t} time snapshots, the mean velocity $\langle \boldsymbol{u}(\boldsymbol{x}, t)\rangle = \frac{1}{N_{\mathrm{t}}} \sum_{i=1}^{N_{\mathrm{t}}} \boldsymbol{u}(\boldsymbol{x}, t_i)$ is first computed as an ensemble average. The POD eigenfunctions are then estimated using the modified input data $\mathcal{U}' = \{\boldsymbol{u}(\boldsymbol{x}, t_1) - \langle \boldsymbol{u}(\boldsymbol{x}, t)\rangle, \ldots, \boldsymbol{u}(\boldsymbol{x}, t_{N_{\mathrm{t}}}) - \langle \boldsymbol{u}(\boldsymbol{x}, t)\rangle\}$ (see [22.35] for an example). Due to its construction, the mean flow $\langle \boldsymbol{u}(\boldsymbol{x}, t)\rangle$ is a solenoidal field and satisfies the prescribed nonhomogeneous boundary conditions. Furthermore, each modified snapshot $\boldsymbol{u}(\boldsymbol{x}, t_i) - \langle \boldsymbol{u}(\boldsymbol{x}, t)\rangle$ is also divergence free, but satisfies homogeneous Dirichlet boundary conditions. In the case of time-independent nonhomogeneous boundary conditions, the reduce- order solution can be computed as

$$\boldsymbol{u}_{\mathrm{DS}}(\boldsymbol{x}, t) = \langle \boldsymbol{u}(\boldsymbol{x}, t)\rangle + \sum_{m=1}^{N_{\mathrm{Gal}}} a_{\mathrm{DS}}^{(m)}(t)\boldsymbol{\Phi}^{(m)}(\boldsymbol{x}) ,$$

where the coefficients $a_{DS}^{(n)}(t)$, $n = 1, \ldots, N_{Gal}$ are the solutions of the dynamical system (22.103).

For boundary control problems, the more interesting case is the one where the Dirichlet boundary conditions $\boldsymbol{h}(\boldsymbol{x}, t; d(t))$ defined by (22.101) depend on time t. In order to match these boundary conditions, *Graham* et al. [22.56], *Ravindran* [22.21, 22] and *Fahl* [22.34] propose searching for the reduced-order solution of the low-order dynamical system (22.103) as

$$\boldsymbol{u}_{\mathrm{DS}}(\boldsymbol{x}, t) = \langle \boldsymbol{u}(\boldsymbol{x}, t)\rangle + \gamma(t)\boldsymbol{u}_c(\boldsymbol{x}) + \sum_{m=1}^{N_{\mathrm{Gal}}} a_{\mathrm{DS}}^{(m)}(t)\boldsymbol{\Phi}^{(m)}(\boldsymbol{x}) ,$$

where $\boldsymbol{u}_c(\boldsymbol{x})$, $\boldsymbol{x} \in \Omega$ is a reference flow field, describing how the control action $\gamma(t)\boldsymbol{c}(\boldsymbol{x})$, $\boldsymbol{x} \in \Gamma_c$, $t \geq 0$ influences the flow and satisfying the following boundary conditions

$$\gamma(t)\boldsymbol{u}_c(\boldsymbol{x}) = \begin{cases} \gamma(t)\boldsymbol{c}(\boldsymbol{x}) , & \boldsymbol{x} \in \Gamma_c, t \geq 0 , \\ \boldsymbol{0} & \boldsymbol{x} \in \Gamma \setminus \Gamma_c, t \geq 0 . \end{cases}$$

Similar to the procedure presented for the time-independent case, a mean velocity $\langle \boldsymbol{u}(\boldsymbol{x}, t)\rangle$ is first computed as the ensemble average of the modified input data defined as $\mathcal{U}' = \{\boldsymbol{u}(\boldsymbol{x}, t_1) - \gamma(t_1)\boldsymbol{u}_c(\boldsymbol{x}), \ldots, \boldsymbol{u}(\boldsymbol{x}, t_{N_{\mathrm{t}}}) - \gamma(t_{N_{\mathrm{t}}})\boldsymbol{u}_c(\boldsymbol{x})\}$. Afterward, the POD basis functions are estimated with the input collection $\mathcal{U}'' = \{\boldsymbol{u}(\boldsymbol{x}, t_1) - \gamma(t_1)\boldsymbol{u}_c(\boldsymbol{x}) - \langle \boldsymbol{u}(\boldsymbol{x}, t)\rangle, \ldots, \boldsymbol{u}(\boldsymbol{x}, t_{N_{\mathrm{t}}}) - \gamma(t_{N_{\mathrm{t}}})\boldsymbol{u}_c(\boldsymbol{x}) - \langle \boldsymbol{u}(\boldsymbol{x}, t)\rangle\}$.

Since $(\boldsymbol{u}(\boldsymbol{x}, t_i) - \gamma(t_i)\boldsymbol{u}_c(\boldsymbol{x}))|_{\Gamma_c} = \boldsymbol{0}$ and $\langle \boldsymbol{u}(\boldsymbol{x}, t)\rangle$ matches all other nonhomogeneous boundary conditions, the POD basis functions satisfy homogeneous boundary conditions on the whole domain. This approach is used in *Bergmann* et al. [22.35] to incorporate the boundary control for the cylinder wake into the POD-based reduced-order model.

Accurate Model Reduction

When the POD-based reduced-order model (22.103) is integrated in time, it yields a set of predicted time histories for the mode amplitudes $a^{(i)}(t)$, which can be compared with the POD temporal eigenfunctions. However, it is now well known that, when the

equations (22.103) are integrated in time with initial conditions obtained from corresponding direct numerical simulations, a gradual drift from the full-state solution to another erroneous state may arise, prohibiting a correct description of the long-term dynamics [22.74]. Even worse, in some cases, the short-term dynamics of the POD model may not be sufficiently accurate to be used as a surrogate model of the original high-fidelity models. Essentially, two sources of numerical errors can be identified. First, the pressure term is often neglected in the Galerkin projection. In many closed flows, it can be demonstrated rigorously that the contribution of the pressure term is exactly zero. For convectively unstable shear layers, as the mixing layer or the wake flow, *Noack* et al. [22.75] proved that neglecting the pressure term may lead to large-amplitude errors in the Galerkin model, requiring the introduction of a pressure-term representation [22.75, 76]. The second source of numerical errors is the truncation involved in the POD Galerkin approach. Indeed, since only the most energetic POD modes are kept, the POD model is not sufficiently dissipative to prevent erroneous time amplifications of its solution. This problem is similar to that of large-eddy simulation, where the energy transfers between the resolved scales and the subgrid scales have to be modeled [22.77]. Recently, Karniadakis employed the same dissipative model, called the spectral vanishing viscosity model (SVVM), to formulate alternative Large Eddy Simulation (LES) approaches [22.78] and to improve the accuracy of POD flow models [22.74]. In *Bergmann* et al. [22.35], the POD model is stabilized by the introduction of a time-dependent eddy-viscosity model estimated for each POD mode as the solution of an auxiliary optimization problem (see [22.79] for a description). This approach can be viewed as a calibration procedure of the POD-Galerkin system similar to the methods recently introduced in *Galletti* et al. [22.76] for the pressure model or in *Couplet* et al. [22.80] for the polynomial coefficients of the system.

22.4.11 Evaluative Summary of the POD Approach

The proper orthogonal decomposition is a powerful and elegant method of data analysis aimed at obtaining low-dimensional approximations of high-dimensional processes. For turbulent flows, the POD approach by itself is neither a theory nor a closure method. However, a better understanding of the role of coherent structures in turbulence generation can be gained with low-order dynamical systems developed by Galerkin projection of the governing equations onto the POD basis functions (see [22.29], for example). On the other hand, the recent invention of microelectromechanical systems has generated substantial interest for control methods for fluid dynamics. The design of reduced-order controllers for fluid system is essential for real-time implementation and the POD method is particularly suited for deriving reduced-order models [22.21, 22, 34, 40].

Among the *advantages* related to the proper orthogonal decomposition, the following points can be underlined.

- The method is objective, methodic, and rigorous: a mathematical framework is provided by the Hilbert–Schmidt theory.
- The POD is a linear method but no linear hypothesis is imposed on the process. The fact that this approach always looks for linear or affine subspaces instead of curved submanifolds makes it computationally tractable. However the POD does not neglect the nonlinearities of the original vector field. If the original dynamical system is nonlinear, then the resulting reduced-order POD model will also typically be nonlinear.
- The POD basis functions are optimal in terms of energy.
- The efficiency of POD increases with the level of inhomogeneity of the process. This method is therefore particularly suited to the analysis of turbulent shear flows. Moreover, as the generalization of Fourier methods to inhomogeneous directions, POD is complementary to harmonic methods.
- Combined with the Galerkin projection procedure, POD provides a powerful method for generating lower-dimensional models of dynamical systems that have a very large or even infinite-dimensional space.

Among the *disadvantages* related to POD are the following.

- The technique requires knowledge of a two-point correlation tensor over a large number of points. Its use is therefore limited by the size of the data sets, which can quickly becomes huge [22.31].
- Due to the use of two-point correlations, phase indetermination appears for directions where an harmonic decomposition has to be used. For classical POD, in particular, complementary techniques are necessary to obtain a description of the preferred modes in the physical space.

- By definition, POD selects structures that are best correlated with the entire fluctuating velocity field. It is therefore not helpful if we want to study a region S that contains only a small fraction of the total kinetic energy. Fortunately, in this type of situation, it is then possible to use the extended POD (EPOD) approach recently introduced by *Borée* [22.81]. Using POD modes computed in the subdomain S only, this method provides a decomposition of the velocity field in the whole domain. This decomposition is such that the extended mode of order p gives the only local contribution to the velocity field that is correlated with the projection of the velocity field onto mode POD of order p in S.
- The nature of the POD basis functions is intrinsically linked to the flow configurations from which they have been derived. The same argument can be used to explain the energetic optimality of the POD basis functions. Therefore, a POD basis determined with a set of realizations of the flow model for a specified control input can perfectly reproduce the dynamics of the flow for a fixed system and may not be sufficient when the system is under the action of a control. In these cases, the POD basis needs to be improved by an adaptive procedure [22.21, 34].

22.5 Conditional Averages and Stochastic Estimation

22.5.1 Conditional Averages

Conditional averaging is a natural way of refining averages to pertain to a more precisely defined set of conditions. It is used extensively in the study of *coherent structures* in turbulent flow. In this section the concepts underlying conditional averaging will be presented briefly, coherent structure concepts will be reviewed, and the method of *conditional eddies* will be explained.

Conditional Averaging Concepts

Let $\tilde{\boldsymbol{q}}$ be any random quantity, and denote the mean value of $\tilde{\boldsymbol{q}}$ by $\langle\tilde{\boldsymbol{q}}\rangle$, where the brackets denote an averaging operation. As usual, we separate $\tilde{\boldsymbol{q}}$ into a sum of its mean and its fluctuation about the mean:

$$\tilde{\boldsymbol{q}} = \langle\tilde{\boldsymbol{q}}\rangle + \boldsymbol{q} \,. \tag{22.104}$$

The conditional average of $\tilde{\boldsymbol{q}}$ given that a set of events $\boldsymbol{E} = \{E_1, \ldots, E_M\}$ occurs is denoted by $\langle\tilde{\boldsymbol{q}}|\boldsymbol{E}\rangle$. The conditional average of the total is equal to the unconditional average plus the conditional average of the fluctuation,

$$\langle\tilde{\boldsymbol{q}}|\boldsymbol{E}\rangle = \langle\tilde{\boldsymbol{q}}\rangle + \langle\boldsymbol{q}|\boldsymbol{E}\rangle \,. \tag{22.105}$$

Hereafter, we shall deal mostly with fluctuations, bearing in mind that the mean component can always be incorporated.

Suppose that $\tilde{\boldsymbol{q}}$ and $\boldsymbol{E}$ are random functions over time. The unconditional time average of $\tilde{\boldsymbol{q}}$ would be found by integrating over its values at all times and dividing by the total time. (Ideally, this would be done in the limit of the total time approaching infinity, but in practice the total time is merely large.) The conditional average for a given $\boldsymbol{E}$ can be found by summing over all points in time at which the event $\boldsymbol{E}$ occurs, and dividing by the fraction of the total time for which $\boldsymbol{E}$ occurs. That is, we would restrict attention to just the set of times for which $\boldsymbol{E}$ occurs. To illustrate this further, suppose that $\tilde{\boldsymbol{q}}$ is the heat flux at a point on a surface and E_1 is the event $\{w(\boldsymbol{x}, t) \geq 0\}$, where w is the vertical velocity at a location $\boldsymbol{x}$ above the surface. The conditional average would be found by sampling the heat flux whenever the vertical velocity is positive. To normalize the average of these samples properly, the averaging time would have to be the fraction of the total time during which the vertical velocity is positive.

As another example, suppose that $\tilde{\boldsymbol{q}}$ is the weight of an individual, $E_1 = h$ is the individual's height, and the averaging brackets represent an ensemble average over a large population of individuals. Then, the conditionally averaged weight given the height would be found first by selecting all of the individuals having a certain height, then finding the average of that group's weight. If the total population in the ensemble were N, and if a group equal to 10% of N had a height of (1.8 ± 0.01) m, then the conditional average would be found by summing the heights of all individuals in the group and dividing by $0.1N$. The conditional averaging processes for area averages, line averages, or combinations of any of the various averages are analogous.

By specifying that random events have certain values, conditional averages diminish uncertainty, and by specifying more event information, the uncertainty diminishes further. For example, by specifying the height of an individual, the conditional weight becomes more representative than the average over all individuals. By

specifying the height and age, the group becomes even more specific, and the conditional average becomes even more representative. One expects the variance about the conditional average to continue to diminish as more data are added, but this is only true if the data are correlated with the quantity being averaged. Thus, the conditional weight of an individual is more likely to be representative if the events are genetic or dietary in nature, but not if they are astronomical or otherwise unrelated to a person's weight.

In the context of fluid mechanics, one way we use conditional averages is to improve measurements in the presence of uncontrolled random variations. For example, suppose that laminar flow moves over a surface whose position with respect to a fixed sensor is slowly changing. Let the distance from the surface to the sensor be $y_s(t)$ and the velocity measured by the sensor be $\tilde{u}$. One could represent the velocity at distance y above the surface by the unconditional average, $\langle\tilde{u}\rangle$, but the measurement would be contaminated by the motion of the surface. By sampling the velocity at the sensor only when $y_s(t) = y$, the conditional average $\langle\tilde{u}|y_s(t) = y\rangle$ could be formed, and it would represent the velocity at y more accurately.

Coherent Structures

A second way we use conditional averages is to evaluate the average behavior of flow fields during certain important events, such as the occurrence of strong Reynolds stresses or strong pressure fluctuations. These averages then tell us something about the state of the flow that creates these strong events. In the study of turbulent shear flows, the best-known conditional averaging method is quadrant analysis. One uses this method to explore the mechanisms by which Reynolds shear stresses $\langle u_1 u_2\rangle$ are created in shear flows such as wall turbulence. (u_1 is streamwise and u_2 is wall-normal.) The flow is classified according to the quadrant in which the instantaneous values (u_1, u_2) fall

$$E_1 = \{u_1 > 0, u_2 > 0\}\,; \quad E_2 = \{u_1 < 0, u_2 > 0\}\,;$$
$$E_3 = \{u_1 < 0, u_2 < 0\}\,; \quad E_4 = \{u_1 > 0, u_2 < 0\}\,. \tag{22.106}$$

By taking conditional averages given these events one can find the mean fraction of the total Reynolds stress associated with each quadrant, the mean velocity in each quadrant, the mean rate of turbulent energy transport associated with each quadrant, etc. Events in the second quadrant are *ejections* that move low-streamwise-momentum fluid away from the wall, and events in the fourth quadrant are called *sweeps*, which transport high-momentum fluid towards the wall. Both types of events contribute to a negative value of $\langle u_1 u_2\rangle$, so knowing the conditional average values of other flow properties during these events is useful.

Associating the occurrence of a conditional event with a physical structure in the flow is a more-challenging problem. This problem arises when one wishes to determine the physical form of *coherent structures*. These structures are characteristic, three-dimensional, vortical motions that occur repeatedly and contribute substantially to the mean behavior of the flow. They are random, but not so random as to make them unrecognizable – they are the order within the chaos. Coherent structures are often large scale, but they need not be. Examples of large-scale structures are the spanwise roll vortices that occur in turbulent shear layers. Within the rolls smaller coherent structures occur in the form of *braids* that have smaller vortex cores and a significant component of vorticity in the direction of the mean flow. In turbulent boundary layers the *bulges* are large-scale coherent structures, and the near-wall *quasi-streamwise vortices* are small scale. Even isotropic turbulence, which is the least structured of all turbulent flows, contains small coherent structures in the form of *worms* – slender vortices whose diameters are of the order of 10 Kolmogorov lengths.

Coherent structures are important because they provide a conceptual means of reducing the complexity of turbulence to manageable units. To implement the concept one would like to be able to decompose a flow field into its various coherent structural elements so as to study their various forms, functions, and interactions. To do so, one must have a mathematically unambiguous definition by which the coherent structures can be recognized and isolated. Unfortunately, there is no such definition. The properties of coherent structures listed above may be common to coherent structures, but they do not constitute a complete definition. For example, the quadrant events in (22.106) cannot be associated with a single coherent structure because many different coherent structures could contain regions whose velocity vectors fall in a given quadrant. Sometimes, it is mistakenly asserted that coherent structures are defined by their coherence in space. However, the continuity of fluid motion virtually guarantees that *any continuous fluid motion is spatially coherent*, so spatial coherence can only be one aspect of coherent structures, not a defining property.

It is more useful to define coherent structures as *motions that have a spatial pattern that persists in time*,

as measured by temporal coherence functions having long time scales. Long temporal coherence implies that the patterns would be characteristic because they would contribute significantly to the mean statistics of the flow by virtue of dominating long segments of the time averages. Unfortunately, a definition based on temporal coherence would require analysis of the flow patterns in space and time, and this is too difficult for current experimental methods, and too data-intensive for current computational simulations.

For the time being, one is forced to return to the idea of defining coherent structures by conditional averages using intelligently selected events that recognize the coherent structure. This was the basic idea of quadrant analysis. Quadrant 2 events were associated with ejections of low-momentum fluid upwards, and quadrant 1 events were associated with sweeps of high-momentum fluid towards the wall. If these statements are taken to be the definitions of ejection and sweep, then there is no ambiguity. But, to go further and attribute detailed structural behavior to the occurrence of such events, one needs much more evidence. For example, quadrant 2 ejections need not coincide with the turbulent burst phenomenon, which is defined in terms of a rapid eruption of dye in flow visualizations of near-wall low-speed streaks. Eddies of many different forms could possess regions in which the velocity vector falls into one quadrant or another, without qualifying as bursts or sweeps. The root cause of this ambiguity is that there are many possible conditional events, and no guarantees that any of them unambiguously identifies coherent structure of a particular type.

Conditional Eddies

One approach to resolving the conundrum outlined above is to employ conditional averages, but to refrain from attempting identification using ad hoc events. Instead, one concentrates on events that occur naturally

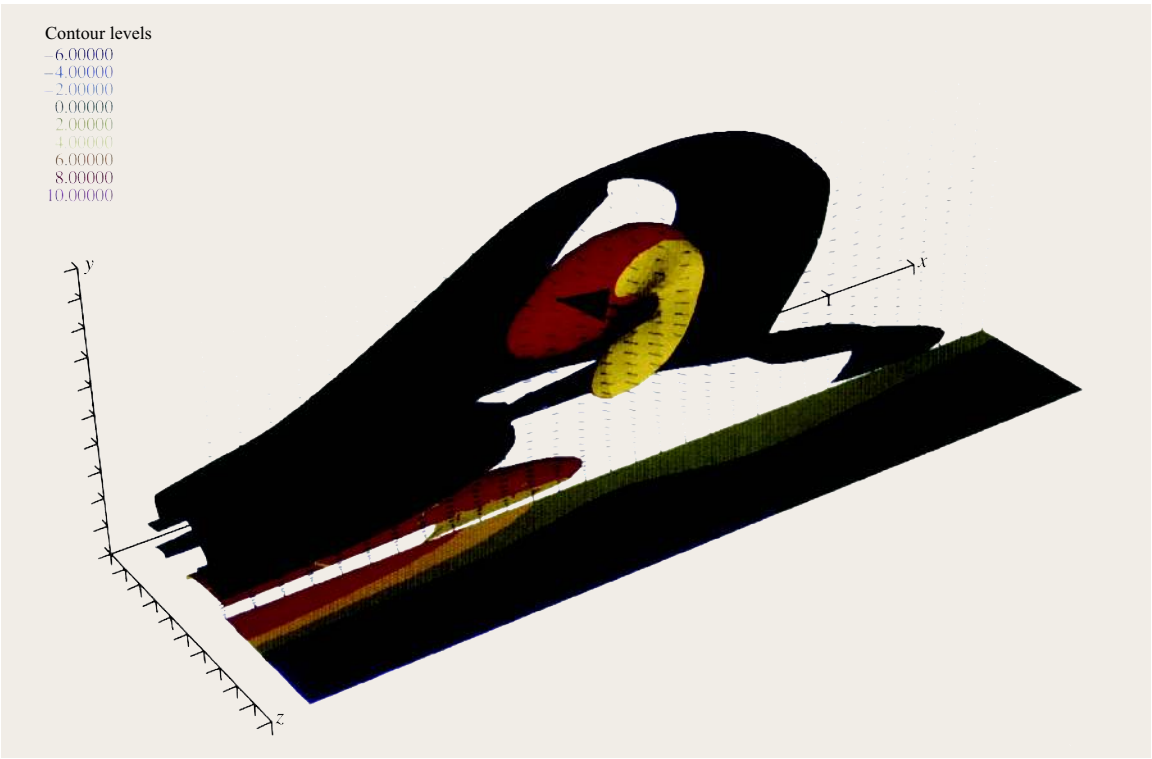

Fig. 22.20 Conditional eddy $\langle \boldsymbol{u}(\boldsymbol{x},t)|\boldsymbol{u}(\boldsymbol{x}_1,t)\rangle$ in turbulent channel flow given a second quadrant event vector. The colored surfaces are contours of constant magnitude of the vorticity of the conditional eddy $\nabla\times\langle \boldsymbol{u}(\boldsymbol{x},t)|\boldsymbol{u}(\boldsymbol{x}_1,t)\rangle = \langle\nabla\times\boldsymbol{u}(\boldsymbol{x},t)|\boldsymbol{u}(\boldsymbol{x}_1,t)\rangle$. The event vector is located $y_1 = 49$ viscous wall units above the lower wall of the $\mathrm{Re}_\tau = 180$ channel flow. The carpet map on the wall depicts the wall shear stress associated with the conditional eddy. The conditional average is found by an approximation that will be discussed later

in the fundamental equations governing the statistics of turbulent flow [22.82]. These equations depend on the particular form of statistical theory one is interested in, but for a broad class of theories it can be shown that the equations governing the probability density function for an event $\boldsymbol{E}$ naturally involve conditional averages of the form $\langle \boldsymbol{u}(\boldsymbol{x}, t)|\boldsymbol{E}\rangle$. From the probability density function equation one can derive equations for any statistical moment of $\boldsymbol{E}$, so understanding velocity fields defined by $\langle \boldsymbol{u}(\boldsymbol{x}, t)|\boldsymbol{E}\rangle$ is fundamental to understanding the closure problem for the $\boldsymbol{E}$-theory.

The quantity $\langle \boldsymbol{u}(\boldsymbol{x}, t)|\boldsymbol{E}\rangle$ defines a velocity vector field that we refer to as the *conditional eddy*. An important class of conditional eddies is the set defined by events of the form

$$\begin{aligned}\boldsymbol{E}_N = \{&\boldsymbol{c}_1 \le \boldsymbol{u}(\boldsymbol{x}_1, t) < \boldsymbol{c}_1 + d\boldsymbol{c}_1\\ &\text{and } \boldsymbol{c}_2 \le \boldsymbol{u}(\boldsymbol{x}_2, t) < \boldsymbol{c}_2 + d\boldsymbol{c}_2 \text{ and } \ldots\\ &\text{and } \boldsymbol{c}_N \le \boldsymbol{u}(\boldsymbol{x}_N, t) < \boldsymbol{c}_N + d\boldsymbol{c}_N\}\,. \end{aligned} \tag{22.107}$$

This event occurs in the Lundgren–Monin equation for the probability density function (PDF) of the velocities at N points. The simplest equation in the Lundgren–Monin hierarchy is the one-point PDF from which equations for all one-point moments (mean, root mean square, and higher-order moments) are derivable. This equation involves the simplest conditional eddy

$$\langle \boldsymbol{u}(\boldsymbol{x}, t)|\boldsymbol{c}_1 \le \boldsymbol{u}(\boldsymbol{x}_1, t) < \boldsymbol{c}_1 + d\boldsymbol{c}_1\rangle\,.$$

Note that quadrant analysis is a special case of this conditional eddy, found by averaging the event velocity vector over each of the quadrants in the (u_1, u_2) plane and all values of u_3. This conditional eddy is quite powerful as a means of recognizing structure. In isotropic turbulence, it takes the form of a vortex ring centered on the event vector [22.83]. In wall turbulence, if the event vector is given values corresponding to the most probable second-quadrant ejection event, the conditional eddy takes the form of the hairpin vortex, shown in Fig. 22.20. This velocity pattern corresponds quite well with patterns observed in experimental flows.

Another type of conditional eddy is the *conditional eddy given local kinematics*. The event defining this eddy consists of the velocity at $\boldsymbol{x}_1$ and the velocity gradient tensor $\nabla\boldsymbol{u}$ at $\boldsymbol{x}_1$, which completely specifies the kinematics at that point. In particular, from the velocity gradient tensor, one can specify the vorticity. In isotropic turbulence, the conditional eddy found by specifying the vorticity looks like a slender vortex whose diameter is of the order of the Taylor microscale and whose length is of the order of the integral length scale, corresponding in shape and dimensions to a turbulent worm. In homogeneous turbulent shear flow the conditional eddy given the vorticity resembles a hairpin vortex [22.84].

22.5.2 Stochastic Estimation

In general, the analysis of data by the process of *stochastic estimation* refers to the approximation of one or more random variables in terms of available data, which may also be random. We shall see that it is intimately related to conditional averaging, and that it will ultimately provide a powerful practical tool for determining conditional eddies from data produced by physical and numerical simulation experiments. To clarify the differences between conditional averaging and stochastic estimation the development of stochastic estimation concepts in this section will begin with a fresh problem statement.

Estimation of Random Processes

In the context of structure in flows that are turbulent or otherwise random, the estimated variable is typically the velocity vector field, which we decompose into the sum of its mean $\boldsymbol{U}(\boldsymbol{x}, t)$ and its fluctuating part $\boldsymbol{u}(\boldsymbol{x}, t)$. As in our discussion of conditional averaging, suppose that the data are associated with the occurrence of certain events at one or more points in the field. Their totality is referred to as the *event data vector* $\boldsymbol{E}$. We shall denote the estimate of $\boldsymbol{u}(\boldsymbol{x}, t)$ in terms of the event data by $\hat{\boldsymbol{u}} = \boldsymbol{F}(\boldsymbol{E}, \boldsymbol{x}, t)$.

The data can take many forms, but in the simplest case $\boldsymbol{E}$ is one or more components of the velocity vector at a single point in the flow, $u_1 = \boldsymbol{u}(\boldsymbol{x}, t)$. Then the estimate would represent a best representation of the velocity field that occurs around the point $\boldsymbol{x}_1$ when the velocity at $\boldsymbol{x}_1$ is equal to the value specified for $\boldsymbol{u}_1$. Note that this value can be varied to explore different states of the flow. Note also that the estimate of the *total* velocity field is just the mean velocity plus the estimate of the *fluctuating* velocity field.

It can be proven that, in general, the least mean-square error estimate of $\boldsymbol{u}(\boldsymbol{x}, t)$ given the data $\boldsymbol{E}$ is the conditional average of $\boldsymbol{u}(\boldsymbol{x}, t)$ given $\boldsymbol{E}$, denoted by $\langle \boldsymbol{u}(\boldsymbol{x}, t)|\boldsymbol{E}\rangle$. That is, of all possible estimates in terms of the event data, $\boldsymbol{F}(\boldsymbol{E}, \boldsymbol{x}, t)$, the mean-square error $e = \langle|\boldsymbol{u} - \boldsymbol{F}|^2\rangle$ is a minimum when $\boldsymbol{F} = \langle \boldsymbol{u}|\boldsymbol{E}\rangle$.

This result is so important that it is derived here in detail. The condition for the error to be a minimum is that the first variation $\delta e = 0$. Taking the variation δF_i

with respect to all possible functions of the event data gives

$$\delta e = \langle 2(u_i - F_i)(-\delta F_i)\rangle \tag{22.108a}$$

$$= -2\langle\langle(u_i - F_i)|\boldsymbol{E}\rangle\delta F_i\rangle\ . \tag{22.108b}$$

Equation (22.108b) follows from (22.108a) by writing the average as the average over the random event data $\boldsymbol{E}$ of the conditional average given $\boldsymbol{E}$. Since $\boldsymbol{E}$ is fixed inside the conditional average, $\delta F_i(\boldsymbol{E})$ is also fixed, and it can be taken outside of the conditional average. [The conditional average given $\boldsymbol{E}$ averages over fluctuations in $\boldsymbol{u}$, while the unconditional (outer) average averages over fluctuations in $\boldsymbol{E}$.] In order for (22.108b) to vanish for arbitrary variations δF_i, the conditional average must vanish identically, leading to

$$F_i = \langle u_i|\boldsymbol{E}\rangle \tag{22.109}$$

or

$$\hat{\boldsymbol{u}} = \text{ best estimate of } \boldsymbol{u} \text{ given the data } \boldsymbol{E} = \langle \boldsymbol{u}|\boldsymbol{E}\rangle\ . \tag{22.110}$$

This simple but elegant result is quite general. We could replace the velocity field $\boldsymbol{u}$ with *any* quantity $\boldsymbol{q}$ and arrive at the same result.

An estimate of $\boldsymbol{u}$ in terms of event data $\boldsymbol{E}$ must become increasingly erroneous as the location $\boldsymbol{x}$ is moved away from the locations of the event data, because $\boldsymbol{u}$ will become uncorrelated with the event data for large spatial (or temporal) separations. The conditional average $\langle \boldsymbol{u}(\boldsymbol{x}, t)|\boldsymbol{E}\rangle$ manifests this property by reducing to the unconditional average $\langle \boldsymbol{u}\rangle$ (which equals zero if $\boldsymbol{u}$ is a fluctuation) as $\boldsymbol{x}$ is removed from the vicinity of the event data.

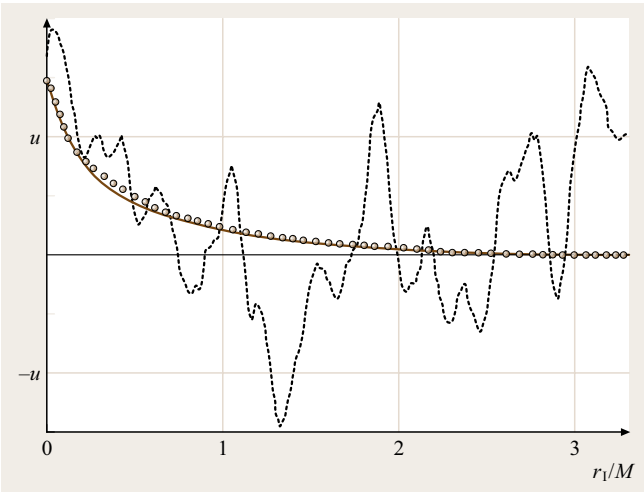

Fig. 22.21 Comparison of a random realization of the streamwise velocity $u(x')$ measured in grid turbulence (*dashed line*), the conditional average of the velocity given the value at $x' = x$ (*solid line*), and the linear stochastic estimate (*open circles*)

Linear and Nonlinear Mean-Square Estimation

In general, $\langle \boldsymbol{u}|\boldsymbol{E}\rangle$ is a nonlinear function of the components of $\boldsymbol{E}$. However,, under the condition that the components of $\boldsymbol{u}$ and $\boldsymbol{E}$ are joint normally distributed, it is well known that $\langle \boldsymbol{u}|\boldsymbol{E}\rangle$ is a linear function of $\boldsymbol{E}$ [22.85]. Often, this property is applied approximately to non-normal random variables by postulating an estimate of $\boldsymbol{u}$ in the form of a linear combination of the event data. Then one speaks of *linear mean-square estimation*. This subject is discussed thoroughly in the literature of stochastic theory [22.85, 86]. Let

$$\hat{\hat{u}}_i = \text{ linear estimate of } u_i = \sum_{j=1}^{M} L_{ij} E_j\ . \tag{22.111}$$

The mean-square error of this estimate is

$$\left\langle \left(u_i - \sum_{j=1}^{M} L_{ij} E_j \right)^2 \right\rangle = \min\ ,$$

$$i = 1, 2, 3 \text{ and } j = 1, \ldots, M\ . \tag{22.112}$$

The mean-square error of the linear estimate must be greater than or equal to the error of the conditional average. The necessary condition for minimization of the mean-square error is the *orthogonality principle* which states that the errors $u_i - \sum_{j=1}^{M} L_{ij} E_j$ are statistically orthogonal to the data

$$\left\langle \left(u_i - \sum_{j=1}^{M} L_{ij} E_j \right) E_k \right\rangle = 0\ ,$$

$$i = 1, 2, 3 \text{ and } j, k = 1, \ldots, M\ . \tag{22.113}$$

Equation (22.113) follows from (22.112) by setting the derivative with respect to L_{ik} of the mean-square error equal to zero. Simple manipulation of (22.113) leads to an $M \times M$ system of linear algebraic equations for the coefficients for each value of i

$$\sum_{j=1}^{M} \langle E_j E_k\rangle L_{ij} = \langle E_k u_i\rangle\ ,$$

$$j, k = 1, \ldots, M\ , \quad i = 1, 2, 3\ . \tag{22.114}$$

The coefficients in these equations are the correlations between each pair of event data and between each event datum and the quantity being estimated.

Figure 22.21 illustrates the behavior of the conditional average and the linear estimate. In this example, the quantity being estimated is the streamwise velocity component in an experimental grid turbulence flow field. The event is that the velocity component is equal to $1.5\sigma_1$ at $x' = x$, where σ_1 is the root mean square of u. A single realization of $u(x')$ that satisfies this event is plotted as a dashed line, and the conditional average and the linear estimate are shown as a solid line and round symbols, respectively. At $x' = x$ the realization and the estimates each equal the given event. As $x' - x$ increases, the conditional average and the linear estimate decay to zero because they lose correlation with the event. The conditional average must approach the unconditional average, which vanishes, and the linear estimate follows suit. As they vanish, the root-mean-square error increases with increasing x' until it asymptotes to the unconditional *root-mean-square value* σ_1.

This illustrates the general rule that estimation of a random variable does not significantly reduce the error unless the variable being estimated is highly correlated with the data, e.g., in the vicinity of the data and correlated with it. Providing information about data that have little physical relationship to the process will not reduce the error, nor will providing physically relevant data that are too far removed from the point of estimation in space or time.

Estimation of Conditional Averages

In addition to estimating $\boldsymbol{u}$ as a function of $\boldsymbol{E}$, one can also *estimate the conditional average* $\langle \boldsymbol{u}|\boldsymbol{E}\rangle$. The conditional average is a deterministic function of random data $\boldsymbol{E}$, so it toe is a random variable. It is natural to expand $\langle \boldsymbol{u}|\boldsymbol{E}\rangle$ in a Taylor series about $\boldsymbol{E} = 0$, and truncate at some order [22.82, 83]. When the series contains only first-order terms, we refer to this as a *linear stochastic estimation* (LSE) to distinguish it from linear mean-square estimation. The equations for *linear* stochastic estimation of the i-th component of $\langle \boldsymbol{u}|\boldsymbol{E}\rangle$ are

$$\breve{u}_i = \text{ linear stochastic estimate of } \langle u_i|\boldsymbol{E}\rangle = \sum_{j=1}^{M} \breve{L}_{ij} E_j \,, \qquad (22.115)$$

where M is the number of event data, and $\breve{L}_{ij}$ is a function of $\boldsymbol{x}$ and the positions of the event data. The estimation coefficients $\breve{L}_{ij}$ are chosen so that the mean-square error

$$\left\langle \left(\langle u_i|\boldsymbol{E}\rangle - \sum_{j=1}^{M} \breve{L}_{ij} E_j \right)^2 \right\rangle = \min \,,$$
$$i = 1, 2, 3 \text{ and } j = 1, \ldots, M \,. \qquad (22.116)$$

As above, the necessary condition for minimization is the *orthogonality principle*, which states that the errors $\langle u_i|\boldsymbol{E}\rangle - \sum_{j=1}^{M} \breve{L}_{ij} E_j$ are statistically orthogonal to the data

$$\left\langle \left(\langle u_i|\boldsymbol{E}\rangle - \sum_{j=1}^{M} \breve{L}_{ij} E_j \right) E_k \right\rangle = 0 \,,$$
$$i = 1, 2, 3 \text{ and } j, k = 1, \ldots, M \,. \qquad (22.117)$$

The resulting equations for $\breve{L}_{ij}$,

$$\sum_{j=1}^{M} \langle E_j E_k \rangle \breve{L}_{ij} = \langle E_k u_i \rangle \,,$$
$$j, k = 1, \ldots, M \,, \quad i = 1, 2, 3 \,, \qquad (22.118)$$

are identical to those for L_{ij} in (22.114). Thus, *the linear stochastic estimate of* $\langle \boldsymbol{u}|\boldsymbol{E}\rangle$ *and the linear mean-square estimate of* $\boldsymbol{u}$ *are numerically equal*. The principal difference is one of interpretation. In particular, while the mean-square error of the linear mean-square estimate of $\boldsymbol{u}$ must be large when $\boldsymbol{u}$ is uncorrelated with $\boldsymbol{E}$, (due, for

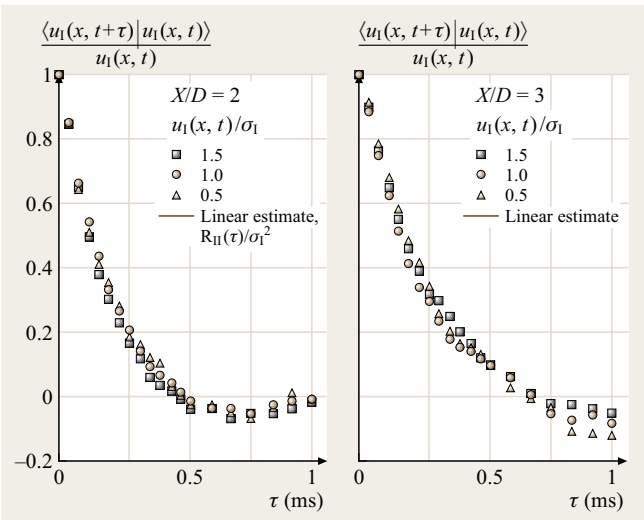

Fig. 22.22 Comparison of conditionally averaged streamwise velocity on the centerline of the shear layer in a round turbulent jet with the linear stochastic estimate of the conditional average. (After *Adrian* et al. [22.87])

example, to a large separation between $\boldsymbol{x}$ and the location of the event data), the error of the linear stochastic estimate of $\langle \boldsymbol{u}|\boldsymbol{E}\rangle$ may be small because $\langle \boldsymbol{u}|\boldsymbol{E}\rangle$ also vanishes as the separation becomes large. The results in Fig. 22.21 illustrate this behavior clearly if we consider the linear estimate to be an estimate of the conditional average.

The linear estimate of the conditional average is surprisingly good for a variety of different types of turbulent flows, including isotropic turbulence, pipe flow, and jet flow [22.88], and for a variety of different types of variables, including velocity, pressure and Reynolds stresses [22.87]. As an example, conditional averages of the streamwise velocity at $t+\tau$ in a turbulent jet given the value of the velocity at t are compared to the linear stochastic estimate in Fig. 22.22. For this simple case the reader can verify that the linear estimate is

$$\begin{aligned}\breve{u}_1(\tau) &= \text{lin. est.}\langle u_1(t+\tau)|u_1(t)\rangle \\ &= \frac{\langle u_1(t)u_1(t+\tau)\rangle}{\langle u_1^2(t)\rangle}u_1(t)\,. \end{aligned} \tag{22.119}$$

The averages are conditioned on three different values of the velocity at zero time and the linear estimate is calculated from the time-delayed autocorrelation.

Usually, the accuracy of linear estimation is good, even for large values of the event data. In situations where the linear estimate falls short of the accuracy required, the estimation can be improved by postulating $\boldsymbol{F}(\boldsymbol{E})$ to be a nonlinear function such as a quadratic or a higher-order polynomial. Often, higher-order terms have little effect on probable values of the events, but sometimes they improve accuracy [22.89–91]. Interestingly, *Brereton* [22.92] has also suggested a Laurent-type expansion that contains negative powers of the event data and showed improved estimation for low-amplitude events. Ultimately, the accuracy of an estimate must rest in direct comparison of the estimate with the conditional average.

It was noted earlier that the most basic conditional eddy in the hierarchy of conditional averages in the PDF equations is $\langle \boldsymbol{u}(\boldsymbol{x},t)|\boldsymbol{u}(\boldsymbol{x}_1,t)\rangle$. The field shown in Fig. 22.20 was presented as an approximation to a conditional eddy of this type. It can now be explained that the approximation was found by the stochastic estimate

$$\text{lin. est.}\langle u_i|\boldsymbol{u}_1\rangle = \breve{L}_{ij}u_{1j}, \quad i,j=1,2,3 \tag{22.120}$$

in which $\breve{L}_{ij}$ is found by solving

$$\langle u_{1j}u_{1k}\rangle \breve{L}_{ij}(\boldsymbol{x}_1,\boldsymbol{x}) = R_{ik}(\boldsymbol{x}_1,\boldsymbol{x})\,, \quad i,j,k=1,2,3\,, \tag{22.121}$$

where

$$R_{ik}(\boldsymbol{x}_1,\boldsymbol{x}) = \langle u_i(\boldsymbol{x}_1,t)u_k(\boldsymbol{x},t)\rangle \tag{22.122}$$

is the two-point spatial correlation with a fixed reference point $\boldsymbol{x}_1$. In matrix form

$$\begin{pmatrix} \langle u_{11}u_{11}\rangle & \langle u_{11}u_{12}\rangle & \langle u_{11}u_{13}\rangle \\ \langle u_{12}u_{11}\rangle & \langle u_{12}u_{12}\rangle & \langle u_{12}u_{13}\rangle \\ \langle u_{13}u_{11}\rangle & \langle u_{13}u_{12}\rangle & \langle u_{13}u_{13}\rangle \end{pmatrix} \begin{pmatrix} \breve{L}_{i1} \\ \breve{L}_{i2} \\ \breve{L}_{i3} \end{pmatrix} = \begin{pmatrix} R_{i1}(\boldsymbol{x}_1,\boldsymbol{x}) & R_{i2}(\boldsymbol{x}_1,\boldsymbol{x}) & R_{i3}(\boldsymbol{x}_1,\boldsymbol{x}) \end{pmatrix} \tag{22.123}$$

A common and useful procedure is to use event data consisting of velocity vectors $\boldsymbol{u}_\alpha = \boldsymbol{u}_\alpha(\boldsymbol{x}_\alpha,t)$ at a set of N space points $\{\boldsymbol{x}_\alpha\}$, $\alpha=1,\ldots,N$. Then, $\boldsymbol{E}$ contains $M=3N$ data,

$$\boldsymbol{E} = \{u_{11},u_{12},u_{13},u_{21},\ldots,u_{N1},u_{N2},u_{N3}\}\,, \tag{22.124}$$

and $\langle E_jE_k\rangle$ involves only second-order two-point spatial correlations.

$$\begin{aligned} &R_{jk}(\boldsymbol{x}_\alpha,\boldsymbol{x}_\beta) \equiv \langle u_j(\boldsymbol{x}_\alpha,t)u_k(\boldsymbol{x}_\beta,t)\rangle\,, \\ &\alpha,\beta=1,\ldots,N\,. \end{aligned} \tag{22.125}$$

The correlation on the right-hand side of (22.118) involves correlations of the form

$$\begin{aligned} &\langle E_ku_i\rangle = \langle u_l(\boldsymbol{x}_\alpha,t)u_i(\boldsymbol{x},t)\rangle = R_{li}(\boldsymbol{x}_\alpha,\boldsymbol{x})\,, \\ &k=1,\ldots,M\,; \quad i,l=1,2,3\,. \end{aligned} \tag{22.126}$$

Thus, when the event data consist of velocity vectors, knowledge of the two-point spatial correlations of the velocity suffices to determine the linear estimate.

Given the estimate of a conditional eddy velocity field, the estimate of a derivative of the conditional eddy can be found by differentiating the estimate with respect to $\boldsymbol{x}$. We have seen this already for the vorticity field in Fig. 22.20. A more-complex application that also illustrates the use of multipoint velocity data is shown in Fig. 22.23. The data consist of a grid of velocity vectors lying in a plane located above a wall in channel flow. The linearly estimated velocity field, given these data, is differentiated at the wall to get the viscous wall shear stress, shown in color contours. Comparison with the actual viscous wall shear stress shows close agreement, although the estimate is smoothed somewhat with respect to the actual stress field.

If the event vector contains derivatives of the velocity field, $(\partial u_i/\partial \boldsymbol{x}_j)$ at the points $\boldsymbol{x}_\alpha$ the resulting two-point correlations that appear in (22.122) contain correlations between velocities and derivatives, and derivatives and

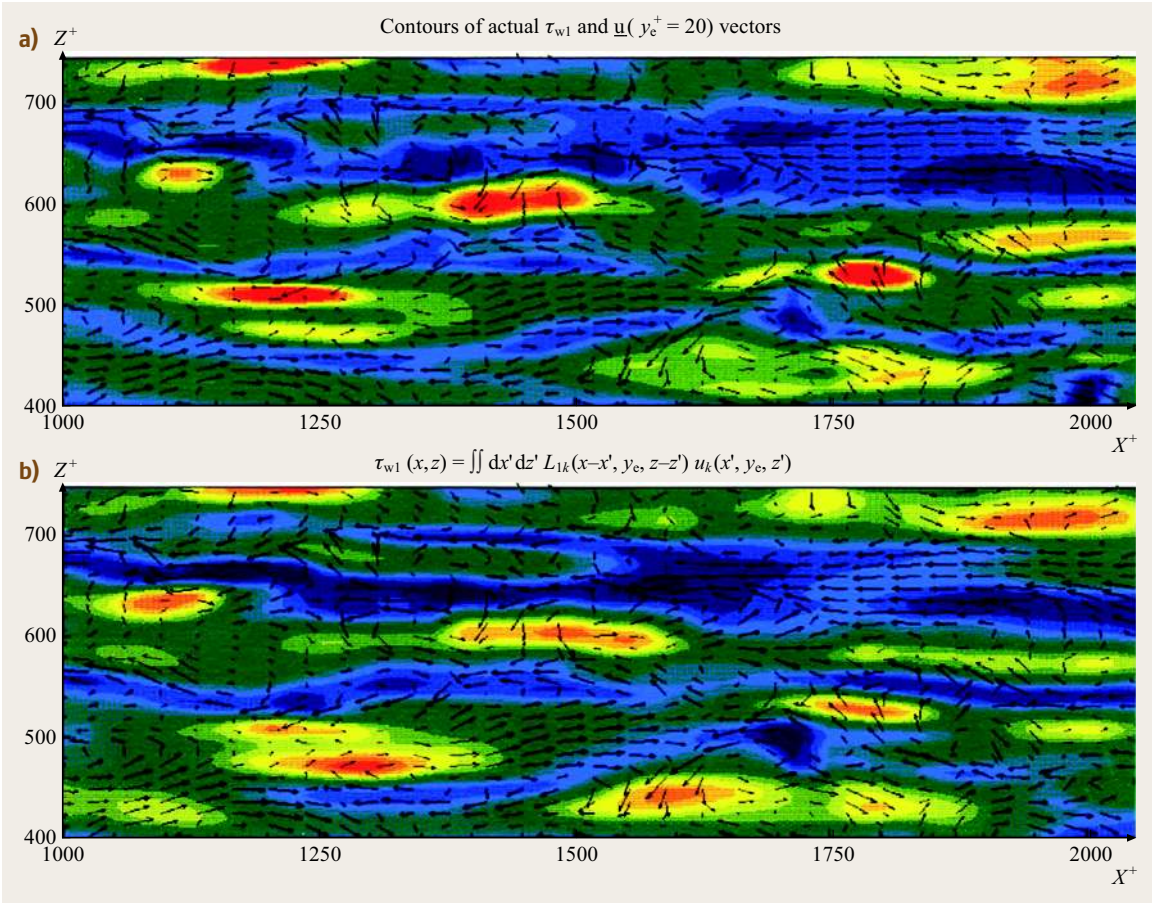

Fig. 22.23 **(a)** Instantaneous streamwise wall shear stress and velocity vectors on a plane $y+ = 20$ viscous wall units above the wall in direct numerical simulation of turbulent channel flow. **(b)** Linear estimate of the conditional average of the wall shear stress given the same set of velocity vectors on the $y+ = 20$ plane. (After *Bagwell* et al. [22.93])

derivatives. Since each type of correlation can be expressed in terms of R_{ij} and its derivatives, it follows that knowledge of the two-point spatial correlation function again suffices to determine fully the linear estimate of $\boldsymbol{u}$ in terms of velocity data and derivatives of any order. This is a powerful result, as it states that very complicated conditional averages can be approximated once R_{ij} is known.

Conditional averages play three important roles. First, they are used in the study of coherent flow structures in turbulence. Second, they appear naturally in PDF theories. These theories define conditional eddies in the form $\langle \boldsymbol{u}(\boldsymbol{x}, t)|\boldsymbol{E}\rangle$, where $\boldsymbol{E}$ consists of a set of velocities at N points. Third, conditional averages play a fundamental role in estimation theory by virtue of being the best least mean-square estimate given the available data. Linear and nonlinear stochastic estimation can be used to estimate either the random variable $\boldsymbol{u}$ or its conditional average. Estimation of the random variable produces a mean-square error that increases as the correlation of the variable with the data decreases. However, estimation of the conditional average does not suffer from this problem. Thus, one must be careful to distinguish clearly between estimation of the variable or the conditional average. The linear estimate of a conditional average is exact for joint normal random variables, but this should not be taken to imply that joint normal distribution is a necessary condition for accuracy, or that accuracy implies that the variable must be joint normal. Experimental evidence shows that stochastic estimation works well for non-joint-normal variables.

Stochastic estimation offers two huge advantages over conditional averaging. First, calculating the conditional average requires finding realizations of the variable and the data in which the data assume the prescribed values of interest. When the event vector has high dimension, the occurrence of the event is highly improbable, and one must take immense amounts of data to build up a stable conditional average. For example, if an N-point conditional eddy is to be evaluated for a single set of velocity vector values, one would have to sift through an N-dimensional space of events to find the realizations in which the prescribed values of the events occur. In contrast, the stochastic estimate requires evaluation of the correlations between the data and the variable being estimated, and it is straightforward to calculate such two-point correlations, especially from data produced by direct numerical simulations or particle image velocimetry. Secondly, once the correlations have been found, the stochastic estimate, linear or nonlinear, gives the conditional average for *any* set of event values. Evaluation for new values only requires plugging them into the linear form. In contrast, evaluating the conditional average for a new event vector would require sorting through all of the data to find realizations that satisfied the new event.

The linear estimate of a conditional eddy offers a third attractive feature. Namely, it involves only the two-point second-order spatial correlation tensors. These are fundamental quantities in the statistical description of turbulent structure, but the correlation tensor in not easily interpreted in terms of the underlying eddy structure. The linear estimate repackages the correlation tensor information into a vector field that is much more readily interpreted.

22.6 Wavelet Transforms

22.6.1 Introduction to Wavelets

Conventional data processing is performed in either the time domain (moments, correlations, etc.) or the frequency domain (power spectra, etc.). Wavelet processing combines the two, allowing the definition of local spectral properties and the ability to zoom in on local features of the signal. To simplify notations, we use *time-frequency*, with an implied reference to time series for the data; the alternative use of data is straightforward. Similarly, the *signal* is simple terminology for scalar or vector field.

A wavelet is a basis function (an elementary building block to analyze or synthesize the signal) characterized by

- its shape and its amplitude, to be selected by the user
- its scale (frequency or size) and location (time or location) relative to the signal, spanning a range of interest to study a given phenomenon.

Wavelet coefficients are the scalar products of the signal with all dilated and translated wavelets. The set of wavelet coefficients thus obtained is indexed by position and scale (always positive) in the wavelet half-plane.

We will first present the continuous wavelet transform, then the discrete and orthogonal wavelet transforms. Additional details can be found in standard references [22.94–96]. We will discuss their implementation and how to use them to analyze signals measured in laboratory experiments or generated numerically. We will also explain how the wavelet transform can be used to extract coherent structures form a velocity or vorticity field. An overview of techniques can be found in [22.97] and in the archival literature.

22.6.2 Continuous Wavelet Transform

Definition of a Wavelet

Let us assume that a wavelet $\psi(t)$ is given.

Notations: Fourier Transform. For reference and to establish notation, we define the Fourier transform of $\psi(t)$ as

$$\hat{\psi}(\omega) = \int_{-\infty}^{\infty} \psi(t)\, \mathrm{e}^{-2\mathrm{i}\pi\omega t}\, \mathrm{d}t \,,$$

with its inverse

$$\psi(t) = \int_{-\infty}^{\infty} \hat{\psi}(\omega)\, \mathrm{e}^{2\mathrm{i}\pi\omega t}\, \mathrm{d}\omega \,.$$

The energy spectrum is defined on the basis of the Parseval relation

$$\frac{1}{2} \int_{-\infty}^{\infty} |\, \psi(t)\, |^2 \, \mathrm{d}t = \int_{-\infty}^{\infty} E_{\mathrm{F}}(\omega)\, \mathrm{d}\omega \,.$$

The subscript 'F' refers to Fourier, to distinguish it from wavelet spectra; in the applications, we will also use the compensated spectrum $\omega \cdot E$ to display dominant scales.

Regardless of its scale and magnitude, a function ψ is admissible as a wavelet if and only if

$$c_\psi = \int_0^\infty |\hat{\psi}(\omega)|^2 \frac{\mathrm{d}\omega}{|\omega|} < \infty \,, \tag{22.127}$$

for which it is sufficient that its mean vanishes

$$\int_{-\infty}^{\infty} \psi(t)\,\mathrm{d}t = 0 \,. \tag{22.128}$$

Optionally, higher moments $\int t^n \psi(t)\,\mathrm{d}t$ may also vanish. In addition, it is required that ψ asymptote to zero fast enough for large t

$$|\psi(t)| < \frac{C}{1+|t|^p} \tag{22.129}$$

with $C > 0$ and $p \in \mathbb{N}$. Other desirable properties include good localization (steep decay) in both the time and frequency domains. These conditions are not very restrictive, and many different wavelets have been used in the literature; only a few examples (and reasons for their selection) can be treated here, but the rationale for wavelet selection can be inferred from the applications discussed in Sect. 22.6.4.

Concerning the Choice of Wavelet. Some of the trade-offs implied by the choice of wavelet are apparent from a few examples. A difference of two Dirac functions separated by a time τ, used to build structure functions, has an extended Fourier spectrum. The Haar function also has compact support (Fig. 22.24) (compact support means that the subset of the time domain over which the function is nonzero is closed and bounded), and an extended oscillatory spectrum ($1/\omega^2$ decay) (Fig. 22.25) as a consequence. The Mexican-hat and Morlet wavelets (formulae in next section) have an exponential drop-off in both time and frequency, and are preferred in many cases. The trade-off between them is that the Morlet wavelet has narrow spectral bandwidth and an extended time domain, while the Mexican-hat wavelet is more localized in the time domain at the expense of a wider spectral content. Perfect localization in both time and frequency is impossible (due to the Heisenberg uncertainty principle): each wavelet represents a compromise, the pros and cons of which should be reflected in the interpretation of the results.

General Formulae

The continuous wavelet transform of a function $u(t)$ (assumed to have zero mean and finite energy) is defined as a convolution

$$\tilde{u}(a,t) = \int_{-\infty}^{\infty} \left[u(t') \frac{1}{\sqrt{a}} \psi^* \left(\frac{t-t'}{a} \right) \right] \mathrm{d}t' \,, \tag{22.130}$$

where the asterisk superscript denotes complex conjugation; $\tilde{u}(a,t)$ is the wavelet coefficient at time t and scale a. The integral measures the comparison of the local shape of the signal and the shape of the wavelet. The dilation factor a acts as a zoom, so large features of the original signal appear at large values of a, while short-duration events appear at small a. By centering the scaled

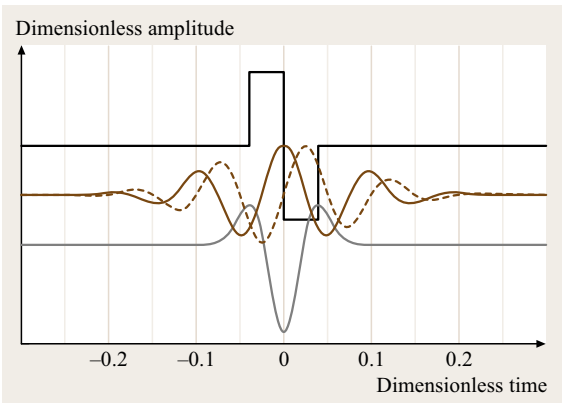

Fig. 22.24 Three wavelets of similar scale (with arbitrary vertical offsets). From top to bottom: Haar, Morlet (real (*solid*) and imaginary (*dashed*) parts), and Mexican hat

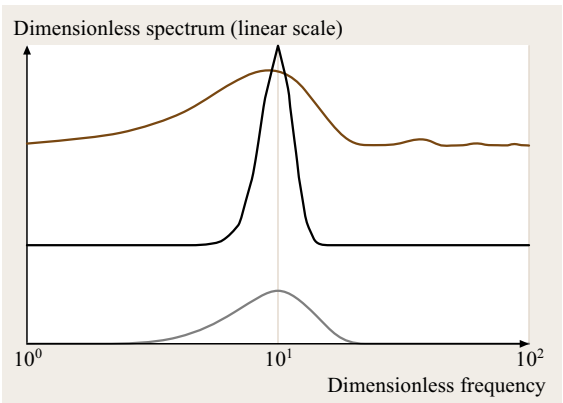

Fig. 22.25 The Fourier spectra $E_\mathrm{F}(\omega)$ of the three wavelets of Fig. 22.24 (arbitrary vertical offsets). From top to bottom: Haar, Morlet, and Mexican hat

wavelet at time t, some time localization around t and some spectral localization around scale a is achieved.

Two interpretations of the variables t and a are consistent with t/a being dimensionless. We can assume that both t and a have dimensions of time; alternatively, t can be nondimensionalized by the wavelet's centroid frequency ω_ψ for $a = 1$,

$$\omega_\psi = \frac{\int_0^\infty \omega|\hat{\psi}(\omega)|\,\mathrm{d}\omega}{\int_0^\infty |\hat{\psi}(\omega)|\,\mathrm{d}\omega}\,.$$

in which case the dilation factor a is also dimensionless. We use them indifferently.

The value of the wavelet transform as an analytical tool rests on the next two formulae. First, the inverse transform

$$u(t) = \frac{1}{c_\psi}\int_{-\infty}^{\infty}\int_0^\infty \left[\tilde{u}(a,t')\frac{1}{\sqrt{a}}\psi\left(\frac{t-t'}{a}\right)\right]\frac{\mathrm{d}a}{a^2}\,\mathrm{d}t' \qquad (22.131)$$

requires a convolution in time as well as integration over a. It expresses the fact that no information is lost in the transform, and that the signal can be interpreted as made of a linear combination of wavelets. Second, there is a Parseval relation

$$\int_{-\infty}^{\infty}[u(t)v^*(t)]\,\mathrm{d}t = \frac{1}{c_\psi}\int_{-\infty}^{\infty}\int_0^\infty \tilde{u}(a,t)\tilde{v}^*(a,t)\frac{\mathrm{d}a}{a^2}\,\mathrm{d}t\,, \qquad (22.132)$$

and in particular

$$\int_{-\infty}^{\infty}|\,u(t)\,|^2\,\mathrm{d}t = \frac{1}{c_\psi}\int_{-\infty}^{\infty}\int_0^\infty |\,\tilde{u}(a,t)\,|^2\,\frac{\mathrm{d}a}{a^2}\,\mathrm{d}t\,, \qquad (22.133)$$

which shows that the energy of the signal is conserved in the time–frequency domain. Thus, the squared wavelet coefficients $\tilde{u}$ provide an instantaneous power spectrum, useful for studying transient or intermittent signals.

The Energy Distribution. For statistically stationary signals, one classically considers the modulus of its Fourier transform [i. e., the spectrogram or energy spectrum $E_F(\omega)$]. Since the phase of the Fourier coefficients is thus lost, no information on the local structure of the signal can be retrieved, as the time or space information is encoded by the phases of all Fourier coefficients. Therefore the classical energy spectrum, based on the Fourier transform, is not ideal to analyze statistically nonstationary or inhomogeneous signals. The wavelet transform extends the concept of energy spectrum so that one can define a local energy spectrum. Several related algorithms are illustrated in Sect. 22.6.4.

Variants. Wavelets can be normalized in such a way as to have unit energy at all scales. This option is favored by many authors, and is associated with the $\sqrt{a}$ and c_ψ factors in the formulae above. Alternatively, changes in variables and different normalizations (as used later) give simpler expressions of inverse transforms and spectra. It is recommended that the user verify the consistency of formulae and software of different provenance by performing wavelet transforms of simple test signals.

Examples: Continuous Wavelet Transforms and Interpretation

In the examples illustrated below, the wavelet transform will be applied to an artificial signal (Fig. 22.26), so that specific experimental conditions need not be described. The signal combines features encountered in various applications in fluid mechanics. We superpose a modulated wave, isolated events in the same frequency range, and continuous and intermittent wave and noise packets (some of the latter correlated to the phase of the primary wave, e.g., at times 2, 7, and 13 of the primary wave).

Implementation: Convolution. Since the wavelet transform at each scale a is a convolution of the signal with the scaled wavelet, the operation is efficiently implemented as a multiplication in Fourier space, i. e.,

$$\tilde{u}(a,t) = \sqrt{a}\int_{\infty}^{\infty}\left[\mathrm{e}^{2\mathrm{i}\pi\omega t}\hat{\psi}^*(a\omega)\hat{u}(\omega)\right]\mathrm{d}\omega\,,$$

which involves the Fourier transform of the signal, multiplication by the (precalculated) transform of the scaled wavelet, and inverse Fourier transform. This relation also shows that the wavelet transform is a band-pass filtered signal, with $\hat{\psi}(a\omega)$ describing the shape of the filter. Each wavelet coefficient combines the information in a temporal vicinity (weighted by the wavelet shape) and in a spectral vicinity (weighted by its Fourier spectrum); it is this time–frequency compromise that makes wavelets so versatile with intermittent data.

Discretization. In practice, the signal $u(t)$ of duration T is sampled at constant intervals on a grid $t_i = iT/N, i \in [0, N-1]$ with $N = 2^J$. This corresponds to a Nyquist frequency $\omega_{\max} = N/2T$, and a spectrum

of discrete decreasing frequencies, for which a logarithmic progression $\omega_j = \omega_{\max} a_0^{-j}$ is typically used. The frequency ratio a_0 is 2 (one per octave) for orthogonal wavelets; for continuous wavelets, a ratio $a_0 = 2^{1/3}$ was used for most figures, with a finer resolution $a_0 = 2^{1/9}$ where required. The lowest Fourier frequency $\omega_0 = 1/T$ does not necessarily apply to the wavelet transform, although it has been adopted in the figures. The Fourier frequencies vary linearly, with $\omega_k = k\omega_0$. For a signal u, the transform is sampled in the wavelet half-plane according to the expression

$$\tilde{u}(a_j, t_i) = \sqrt{a_j} \sum_{k=-N/2}^{N/2} \left[\mathrm{e}^{2\mathrm{i}\pi\omega_k t_i} \hat{\psi}^*(a_j\omega_k)\hat{u}(\omega_k) \right] ,$$

where $a_j = a_0^j$ and $\hat{u}(\omega_k) = \Delta t \sum_{n=0}^{N-1} u(t_n)\mathrm{e}^{-2\pi\mathrm{i}t_n\omega_k}$ and can be efficiently computed using the FFT. Note that frequencies ω_k have been centered around $\omega = 0$ and that $\hat{u}(-\omega) = \hat{u}^*(\omega)$ since u is real-valued.

Discretization Error. Sampling of the continuous wavelet transform at discrete points entails some loss of information. This loss can be treated in practice as an approximation for which errors can be kept as small as desired on a suitably fine grid. Bounds on the errors can be found in the mathematical theory of frames. Generally, using the time-series sampling interval and a frequency ratio of 2–5 per octave yields sufficient accuracy for many applications.

Mexican-Hat Wavelets. Starting from the normalized Gaussian filter

$$F_\sigma(t) = \frac{1}{2\sqrt{\pi\sigma}} \mathrm{e}^{-\frac{t^2}{4\sigma}} , \qquad (22.134)$$

in which $\sigma = a^2/2$, its derivative with respect to σ (second time derivative) gives the Mexican-hat wavelet:

$$\psi_2(\sigma, t) = \frac{\mathrm{d}F_\sigma}{\mathrm{d}\sigma} = \left(\frac{t^2}{4\sigma^2} - \frac{2}{\sigma} \right) F_\sigma(t) = \frac{\mathrm{d}^2 F_\sigma}{\mathrm{d}t^2} . \qquad (22.135)$$

It is a difference of Gaussian filters of different scales (band-pass filtering), divided by the scale difference. Rather than energy normalization, this variant favors the relation to Gaussian filtering and the simple formulae below, including the compatibility equation. The Fourier transform of ψ_2 is

$$\hat{\psi}_2(\sigma, \omega) = -4\pi^2\omega^2 \mathrm{e}^{-4\pi^2\omega^2\sigma} . \qquad (22.136)$$

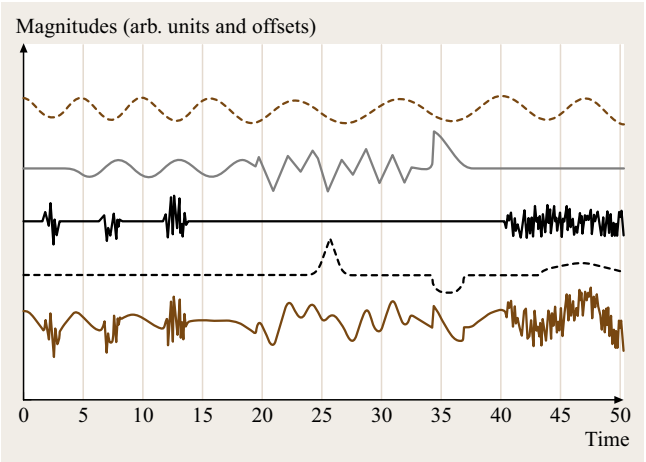

Fig. 22.26 The signal $u(t)$ used in examples (*bottom*), and its various contributions (*top*); arbitrary offsets and magnitude

For a signal u, the Mexican-hat wavelet transform is written

$$\tilde{u}_2(\sigma, t) = \int u(t')\psi_2(t - t', \sigma)\mathrm{d}t' = \frac{\mathrm{d}^2}{\mathrm{d}t^2}(F_\sigma * u) . \qquad (22.137)$$

Then the energy of the signal is given by

$$\int \frac{|\, u \,|^2}{2} \mathrm{d}t = \iint 2 \,|\, \sigma\tilde{u}_2 \,|^2 \frac{\mathrm{d}\sigma}{\sigma} \mathrm{d}t \qquad (22.138)$$

and the inverse transform by either one of the relations

$$u(t) = -\int_0^\infty \sigma\tilde{u}_2(\sigma, t) \left[\frac{\mathrm{d}\sigma}{\sigma} \right] \qquad (22.139)$$

$$= 4 \iint \sigma\tilde{u}_2(\sigma, t')\psi_2(t - t', \sigma)\mathrm{d}\sigma\,\mathrm{d}t' . \qquad (22.140)$$

The relations show that $\sigma\tilde{u}_2$ is physically relevant.

For plotting purposes, the conversion from σ to an equivalent frequency is needed. Taking the wavelet transform of $\cos(2\pi\omega t)$, two simple conversions can be adopted: the peak of the compensated energy spectrum corresponds to $\omega\sqrt{\sigma} = 1/\pi\sqrt{8}$, or the centroid of the spectrum coincides with $\omega\sqrt{\sigma} = 1/2\pi$. The second alternative is adopted here, with the largest ω equal to the Nyquist frequency of our discrete signal.

The example signal (Fig. 22.26) and its Mexican-hat wavelet map are shown in Fig. 22.27.

The largest wavelet coefficients (red for minima, blue for maxima) identify individual extrema of the

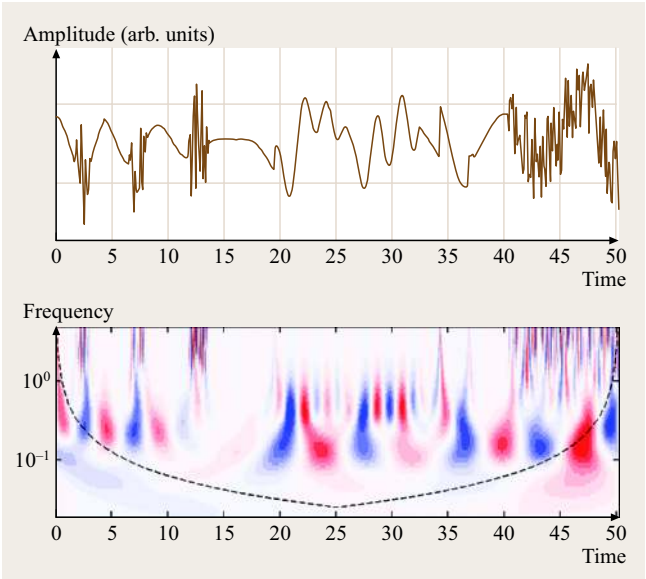

Fig. 22.27 Mexican hat wavelet map $\sigma\tilde{s}_2$ (*bottom*) and signal (*top*). The cone of influence of end-points is also shown

signal. The near-periodicity of one contribution to the signal is visible in the energetic contributions along a horizontal strip of the map. The noise is intermittently distributed in the top third of the map, corresponding to larger frequencies. Additional features are discussed in connection with the Morlet transform.

Cone of Influence and End Effects. For a wavelet located at a fixed time, increasing its scale from some very small value gradually brings a larger part of the signal into the wavelet's view, generating the cone of influence of the wavelet. Signal values within the cone of influence affect the wavelet coefficient at that scale. If the wavelet is located near either end of a signal, it will see whatever information is located beyond the end-points, or the lack of information; the corresponding wavelet coefficients are of questionable value. Various techniques such as wrap-around (implied periodicity of the signal), mirror symmetry or zero padding do not entirely eliminate this problem, and results should be interpreted accordingly. Periodicity is used throughout the examples below. The cone of influence is the envelope, for some suitably low threshold (2% of maximum in this case), of the wavelet coefficients $\tilde{u}$ of a Dirac function located at position t_0 or t_{N-1}. It is recommended that the cone of influence of end-points be shown as a reminder that the wavelet coefficients within the cone should be used with caution.

Morlet Wavelet. The Morlet wavelet is complex-valued, and consists of a Fourier wave train inside a Gaussian envelope of width z_0/π:

$$\psi_{M,z_0}(t) = \left(e^{2i\pi t} - e^{-\frac{z_0^2}{2}}\right) e^{-2\pi^2 t^2/z_0^2} . \qquad (22.141)$$

The envelope factor z_0 controls the number of oscillations in the wave packet; a value of $z_0 = 5$ is generally adopted, with the result shown on Fig. 22.24. The correction factor $e^{-z_0^2/2}$, making the wavelet admissible, is very small for $z_0 \geq 5$ and often neglected. The Fourier transform is

$$\hat{\psi}_{M,z_0} = \frac{z_0}{2\sqrt{\pi}} e^{-\frac{z_0^2}{2}(1+\omega^2)} \left(e^{-z_0^2\omega} - 1\right) . \qquad (22.142)$$

There is apparently no closed-form expression of c_ψ, but numerical integration presents no difficulty and yields the values shown in Table 22.1.

Instead of the usual dilation factor a, we adopt its inverse $\omega = 1/a$, which is its own equivalent frequency. For normalization, we adopt

$$\Psi_M(t\omega) = \frac{\omega}{\sqrt{c_\psi}} \psi_{M,z_0}(t\omega) . \qquad (22.143)$$

Then, the three basic formulae are, for the transform

$$\tilde{u}_M = \int u(t') \Psi_M^*[(t-t')\omega] \, dt' , \qquad (22.144)$$

for the energy of the signal

$$\int dt \frac{u^2}{2} = \frac{1}{2} \iint |\tilde{u}_M|^2 \frac{d\omega}{\omega} dt , \qquad (22.145)$$

and for the inverse transform

$$u(t) = \iint \Psi_M[(t-t')\omega] \tilde{u}_M(t', \omega) \frac{d\omega}{\omega} dt . \qquad (22.146)$$

Figure 22.28 shows the norm and phase of the Morlet transform of our signal.

Comparison and Interpretation. Similarities and differences between Figs. 22.27 and 22.28 are equally informative.

The cone of influence of the end-points is wider for the Morlet wavelet: this is not surprising, since the wavelet captures several oscillations at a given frequency, whereas the Mexican-hat wavelet only covers one-and-a-half periods. The better frequency resolution of Morlet is counterbalanced by its broader temporal resolution. The wavelet coefficients within the cone of influence of the end-points are necessary for energy conservation and signal reconstruction, but should not

blindly be interpreted as physical events (although the presence of oscillations at time $t > 40$ and of a maximum at $t = 47$ are not in doubt in the example).

Local spectral intensity (as measured by the wavelet coefficients) is concentrated in the same frequency band around $\omega \approx 0.3$. In the time–frequency resolution tradeoff, the Morlet wavelet gives a much narrower frequency spread for the dominant wave, whereas the Mexican-hat wavelet identifies individual extrema of the signal in time. In the Morlet case, one weak energetic band at lower frequency is associated with the signal modulation, and at yet a lower frequency with end-effects (wrap-around creates periodicity).

At times 42 to 50, and frequencies larger than 0.6, we see a scattering of events that is due to the interplay of random number generation and the wavelet's reproducing kernel (see the next paragraph).

Interpretation: Reproducing Kernel. The mapping of $u(t)$ from the time axis to the wavelet half-plane (time and scale) shows that the continuous wavelet representation is redundant, which implies that the wavelet coefficients are not independent of one another. The various patterns observed in the wavelet coefficients reflect a combination of the features of the signal and of the wavelet used for the analysis. Mathematically, this is shown by substituting the expression for the inverse transform in the direct transform relation; simple rearrangement yields

$$\tilde{u}(a,t) = \iint K(a,t,a',t'')\tilde{u}(a',t'')\,\mathrm{d}a'\,\mathrm{d}t'' \,,$$

where the reproducing kernel K is

$$K = \frac{1}{c_\psi \sqrt{a} a'^{5/2}} \times \int \left[\psi\left(\frac{t'-t''}{a'}\right)\psi^*\left(\frac{t-t'}{a}\right)\right]\mathrm{d}t' \,.$$

The reproducing kernel provides structure to the field of wavelet coefficients through the integral equation above, by which the wavelet coefficient at any point captures information from its vicinity as weighted by K, itself dependent on the wavelet shape.

Alternatively, it can be shown that, in the case of the Mexican-hat wavelet, the structure of the field of coefficients is such that

$$\partial_\sigma \tilde{u}_2 = \partial_u^2 \tilde{u}_2 \,.$$

This is a compatibility condition for $\tilde{u}(\sigma, t)$ to be the Mexican-hat transform of a signal $u(t)$. (Note that we plot $\sigma\tilde{u}_2$, which obeys a related partial differential equation.) The compatibility equation for the Morlet wavelet is much more complicated.

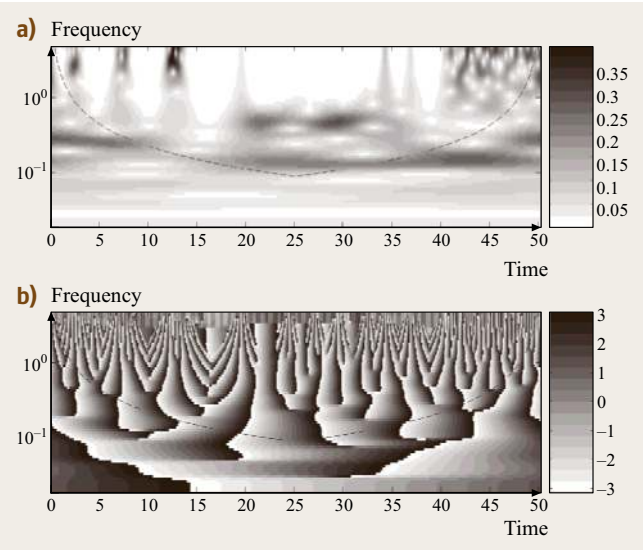

Fig. 22.28a,b Norm (**a**) and phase (**b**) of the Morlet transform of our signal. Also shown is the cone of influence of the end-points

Thinking of the analyzing wavelet as a template for features of the signal, the main difference between the Morlet and Mexican-hat shapes is the local periodicity of the former as opposed to the central minimum (with two side maxima for admissibility) of the latter. Large wavelet coefficients are associated with a good match of shape at the right scale and location, but the pattern recognition is far from perfect. The Mexican-hat wavelet responds to any local maximum or minimum of the signal, and will do so over a range of scales; the Morlet wavelet is better suited to respond to a sequence of maxima and minima, of which the location is harder to pinpoint but the frequency is more narrowly determined.

22.6.3 Orthogonal Wavelet Transform

Discrete Wavelets

It is possible to obtain a discrete set of quasi-orthogonal wavelets by sampling the dilation and time axes a and b. For the scale a we use a logarithmic discretization, i. e., a is replaced by $a_j = a_0^{-j}$ where a_0 is the sampling rate of the $\log a$ axis [$a_0 = \Delta(\log a)$] and where $j \in \mathbb{Z}$ is the scale index. The position b is discretized linearly, i. e., b is replaced by $t_{ji} = ib_0 a_0^{-j}$, where b_0 is the sampling rate of the position axis at the largest scale and where $i \in \mathbb{Z}$ is the position index. Note that the sampling rate

of the position varies with scale, i. e., for finer scales (increasing j and hence decreasing a_j) the sampling rate increases. Accordingly we obtain discrete wavelets

$$\psi_{ji}(t) = \frac{1}{\sqrt{a_j}}\psi\left(\frac{t - t_{ji}}{a_j}\right) \tag{22.147}$$

and the corresponding discrete decomposition formula is

$$\tilde{u}_{ji} = \langle \psi_{ji}, u\rangle = \int_{-\infty}^{\infty} u(t)\psi^*_{ji}(t)\,\mathrm{d}t \tag{22.148}$$

with $\langle u, v\rangle = \int_{-\infty}^{+\infty} u(t)v^*(t)\,\mathrm{d}t$ being the scalar product in energy norm, i. e., for signals of finite energy such as those encountered in fluid mechanics.

The discrete reconstruction formula is

$$u(t) = C\sum_{j=-\infty}^{+\infty}\sum_{i=-\infty}^{+\infty}\tilde{u}_{ji}\psi_{ji}(t) + R(t)\,, \tag{22.149}$$

where C is a constant and $R(t)$ is a residual, both of which depend on the choice of the wavelet and the sampling of the scale and position axes. For the particular choice $a_0 = 2$ (which corresponds to a scale sampling by octaves) and $b_0 = 1$ we have the dyadic sampling, for which there exist special wavelets ψ_{ji} that form an orthonormal basis, i. e.,

$$\langle \psi_{ji}, \psi_{j'i'}\rangle = \delta_{jj'}\delta_{ii'}\,, \tag{22.150}$$

where δ denotes the Kronecker symbol. This means that the wavelets ψ_{ji} are orthogonal with respect to their translates by discrete steps $2^{-j}i$ and their dilates by discrete steps 2^{-j} corresponding to octaves. In this case the reconstruction formula is exact with $C = 1$ and $R = 0$, but the discrete wavelet transform has lost the invariance by translation and dilation of the continuous one.

Orthogonal Wavelets

The construction of orthogonal wavelet bases and the associated fast numerical algorithms are based on the mathematical concept of multiresolution analysis (MRA). The underlying idea is to consider approximations u_j of the signal $u(t)$ at different scales j. The amount of information needed to go from a coarse approximation u_j to a higher-resolution approximation u_{j+1} is then described using orthogonal wavelets. The orthogonal wavelet analysis can thus be interpreted as decomposing the signal into approximations of the signal at coarser and coarser scales (i. e., for decreasing j) where the differences between the approximations are encoded using wavelets.

The coarse-graining at a given scale is done by filtering the signal with the scaling function ϕ. As a filter, the scaling function ϕ does not have vanishing mean but is normalized $\int_{-\infty}^{\infty}\phi(t)\,\mathrm{d}t = 1$. We construct translated and dilated versions of ϕ

$$\phi_{ji}(t) = 2^{j/2}\phi(2^j t - i)\,. \tag{22.151}$$

This basis ϕ_{ji} is orthonormal at a given scale j with respect to its translates by steps $i/2^j$

$$\langle \phi_{ji}, \phi_{ji'}\rangle = \delta_{ii'} \tag{22.152}$$

but not to its dilates, in contrast to wavelets. In general there is no explicit expression for the scaling function. However, the scaling function satisfies a so-called refinement equation:

$$\phi_{j-1,i}(t) = \sum_{n=-\infty}^{+\infty} h_{n-2i}\phi_{jn}(t) \tag{22.153}$$

with the coefficients $h_i = \langle \phi_{ji}, \phi_{j-1,0}\rangle$. These coefficients determine the scaling function completely. Equation (22.153) implies that the approximation of a coarser scale can be described by linear combinations of the signal at finer scales, which corresponds to a nestedness of the approximation space.

The associated wavelet ψ is a linear combination of the scaling function ϕ,

$$\psi_{ji}(t) = \sum_{n=-\infty}^{+\infty} g_{n-2i}\phi_{jn}(t) \tag{22.154}$$

with coefficients $g_n = \langle \phi_{jn}, \psi_{j-1,0}\rangle$. These filter coefficients g_n are computed from the filter coefficients h_n using the relation

$$g_n = (-1)^{1-n}h_{1-n}\,. \tag{22.155}$$

As in the continuous case, the wavelets have at least vanishing mean, and also possibly vanishing higher-order moments, i. e.,

$$\int_{-\infty}^{+\infty} t^m\psi(t)\,\mathrm{d}t = 0 \quad \text{for } m = 0, \ldots, M-1\,. \tag{22.156}$$

Now we consider approximations of the signal $u(t)$ at two different scales j

$$u_j(t) = \sum_{i=-\infty}^{+\infty}\overline{u}_{ji}\phi_{ji}(t) \tag{22.157}$$

and $j-1$

$$u_{j-1}(t) = \sum_{i=-\infty}^{+\infty} \overline{u}_{j-1,i}\phi_{j-1,i}q(t) \tag{22.158}$$

with the scaling coefficients

$$\overline{u}_{ji} = \langle u, \phi_{ji}\rangle \tag{22.159}$$

which correspond to local averages of the signal u at position $i2^{-j}$ and at scale 2^{-j}. The difference between the two approximations is described by the wavelets

$$u_j(t) - u_{j-1}(t) = \sum_{i=-\infty}^{+\infty} \tilde{u}_{j-1,i}\psi_{j-1,i}(t) \tag{22.160}$$

with the wavelet coefficients

$$\tilde{u}_{ji} = \langle u, \psi_{ji}\rangle\,, \tag{22.161}$$

which correspond to local differences of the signal at position $(2i+1)2^{-(j+1)}$ between approximations at scales 2^{-j} and $2^{-(j+1)}$.

Iterating the two-scale decomposition (22.160), any signal $u(t)$ of finite energy can be expressed as a sum of a coarse-scale approximation at a reference scale j_0, and their successive differences (the details needed to go from one scale j to the next smaller scale $j+1$ for $j = j_0, \ldots, J-1$),

$$u(t) = \sum_{i=-\infty}^{+\infty} \overline{u}_{j_0 i}\phi_{j_0 i}(t) + \sum_{j=j_0}^{J}\sum_{i=-\infty}^{+\infty} \tilde{u}_{ji}\psi_{ji}(t)\,. \tag{22.162}$$

In numerical applications the sums in theis equation have to be truncated in both scale j and position i. The truncation in scale corresponds to a limitation of u to a given finest scale J, which is in practice imposed by the available sampling rate. Due to the finite length of the available data the sum over i becomes also finite. The decomposition (22.162) is orthogonal, as, by construction,

$$\langle \psi_{ji}, \psi_{lk}\rangle = \delta_{jl}\delta_{ik}\,, \tag{22.163}$$

$$\langle \psi_{ji}, \phi_{lk}\rangle = 0 \quad \text{for } j \geq l \tag{22.164}$$

in addition to (22.152).

Fast Wavelet Transform

Starting with a signal u given at the finest resolution 2^{-J}, i. e., we know u_J and hence the coefficients $\overline{u}_{Ji}$ for $i \in \mathbb{Z}$, the fast wavelet transform computes its wavelet coefficients $\tilde{u}_{ji}$ by successively decomposing each approximation u_J into a coarser-scale approximation u_{J-1}, plus their differences, encoded by the wavelet coefficients. The algorithm uses a cascade of discrete convolutions with the filters h_n (low pass filter) and g_n (band pass), followed by down-sampling, i. e., we retain one coefficient out of two.

- Initialization: given $u \in L^2(\mathbb{R})$ and $\overline{u}_{Ji} = u\left(\frac{i}{2^J}\right)$ for $i \in \mathbb{Z}$.
- Decomposition: for $j = J$ to 1, step -1, do

$$\overline{u}_{j-1,i} = \sum_{n\in\mathbb{Z}} h_{n-2i}\overline{u}_{jn} \tag{22.165}$$

$$\tilde{u}_{j-1,i} = \sum_{n\in\mathbb{Z}} g_{n-2i}\overline{u}_{jn}\,. \tag{22.166}$$

The inverse wavelet transform is based on successive reconstructions of a fine-scale approximation u_j from the coarser-scale approximation u_{j-1}, plus the differences between approximations at scale $j-1$ and the smaller scale j that are encoded by $\tilde{u}_{j-1,i}$. The algorithm uses a cascade of discrete convolutions with the filters h_n and g_n, plus up-sampling. The up-sampling is obtained by adding zeros between two successive coefficients.

- Reconstruction: for $j = 1$ to J, step 1, do

$$\overline{u}_{ji} = \sum_{n=-\infty}^{+\infty} h_{i-2n}\overline{u}_{j-1,n} + \sum_{n=-\infty}^{+\infty} g_{i-2n}\tilde{u}_{j,n}\,. \tag{22.167}$$

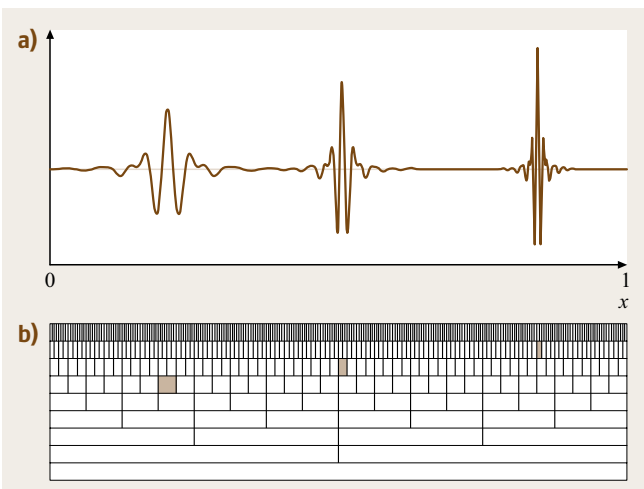

Fig. 22.29a,b Orthogonal quintic spline wavelets $\psi_{j,i}(t) = 2^{j/2}\psi(2^j t - i)$ at different scales and positions: $\psi_{5,6}(t)$, $\psi_{6,32}(t)$ $\psi_{7,108}(t)$ **(a)** and corresponding wavelet coefficients **(b)**

Examples of Orthogonal Wavelets

Orthogonal wavelets (constituting an MRA) are typically defined by their filter coefficients h_n and for most no explicit expression for ψ is available. In the following we give filter coefficients of h_n for typical orthogonal wavelets. The filter coefficients of g_n can be obtained using the quadrature relation between the two filters (22.155).

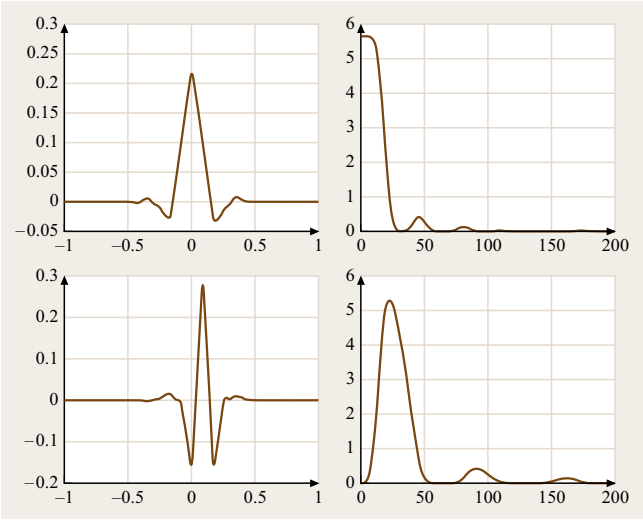

Fig. 22.30 Orthogonal wavelets Coiflet 12. *Top*: scaling function $\phi(t)$ (*left*) and $|\hat{\phi}(\omega)|$. *Bottom*: wavelet $\psi(t)$ (*left*) and $|\hat{\psi}(\omega)|$

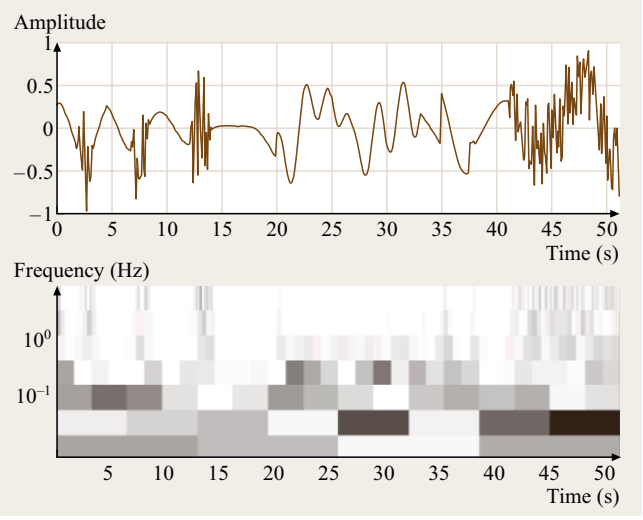

Fig. 22.31 Absolute value of the orthogonal wavelet transform of our signal using Coiflet 12 wavelets

- Haar D1 (one vanishing moment):

$$h_0 = \frac{1}{\sqrt{2}} ,$$
$$h_1 = \frac{1}{\sqrt{2}} .$$

- Daubechies D2 (two vanishing moments):

$$h_0 = \frac{(1+\sqrt{3})}{4\sqrt{2}} = 0.482962913145 ,$$
$$h_1 = \frac{(3+\sqrt{3})}{4\sqrt{2}} = 0.836516303736 ,$$
$$h_2 = \frac{(3-\sqrt{3})}{4\sqrt{2}} = 0.224143868042 ,$$
$$h_3 = \frac{(1-\sqrt{3})}{4\sqrt{2}} = -0.129409522551 .$$

- Coiflets: coefficients, too numerous to appear here, are listed in other sources [22.98]; wavelets are shown on Fig. 22.30.

As an example (Fig. 22.31), we develop the signal $u(t)$, sampled on $N = 2^J$ points, as an orthonormal wavelet series from the largest scale $a_{\max} = 2^0$ to the smallest scale $a_{\min} = 2^{-J}$:

$$u(t) = \sum_{j=0}^{J-1} \sum_{i=0}^{2^j-1} \tilde{u}_{ji} \psi_{ji}(t) . \qquad (22.168)$$

Comparing the orthogonal wavelet transform (Fig. 22.31) with the continuous versions (Figs. 22.27 and 22.28) shows qualitative agreement in the distribution of coefficients. The cone of influence depends on the filter length L of g and h (22.153, 155). On the finest scale $L/2-1$ coefficients on the left and on the right maybe be influenced by boundary effects. At larger scales, the number of influenced coefficients increases accordingly (22.165, 166). Note that for the Haar wavelet ($L = 2$), no boundary effects are present.

We note two other differences. First, the orthogonal wavelet uses very few coefficients to describe the large-scale features. For a signal of N points, the highest resolution (Nyquist) requires $N/2$ points, the next highest $N/4$, and so forth, so that a total of N wavelet coefficients for all scales are needed for an exact reconstruction. This contrasts with the $N\dot{M}$ continuous wavelet coefficients, where M is the number of discretized frequencies for an approximate reconstruction. Although the $N \cdot M$ number can be improved upon, this justifies the use of orthogonal wavelets whenever the

economy of representation is critical (numerical simulation, data storage and transmission). Second, the subtle variations in frequency in the signal are not readily diagnosed from the orthogonal transform, because of the scale discretization into octaves.

22.6.4 Applications in Experimental Fluid Mechanics

In this section we describe some diagnostics based on the continuous and orthogonal wavelet transform. The diagnostics can be local (properties of single coefficients) or collective (properties of groups of coefficients or statistics based on them). While our purpose is to illustrate the strengths of wavelet-based methods, we also caution about some possible misuses. We will illustrate the ideas on our artificial signal which contains, by construction, a number of the observed features that might be difficult to isolate with other techniques; and mention a few published results from a rapidly evolving archival list. This is about data interrogation: from the selection of the wavelet to the processing algorithms, each subsection should be read as an example of a question made possible by wavelet analysis, and the corresponding quantitative answer.

Energy Distribution

Energy Maps. The total energy of the signal, normalized per unit time, is

$$E = \frac{1}{T}\int_0^T \frac{u^2}{2}\,\mathrm{d}t\ . \tag{22.169}$$

The Parseval relations for Fourier and wavelets (Mexican hat, Morlet, and orthogonal take the subscripts 'F', '2', 'M', and 's', respectively) give the expressions

$$\begin{aligned} E &= \frac{1}{T}\int E_\mathrm{F}\,\mathrm{d}\omega = \frac{1}{T}\int E_2\,\mathrm{d}\omega \\ &= \frac{1}{T}\int E_\mathrm{M}\,\mathrm{d}\omega = \frac{1}{T}\sum_{i,j} E_\mathrm{s}(\omega_j, t_i)\ . \end{aligned} \tag{22.170}$$

On this basis, we can define the local scalogram (or energy distribution in time and frequency), and, after time integration/summation, the global scalogram (or mean energy spectrum) as an alternative to the Fourier spectrum.

We remark that, for mean spectra or for local spectra, many distinct distributions of energy are possible, adding to the same total energy. The interpretation of the various options, and their relation to the Fourier spectrum, are discussed in the following subsections.

Local Spectra. Since each scale 2^{-j} of the wavelet ψ_j is inversely proportional to the mean wavenumber $\omega_j = \omega_\psi 2^j$. The local wavelet spectrum is then defined as

$$E_\mathrm{s}(\omega_j, t_i) = |\tilde{u}_{ji}|^2 \frac{2^j}{\omega_j}\ . \tag{22.171}$$

By measuring $E_\mathrm{s}(\omega_j, t_i)$ at different positions t_i, one can study how the energy spectrum depends on local flow conditions and estimate the contribution to the overall Fourier energy spectrum of different components of the flow. For example, one can determine the scaling of the energy spectrum contributed by coherent structures, such as isolated vortices, and the scaling of the energy spectrum contributed by the unorganized part of the flow. The spatial variability of the local wavelet spectrum $E_\mathrm{s}(\omega_j, t_i)$ measures the flow's intermittency and lends itself to conditional sampling.

A comparison of the Mexican-hat and Morlet compensated spectra is shown on Fig. 22.32.

It was verified that the integral adds up to the signal's energy for each case. While the spatial and spectral energies are similar in some respects, the details reflect the properties of the corresponding wavelets. The most obvious common feature is that most of the energy is concentrated in a small region of the wavelet half-plane: most wavelet coefficients contribute negligible energy to the signal. This is the basis for wavelet compression algorithms.

Mean Spectra. When one integrates the local wavelet spectrum over time, one gets the global wavelet spec-

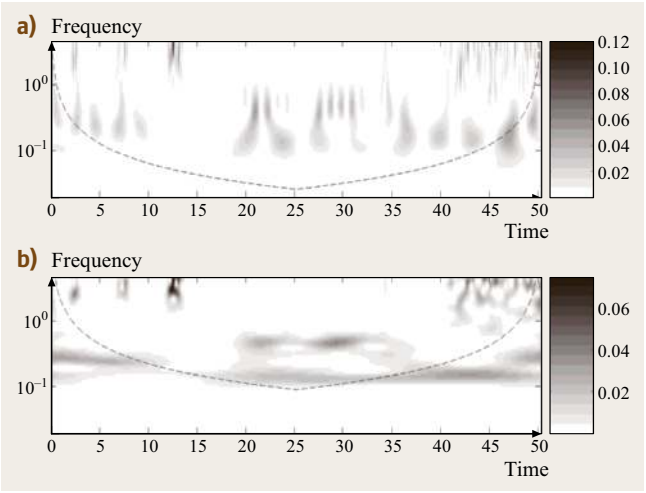

Fig. 22.32a,b Compensated local spectra of our test signal with the Mexican-hat (ωE_2, (**a**)) and Morlet (ωE_M, (**b**)) wavelets

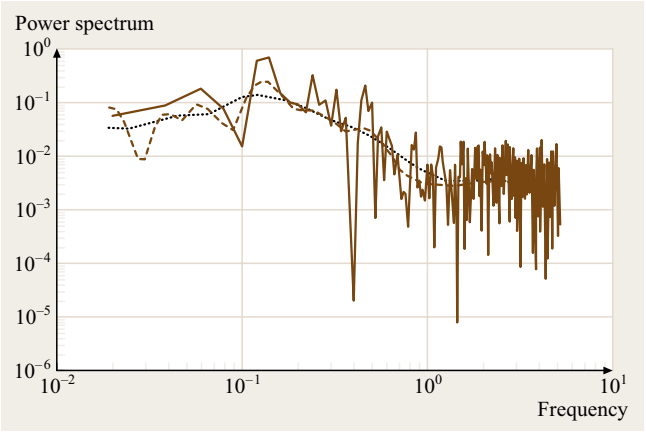

Fig. 22.33 Fourier (E_F, *solid line*), and mean Mexican-hat (E_2, *dotted line*) and Morlet (E_M, *dashed line*) mean power spectra

trum. The Fourier spectrum (Fig. 22.33) appears very noisy, which is due to the brevity of our signal (512 points) combined with its various intermittent features. The power spectrum $E(\omega)$ shows the dominant mid frequencies; at high frequencies, we have a combination of noise and corrections for nonsinusoidal low-frequency content and for intermittent events.

The Morlet spectrum is a smoother alternative to the Fourier spectrum, obtained by squaring the wavelet coefficients, and summing them at each frequency. The dominant lower frequencies stand out, but the familiar Fourier scatter is absent: this is a consequence of the wavelet coefficients being band-pass-filtered Fourier coefficients, with the spectrum of the wavelet as the filter shape. Depending on the application, such drastic smoothing can be an advantage or a weakness of the mean wavelet spectra compared to the Fourier spectra.

The wider spectrum of the Mexican-hat wavelet leads to further smoothing, so much that the low-frequency peaks are no longer distinct, but merge into a broader clump. This illustrates the time–frequency resolution compromise associated with wavelet selection.

Relation to Fourier Spectrum. Although the wavelet transform analyzes the flow into wavelets rather than complex exponentials, it has been shown that the global wavelet spectrum converges to the Fourier spectrum provided that the analyzing wavelets have enough cancellations. More precisely the global wavelet spectrum (with $\tilde{E}$ standing for either E_F, E_2 or E_M) is

$$\tilde{E}(\omega) = \int_0^{+\infty} \tilde{E}(\omega, t)\,\mathrm{d}t \qquad (22.172)$$

gives the correct Fourier exponent for a power-law Fourier energy spectrum $E_F(\omega) \propto \omega^{-\beta}$ if the analyzing wavelet has at least $m > (\beta - 1)/2$ vanishing moments. Thus, the steeper the energy spectrum, the more vanishing moments the analyzing wavelet should have. The inertial range in turbulence has a power-law behavior. The ability to correctly characterize power-law energy spectra is therefore an important property of the wavelet transform (which is related to its ability to detect and characterize singularities).

The global wavelet spectrum $\tilde{E}(\omega)$ is a smoothed version of the Fourier spectrum $E_F(\omega)$. This can be seen from the following relation between the two spectra

$$\tilde{E}(\omega) = \frac{1}{C_\psi \omega_\psi} \int_0^{+\infty} E(\omega') |\hat{\psi}\left(\frac{\omega_\psi \omega'}{\omega}\right)|^2 \,\mathrm{d}\omega' \qquad (22.173)$$

which shows that the global wavelet spectrum is an average of the Fourier spectrum weighted by the square of the Fourier transform of the wavelet ψ shifted at wavenumber ω. Note that the larger ω is, the larger the averaging interval, because wavelets are bandpass filters with $\frac{\Delta\omega}{\omega}$ constant. This property of the global wavelet spectrum is particularly useful for turbulent flows. Indeed, the Fourier spectrum of a single realization of a turbulent flow is too oscillatory to clearly detect a slope, but this is not an issue for the smoother global wavelet spectrum.

For instance, the real-valued Mexican-hat wavelet has only two vanishing moments and thus can correctly measure energy spectrum exponents up to $\beta < 5$. In the case of the complex-valued Morlet wavelet (22.141), only the zeroth-order moment is zero, but the higher m-th-order moments are very small ($\propto \omega_0^{2m+1} \mathrm{e}^{(-\omega_0^2/2)}$) provided that ω_0 is larger than 5. Therefore the Morlet wavelet transform gives accurate estimates of the power-law exponent of the energy spectrum at least for approximately $\beta < 7$ (if $\omega_0 = 6$). There is also a family of wavelets with an infinite number of cancellations

$$\hat{\psi}_k(\omega) = \alpha_k \exp\left[-\frac{1}{2}\left(\omega^2 + \frac{1}{\omega^{2k}}\right)\right], \quad k \geq 1\,, \qquad (22.174)$$

where α_k is chosen for normalization. These wavelets can therefore correctly measure any power-law energy spectrum, and detect the difference between a power-law energy spectrum and a Gaussian energy spectrum $E(\omega) \propto \mathrm{e}^{-(\omega/\omega_\psi)^2}$. For instance in turbulence this wavelet can identify the changing spectral slopes around the Kolmogorov microscale and into the dissipative range of the spectrum.

Ridges. In some applications, the signal may be primarily oscillatory, but with modulation of the frequency and amplitude. Extracting these oscillations and quantifying the modulation can be done from the continuous wavelet map. One algorithm consists of identifying the ridges of the energy distributions, i. e., the coordinates of the points in time at which the compensated energy spectrum has a local spectral maximum. In Fig. 22.34, we plot the ridge lines of the Mexican-hat and Morlet energy distributions. The Morlet wavelet is a better template for localized oscillations, and emphasizes the locally periodic structure of the signal. In contrast, although local periodicity is visible on the Mexican-hat energy map, the ridge lines do not capture the continuity of wave trains. While remedies exist for this shortcoming of the Mexican-hat wavelet, the Morlet wavelet is a more natural tool for this application.

Even when the frequency modulation is very small, the relevant physics can be detected through related modulations in the amplitude and or phase discontinuities along the ridge line. This technique has been successfully used to unravel the interactions between modes in shear layers.

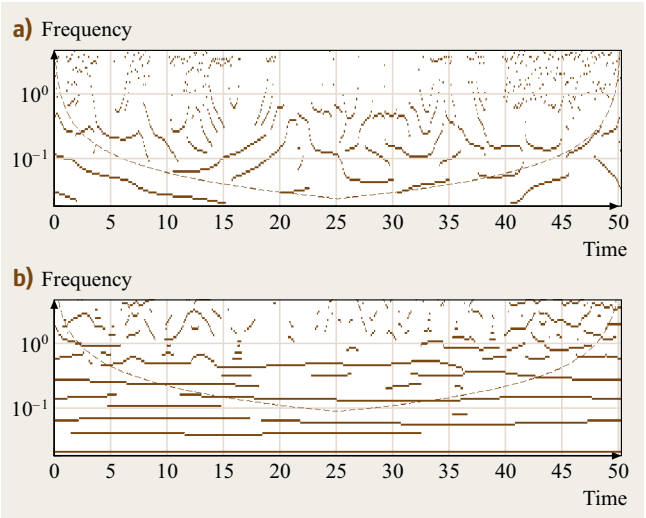

Fig. 22.34a,b Ridge lines of the Mexican-hat **(a)** and Morlet transforms **(b)**, showing the frequency modulation of the energetic contributions to the signal

Lines of Modulus Maxima. A skeleton of the continuous wavelet transform can also be obtained by mapping its modulus maxima at each frequency. In the case of real-valued wavelets, these alternate with the lines of zero crossing (sign change). The skeleton combines information about the signal and the wavelet (reproducing kernel), as shown in Fig. 22.35. For a given signal, the particulars of the skeleton are clearly wavelet dependent, and should be interpreted with caution. However, statistically the skeleton provides useful partitions of the wavelet half-plane.

While modulus maxima and zero-crossing lines are topologically equivalent, the values of the extrema on the former contain more information. At any given frequency, the wavelet transform can be approximated between extrema by interpolating a smooth monotonic function. Thus, the knowledge of the wavelet coefficients along the lines of modulus maxima is sufficient to reconstruct the wavelet map, and thereby the signal. In conjunction with thresholding of the wavelet coefficients, this can be used for data compression and for computing multifractal statistics.

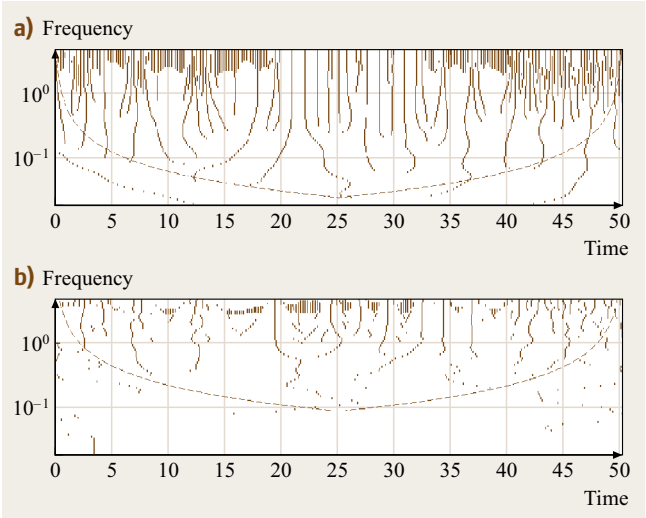

Fig. 22.35a,b Lines of modulus maxima for the Mexican-hat **(a)** and Morlet **(b)** wavelets

Intermittent Fluctuations. One of the advantages of the time–frequency representation is the ability to define and compute error bars to supplement the mean spectra. In intermittent cases, the (squared) wavelet coefficients show considerable variability in time, and a corresponding standard deviation can be calculated at each scale. The result, using additive rather than logarithmic departures from the mean, is shown in Fig. 22.36.

The error bars are taken as covering the mean, plus or minus three standard deviations. The lower end of the error bars corresponds to negative energies, and is assimilated to zero; the profile of the top of the error

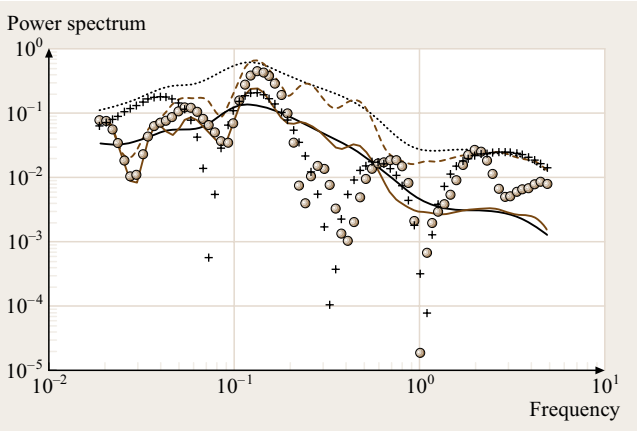

Fig. 22.36 Mean Morlet and Mexican-hat mean power spectra (*solid lines*), as in Fig. 22.33, and their error bar profile as *dashed line* (Mexican hat) and *dotted line* (Morlet); also the local spectra at $t = 45$: Mexican hat (*circles*) and Morlet (*crosses*)

bars is shown. It is seen that the error bars can be larger than the mean by a factor of 3–4 at low frequencies, and considerably more at high frequencies, for our signal. A larger bracket around the mean spectrum has been interpreted as an indicator of intermittency in homogeneous turbulence.

The superposition of the local spectra (scaled per unit duration of signal) is also informative. First, there is considerable difference between the Morlet and Mexican-hat local energies Fig. 22.32) – as was obvious from the wavelet maps (Figs. 22.28 and 22.27). At $\omega \approx 0.15$, the local energies contribute to one of the dominant peaks: the smallest dominant frequency is represented at this time. The larger Morlet energy is indicative of an oscillation at this frequency. In contrast, at $\omega \approx 0.045$, the larger Mexican-hat energy content captures the large, single bump better than Morlet. At $\omega \approx 3$–4, the double peak of Morlet coefficients is matched by a much larger single peak of the Mexican-hat coefficients: this combines the random noise and the reproducing kernel for this particular instant, and is very different at nearby points.

Also noteworthy is that the Mexican-hat energies around $\omega = 4$ lie outside the three-standard-deviation bracket. In general, this can be attributed to several possible causes. First, the difference in magnitude between Morlet and Mexican-hat energies indicates that an individual event, rather than an oscillation, is present in this vicinity; such an event could be a statistical outlier. Second, in this instance, the mean spectrum and the standard deviation are ensemble statistics, underestimating the (intermittent) noise energy content per unit time. This points to the need for conditional statistics.

Intermittency Measures. We now turn to intermittency, which is defined as localized bursts of high-frequency activity. This means that intermittency is a phenomenon localized in both physical space and spectral space, and thus a suitable basis for representing intermittency should reflect this dual localization.

To measure intermittency we use the space-scale information contained in the wavelet coefficients to define scale-dependent moments and moment ratios. Useful diagnostics to quantify the intermittency of a signal $u(t)$ are the moments of its wavelet coefficients at different scales j,

$$M_{p,j}(u) = 2^{-j} \sum_{i=0}^{2^j-1} |\tilde{u}_{ji}|^p \,. \tag{22.175}$$

Note that $E_j = 2^j M_{2,j}$.

The sparsity of the wavelet coefficients at each scale is a measure of intermittency, and it can be quantified using ratios of moments at different scales,

$$Q_{p,q,j}(u) = \frac{M_{p,j}(u)}{[M_{q,j}(u)]^{p/q}} \,. \tag{22.176}$$

Classically, one chooses $q = 2$ to define typical statistical quantities as a function of scale. Recall that for $p = 4$ we obtain the scale-dependent flatness $F_j = Q_{4,2,j}$. It is equal to 3 for Gaussian white noise at all scales j, which proves that this signal is not intermittent. The scale-dependent skewness, hyperflatness, and hyperskewness are obtained for $p = 3$, 5 and 6, respectively. For intermittent signals $Q_{p,q,j}$ increases with j.

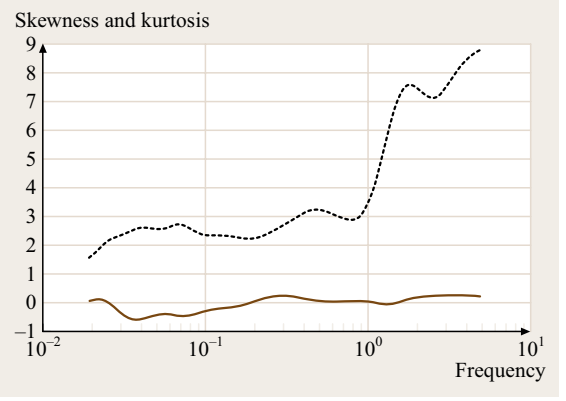

Fig. 22.37 Scale dependence of the skewness (*solid line*) and flatness (*dashed line*)

On Fig. 22.37, we show the frequency-dependent skewness and kurtosis of our test data, calculated based on the Mexican-hat coefficients. The skewness hovers around zero, and the kurtosis around 3 at low frequencies. The larger kurtosis values at higher frequencies confirms the intermittency of the noise interspersed in the data.

Various techniques have been used to separate outlier events from a background signal. One can mention the local intermittency measure (LIM) and large dissipative events.

Higher Moments and Scaling

The idea in this group of applications is that any line in the wavelet transform matrix can be treated as a time trace (band-pass-filtered data) with statistics in its own right. Auto- and cross-correlations can be found in the literature. The spectral error bars described already are another example.

Scaling describes the relation between moments of a signal at various scales. In particular, anomalous scaling relates to departures from Kolmogorov scaling for high-order moments of turbulent fields. Because of their intermittent and spectral content, wavelet coefficients can be used effectively to study anomalous scaling. By comparing results before and after filtering certain types of events, it has been possible to associate anomalous scaling with certain classes of events, such as coherent structures or highly dissipative eddies.

Relation to Structure Functions. Since its introduction to turbulence by Kolmogorov, the second-order structure function has been a frequently used diagnostic tool for the study of a turbulent signal $u(t)$. It is easy to measure and, moreover, Kolmogorov's theory of homogeneous and isotropic turbulent predicts its scaling exponent, which explains its wide use. It is defined as

$$S_2(\tau) = \int_{-\infty}^{\infty} [u(t+\tau) - u(t)]^2 \, \mathrm{d}t \; . \tag{22.177}$$

In this paragraph we link the scale-dependent moments of the wavelet coefficients to the structure functions and show that the global wavelet spectrum corresponds to the second-order structure function. Furthermore, we prove that the structure functions are *blind* to some scaling exponents and propose a way to overcome this limitation.

We first remark that the increments of a signal, also called the modulus of continuity, can be seen as its wavelet coefficients using the difference of Diracs (DOD) wavelet

$$\psi^{\delta}(t) = \delta(t+1) - \delta(t) \; . \tag{22.178}$$

We thus obtain

$$u(t+\tau) - u(t) = \tilde{u}_{t\tau} = \left\langle u, \psi^{\delta}_{t\tau} \right\rangle \tag{22.179}$$

with $\psi^{\delta}_{t\tau}(t) = 1/\tau\{\delta[(t-t')/\tau + 1] - \delta[(t-t')/\tau]\}$. Note that in this case the wavelet is normalized with $1/\tau$ normalization rather than $1/\sqrt{(}\tau)$. The p-th-order structure function $S_p(l)$ therefore corresponds to the p-th-order moment of the wavelet coefficients at scale τ,

$$S_p(\tau) = \int_{-\infty}^{\infty} [u(t+\tau) - u(t)]^p \, \mathrm{d}t = \int_{-\infty}^{\infty} (\tilde{u}_{t\tau})^p \, \mathrm{d}t \; . \tag{22.180}$$

As the DOD wavelet has only one vanishing moment (its mean), the exponent of the p-th-order structure function in the case of a self-similar behavior is limited by p, i. e., if $S_p(\tau) \propto \tau^{\zeta(p)}$ then $\zeta(p) < p$. To be able to detect larger exponents one has to use increments with a larger stencil, or wavelets with more vanishing moments, i. e., $\int t^m \psi(t) \, \mathrm{d}t = 0$ for $m = 0, 1, \ldots, M-1$.

We now concentrate on the case $p = 2$, i. e., the energy norm. Equation (22.172) gives the relation between the global wavelet spectrum $\tilde{E}(\omega)$ and the Fourier spectrum $E(\omega)$ for an arbitrary wavelet ψ. For the DOD wavelet we find, since $\hat{\psi}^{\delta}(\omega) = \mathrm{e}^{\iota\omega} - 1 = \mathrm{e}^{\iota\omega/2}(\mathrm{e}^{\iota\omega/2} - \mathrm{e}^{-\iota\omega/2})$ and hence $|\hat{\psi}^{\delta}(\omega)|^2 = 2(1 - \cos\omega)$, that

$$\tilde{E}(\omega) = \frac{1}{C_{\psi}\omega} \int_0^{\infty} E(\omega') \left[2 - 2\cos\left(\frac{\omega_{\psi}\omega'}{\omega} \right) \right] \mathrm{d}\omega' \; . \tag{22.181}$$

Setting $\tau = \omega_{\psi}/\omega$ and comparing with (22.177) we see that the wavelet spectrum corresponds to the second-order structure function, i. e.,

$$E_{\mathrm{s}}(\omega) = \frac{1}{C_{\psi}\omega} S_2(\tau) \; . \tag{22.182}$$

These results show that, if the Fourier spectrum behaves like $\omega^{-\alpha}$ for $\omega \to \infty$, $\tilde{E}(\omega) \propto \omega^{-\alpha}$ if $\alpha < 2M + 1$, where M is the number of vanishing moments of the wavelets. Consequently, we find for $S_2(\tau)$ that $S_2(\tau) \propto \tau^{\zeta(p)} = \left(\frac{\omega_{\psi}}{\omega}\right)^{\zeta(p)}$ for $\tau \to 0$ if $\zeta(2) \leq 2M$. In the present case we have $M = 1$, i. e., the second-order structure function can only detect slopes smaller than 2, corresponding to an energy spectrum with slopes shallower than -3. Thus we find that the usual structure function gives spurious results for sufficiently smooth signals.

Wavelet-based calculation of structure functions and their statistics (including anomalous scaling, above) has been documented.

Nonlinear Filtering

Nonlinear filtering is the common approach to denoising, data compression, coherent structure eduction, and associated conditional statistics. It consists in separating from a wavelet map any event meeting a physically relevant criterion, and reconstructing a filtered signal suitable for further processing. The quality of the results depends on the choices of wavelet and of event definition. In Fourier filtering, the presence of a spectral gap is highly desirable. In the wavelet representation, objective criteria for separating flow events need the same careful formulation. Different events, with different spectral and temporal signatures, might be captured with different wavelets; but a wavelet coefficient is not a flow structure, in the usual sense, unless the experimental definition of the event is reflected in the filtering algorithm.

Whether based on local intermittency measures, on being surrounded by a temporal–spectral gap, or related energy-based criteria, some thresholding is usually involved in the filtering scheme, and threshold sensitivity needs to be documented. One notable exception, which has been used for coherent structure eduction, is the mathematically proven optimality of some wavelets to separate a coherent signal from Gaussian noise, without adjustable thresholding parameters. This has been used effectively in two- (2-D) and three-dimensional (3-D) turbulence.

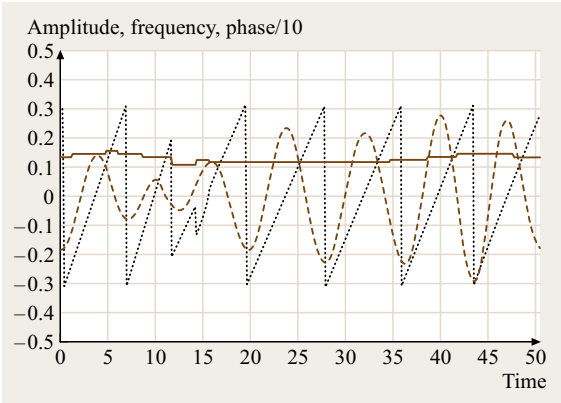

Fig. 22.38 The dominant oscillations (*dashed line*), its local frequency (*solid line*) and its phase (*dotted line*). The phase in $(-\pi, \pi)$ is divided by 10 for plotting convenience

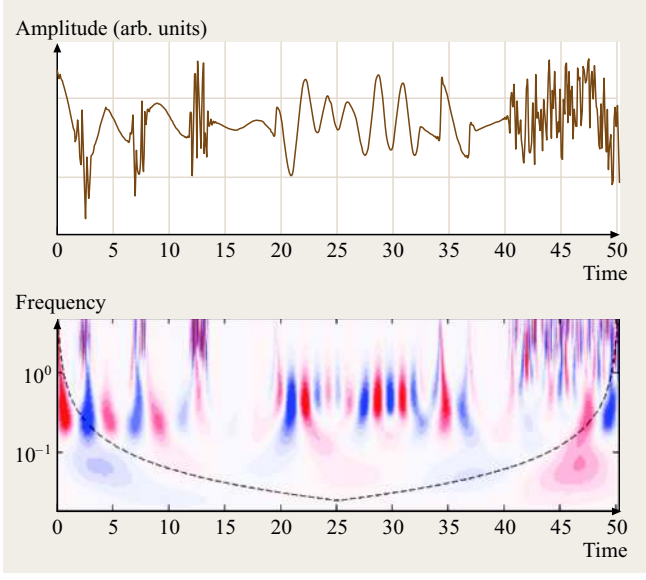

Fig. 22.39 The signal obtained by subtracting the dominant oscillations (Fig. 22.38) from the original signal (Fig. 22.26) and its Mexican-hat wavelet transform

Modulated Oscillations. For our signal, the mean spectra do not indicate a unique dominant periodicity, but several weak mid-frequency peaks can be identified. The Morlet wavelet, a template for local periodicity (over a time frame of only a few periods), enables us not only to extract the modulation, but also to quantify the frequency shifts already visible on Fig. 22.34. The algorithm consists of

1. searching, at each time, for the peak energy within range of scales (excluding the noisy high frequency band, for example)
2. recording the frequency and phase of the wavelet coefficients
3. canceling the wavelet coefficients outside this dominant mode (a spectral bracket of $\pm 10\%$ of peak local frequency has been retained here)
4. performing the inverse wavelet transform of the remaining coefficients to obtain a *filtered* signal. The result is shown on Fig. 22.38.

Comparing with Fig. 22.26, we observe that the clean part of the signal, between times 15 and 40, is extracted together with amplitude corrections caused by the isolated events of matching scale. The dominant frequency is seen to vary slightly, matching one of the ridge lines on Fig. 22.34, and increasing slightly towards both ends of the plot. Thus, depending on

the context, this oscillation could indicate a physical event. In contrast, in the first third of the signal, the ridge lines are broken, and we also see phase dislocations and erratic amplitude in Fig. 22.38. This happens because of interference from the oscillations at nearby frequencies, and from end-effects, so no carrier wave can be isolated unambiguously in this region. Additional physical insight, different wavelets and/or more-elaborate algorithms might modify this cautious conclusion.

Noteworthy is the relatively complex nature of the filter, made possible by the time–frequency representation. Furthermore, the small frequency shifts are easily observed, a trademark of continuous (Morlet in particular) wavelet transforms; for actual anemometric and acoustic traces, they have been associated, e.g., with subtle shear layer resonances. Finally, the phase of this nonperiodic signal is clearly defined away from dislocations, and can be correlated with other features. Similar ideas have been used in relation to vortex shedding and atmospheric oscillations.

Selective Filtering. Complementing the above viewpoint, the wavelet coefficients excluding the modulated oscillation can be retained, and the inverse Morlet transform removes the oscillation from the signal. A similar procedure has been carried out to characterize background turbulence as distinct from coherent structures. The result is shown on Fig. 22.39. The higher-frequency wave packet, the isolated bumps, and the noise are left intact, and only the faintest trace of the main oscillation is observed in the filtered signal. The difference on the time trace is not huge (weaker low frequencies between times $t = 15$ and 35, and the weaker bump at $t = 6$, are the more visible differences), but is quite clear on the Mexican-hat wavelet transform compared with Fig. 22.27.

This filtered signal can be treated as any signal, and its Mexican-hat wavelet transform is also shown on Fig. 22.39. The isolated events, notably the discontinuity at $t = 34$, stand out. Several points are illustrated in this context.

1. The selective removal of groups of wavelet coefficients meeting specific criteria designed by the analyst amounts to local surgery on the signal.
2. Because of their different shapes, the Morlet and Mexican-hat wavelets emphasize different features (local periodicity and isolated extrema, respectively). Other wavelets can be used, e.g., for edge detection.
3. Physical events (e.g., the discontinuity at time $t = 34$) can be multiscale events, extending spectrally over several orders of magnitudes; conversely, events of similar shape, location and/or scale (as were seeded in our signal on Fig. 22.26) may not have distinct wavelet signatures. Spectrally or temporally overlapping groups of coefficients should not be interpreted as indicative of distinct physical objects without corroborating additional insight specific to the signal at hand.

Several filtering variants can extract coherent structures. In addition to the denoising approach mentioned above, several wavelet-based eduction schemes have been used successfully. One example is shown in Fig. 22.40 [22.99], for the decomposition of the vector field in a mixing layer into coherent eddies and unstructured turbulence. In this case, both coherent and unstructured fields carried a significant fraction of the turbulent energy and of the turbulent stresses.

Conditional Spectra. Statistics such as energy or kurtosis provide a global summary of the data. Conditional statistics do the same for any subset of the data that meets user-defined criteria. This approach has been used in the case of unsteady flows encountered in turbomachinery, where periodic wake passing affects the boundary-layer development and transition and the relevant turbulent time scales. Similar steps are taken here with our test

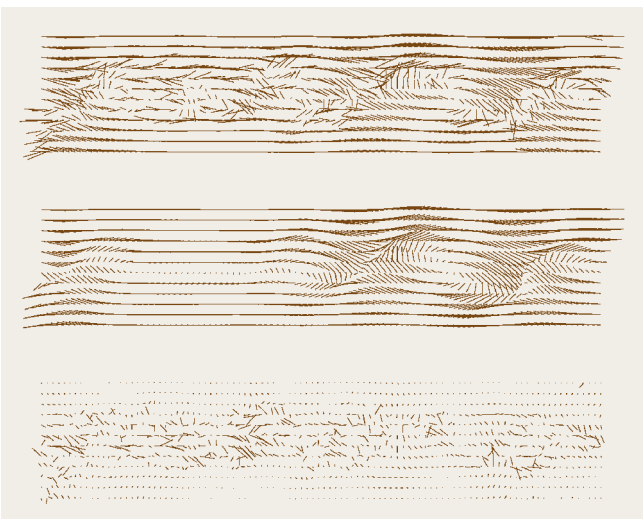

Fig. 22.40 A velocity field in a turbulent mixing layer (*top*), and its decomposition into intermittent coherent (*middle*) and unstructured fluctuations (*bottom*) (after [22.99])

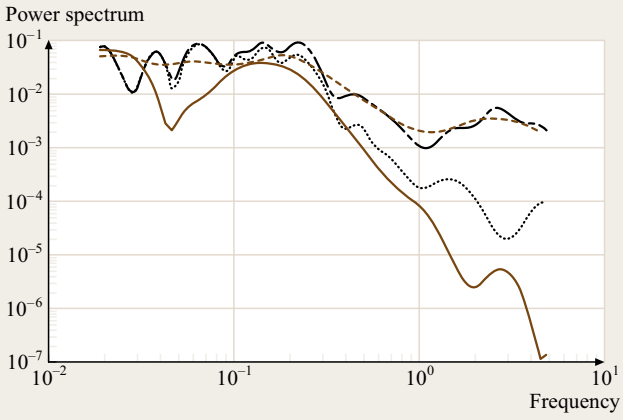

Fig. 22.41 Conditional power spectra over the first 15 units of test data, separating the contributions from data with the phase of the modulated oscillation between $-\pi/5$ and $\pi/5$ ('part 1'), and the other phases ('part 2'). Mexican hat spectrum of part 1 (*dashed line*) and part 2 (*solid line*); Morlet spectrum of part 1 (*dash-dot line*) and part 2 (*dotted line*)

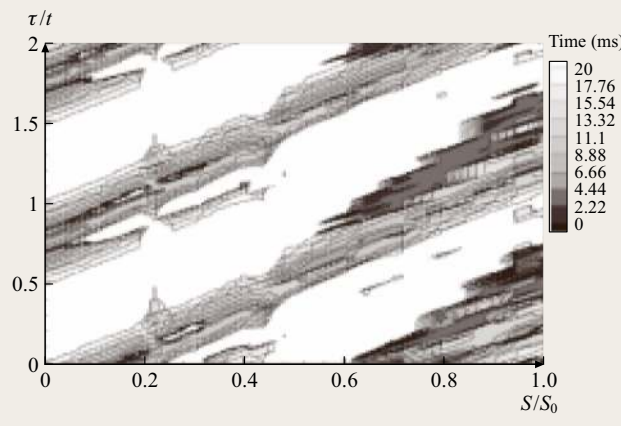

Fig. 22.42 Dominant time scales of unsteady turbulence triggered in the boundary layer over a curved plate by periodic wakes; s/s_0 is the dimensionless chord coordinate; time is nondimensionalized with the wake-passing half-period (after [22.100])

data. We restrict the computation of mean spectra to the filtered signal (Fig. 22.39) subject to the condition that the phase of the modulated oscillations over the first 15 s of data is between $-\pi/5$ and $\pi/5$ (Fig. 22.38), called part 1; other phases in the same time span contributed to part 2. For comparison, all spectra are normalized to a unit time of their respective samples. A statistical quantity of interest might be the dominant time scale (peak of compensated spectrum) associated with the condition. Note that the (phase-related) condition and the (energy-related) statistic can be obtained with different wavelet transforms.

The result is shown in Fig. 22.41. As far as determining the dominant frequencies of part 1 of the signal, the Mexican-hat and Morlet spectra agree both for the low-frequency and noisy contributions, separated by a spectral gap. For part 2 of the signal, they also concur that there is no noise. This might serve as an indication that noise is triggered in some way by the modulated oscillation, or that they have a common driving mechanism. However, one should be careful that conditional statistics imply the use of an indicator function (value 1 when the conditioning criterion is met, 0 otherwise), which introduces a cone of influence for each transition. Therefore, quantitative spectral statistics would be accurate only at frequencies higher than the dominant frequencies of the indicator function.

These ideas have been implemented in the study of unsteady boundary-layer transition (Fig. 22.42) [22.100]. The wakes of guide vanes are experienced as nearly periodic disturbances traveling along the rotor blade surfaces, triggering transition. The characterization of three types of turbulence (between wakes, in wakes, and in the boundary layer) evolving along the blade surface, could lead to better models of these complex flows.

Further Applications

Some general applications of wavelets overlap partially with fluid dynamics, and can be mentioned briefly.

Multidimensional Wavelets. Beyond time series, experimental and numerical data fields can be multidimensional, in space (e.g., PIV data) or space and time. Multidimensional wavelet analysis has been used in this context, and examples were presented above. Distinct transforms are normally executed in space and time; for 2-D or 3-D fields, multidimensional wavelets have been used successfully. They can be constructed as tensor products of one-dimensional wavelets, or as derivatives of multidimensional (sometimes anisotropic) filters. They have been successfully applied to the study of scaling in isotropic turbulence, of anisotropy in turbulent shear flows, to the eduction of coherent structures in 2-D and 3-D numerical data, among others. Generally speaking, many tools developed in the image processing literature are potentially relevant.

Denoising. Denoising has been used to separate unstructured turbulence (the noise) from the coherent structures. In this context, noise is not necessarily a loss in signal

quality due to extraneous random interference. Depending on the context, the noise may be undesirable or physically relevant: what matters here is that the two contributions to the signal have different wavelet signatures, either locally (e.g., the magnitude of the wavelet coefficients) or statistically (e.g., Gaussian energy distribution). Denoising is one particular instance of nonlinear filtering.

Denoising and two-dimensional fields are combined in Fig. 22.43. PIV data in the near wake of a circular disk normal to the uniform flow were obtained in an axial plane, and the tangential vorticity was calculated by finite difference. The combination of experimental and numerical noise can be alleviated by denoising. The orthogonal wavelet denoising scheme [22.98] has been adapted to the Mexican-hat wavelet, resulting in the vorticity distribution shown on Fig. 22.43.

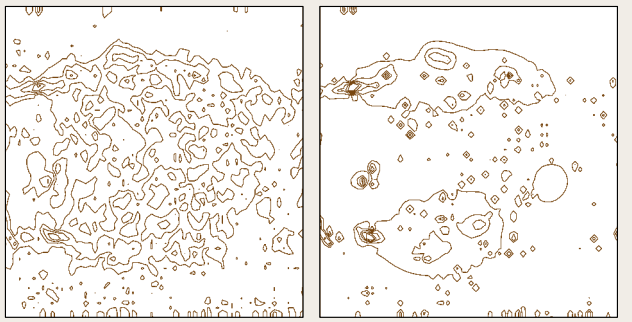

Fig. 22.43 Contour lines of instantaneous tangential vorticity in an axial section of the wake behind a circular disk, calculated from PIV data. *Right*: raw data; *left*: after continuous wavelet denoising; the same contour levels are used for both plots (data courtesy of H. Higuchi and R. P. Bigger)

Data Compression. Most of the energy of the signal is concentrated in a relatively small number of wavelet coefficients, as seen on Fig. 22.32. Independently of the context-dependent interpretation of energetic events as coherent structures, as in POD (Sect. 22.5), the remaining weak fluctuations may be ignored or modeled to yield a lower-dimensional system. Further economy of representation is achieved by keeping only modulus-maxima lines (the skeleton, without the surrounding *flesh*). Because of the commercial impact for data storage and transmission, this subfield has evolved very rapidly. Dynamical system modeling based on modulus maxima may be achievable.

Detection of Transitions. Transitions come in various guises, and several options should be considered. The asymmetric first derivative of a Gaussian (related to the Mexican hat, which is the second derivative) has been used for edge detection; in nearly periodic signals, phase dislocations (Morlet) have also been used successfully. The image-processing literature is too extensive to cite.

Resolution of Singularities, Fractal Signals. The ability of wavelets to zoom into ever-smaller domains of the signal can also be used to characterize singularities. It has been shown that the scaling exponent of the wavelet coefficients is related to the strength of the singularity.

Additional Remarks. Nonuniform sampling intervals in time series complicate the use of fast algorithms for wavelet transforms. As for Fourier processing, methods such as interpolation and resampling can be used.

As a pattern-recognition technique, the use of a single wavelet shape and simple algorithms is usually not satisfactory, because the value of the wavelet coefficients is determined not only by the shape, but also the amplitude of fluctuations. Some successful applications are emerging in the flow control area. While wavelets are usually too simple to serve as pattern-recognition tools, a collection of wavelet-based diagnostics can decrease the number of false-positive matches. Neural nets have been used to process multiple wavelet-based criteria, and applications to fluid mechanics appear likely in the future.

References

22.1 S.L. Marple Jr.: *Digital Spectral Analysis* (Prentice-Hall, Englewood Cliffs 1987)

22.2 J.S. Bendat, A.G. Piersol: *Random Data: Analysis and Measurement Procedures* (Wiley, New York 1986)

22.3 J.L. Lumley: The structure of inhomogeneous turbulence. In: *Atmospheric Turbulence and Wave Propagation*, ed. by A.M. Yaglom, V.I. Tatarski (Nauka, Moscow 1967) pp. 166–178

22.4 A.A. Townsend: *The Structure of Turbulent Shear Flow*, 2nd edn. (Cambridge Univ. Press, Cambridge 1976)

22.5 R. Adrian, J.P. Bonnet, J. Delville, F. Hussain, J. Lumley, O. Metais, C. Vassilicos: *CISM/ERCOFTAC*

Advanced Course: Eddy Structure Identification Techniques in Free Turbulent Shear Flows (Springer, Berlin, Heidelberg 1996)
22.6 J.L. Lumley: *Stochastic Tools in Turbulence* (Academic, New York 1970)
22.7 D.D. Kosambi: Statistics in function space, J. Indian Math. Soc. **7**, 76–88 (1943)
22.8 M. Loève: Fonctions aléatoires du second ordre, Comptes Rend. Acad. Sci. **220**, 295–300 (1945)
22.9 M. Loève: *Probability Theory* (Van Nostrand, New York 1955)
22.10 K. Karhunen: Zur Spektraltheorie stochastischer Prozesse, Ann. Acad. Sci. Fenn. A1 **34**, 1–7 (1946), in German
22.11 V.S. Pougachev: General theory of the correlations od random functions, Izv. Akad. Nauk. SSSR Mat. **17**, 401–402 (1953)
22.12 A.M. Obukhov: Energy distribution in the spectrum of a turbulent flow, Izv. A. N. SSSR Geogr. Geophys. **4–5**, 453–466 (1941)
22.13 A.M. Obukhov: Statistical description of continuous fields, Trudy Geophys. Int. Akad. Nauk. SSSR **24**, 3–42 (1954)
22.14 I.T. Joliffe: *Principal Component Analysis* (Springer, New York 1986)
22.15 H. Hotelling: Analysis of a complex statistical variables into principal components, J. Educ. Psychol. **24**, 417–441 (1933)
22.16 G.H. Golub, C.F. Van Loan: *Matrix Computations*, 2nd edn. (Johns Hopkins Univ. Press, Baltimore 1990)
22.17 A. Papoulis: *Probability, Random variables, and Stochastic Processes* (McGraw-Hill, New York 1965)
22.18 M. Kirby, L. Sirovich: Application of the Karhunen–Loève procedure for the characterization of human faces, IEEE T. Pattern Anal. **12**(1), 103–108 (1990)
22.19 V.R. Algazi, D.J. Sakrison: On the optimality of the Karhunen–Loève expansion, IEEE Trans. Inform. Theory **15**, 319–321 (1969)
22.20 C.A. Andrews, J.M. Davies, G.R. Schwartz: Adaptative data compression, Proc. IEEE **55**, 267–277 (1967)
22.21 S.S. Ravindran: Reduced-order adaptive controllers for fluid flows using POD, J. Sci. Comput. **15**(4), 457–478 (2000)
22.22 S.S. Ravindran: A reduced-order approach for optimal control of fluids using proper orthogonal decomposition, Int. J. Numer. Meth. Fluids **34**, 425–448 (2000)
22.23 R. Courant, D. Hilbert: *Methods of Mathematical Physics*, Vol. 1 (Wiley, New-York 1953)
22.24 P. Holmes, J.L. Lumley, G. Berkooz: *Turbulence, Coherent Structures, Dynamical Systems and Symmetry, Cambridge Monographs on Mechanics* (Cambridge Univ. Press, Cambridge 1996)
22.25 J. Delville, L. Ukeiley, L. Cordier, J.-P. Bonnet, M. Glauser: Examination of large-scale structures in a turbulent mixing layer, Part 1. Proper orthogonal decomposition, J. Fluid Mech. **391**, 91–122 (1999)
22.26 S. Gordeyev: *Investigation of coherent structure in the similarity region of the planar turbulent jet using POD and wavelet analysis*, Ph.D. Dissertation (University of Notre Dame, Notre Dame 1999)
22.27 J.-P. Bonnet, J. Delville: Coherent structures in turbulent flows and numerical simulations approaches. In: *Lecture Series 2002-04 on Post-Processing of Experimental and Numerical Data*, ed. by P. Millan, M.L. Riethmuller (Von Karman Institute for Fluid Dynamics, Bruscelles 2002)
22.28 H.E. Fiedler: Control of free turbulent shear flows. In: *Flow Control: Fundamental and Practices*, Lecture Notes Phys., Vol. 53, ed. by M. Gad-el-Hak, A. Pollard, J.-P. Bonnet (Springer, Berlin, Heidelberg 1998) pp. 336–429
22.29 N. Aubry, P. Holmes, J.L. Lumley, E. Stone: The dynamics of coherent structures in the wall region of a turbulent boundary layer, J. Fluid Mech. **192**, 115–173 (1988)
22.30 L. Ukeiley, L. Cordier, R. Manceau, J. Delville, M. Glauser, J.-P. Bonnet: Examination of large-scale structures in a turbulent mixing layer, Part 2. Dynamical systems model, J. Fluid Mech. **441**, 67–108 (2001)
22.31 L. Cordier, M. Bergmann: Two typical applications of POD: Coherent structures eduction and reduced order modelling. In: *Lecture Series 2002-04 on Post-Processing of Experimental and Numerical Data*, ed. by P. Millan, M.L. Riethmuller (Von Karman Institute for Fluid Dynamics, Bruscelles 2002)
22.32 M. Hinze: *Optimal and instantaneous control of the instationary Navier–Stokes equations, Accreditation to supervise research dissertation* (Berlin University, Berlin 2000)
22.33 S. Volkwein: *Optimal and suboptimal control of partial differential equations: Augmented Lagrange-SQP methods and reduced order modeling with proper orthogonal decomposition, Accreditation to supervise research dissertation* (Graz University, Graz 2001)
22.34 M. Fahl: *Trust-Region methods for flow control based on reduced order modeling*, Ph.D. Dissertation (Trier University, Trier 2000)
22.35 M. Bergmann, L. Cordier, J.-P. Brancher: Optimal rotary control of the cylinder wake using POD reduced order model, Phys. Fluids **17**(9), 1–21 (2005)
22.36 A. Chatterjee: An introduction to the proper orthogonal decomposition, Curr. Sci. **78**(7), 808–817 (2000)
22.37 T.J. Rivlin: *An Introduction to the Approximation of Functions* (Dover, New York 1981)
22.38 N.J. Higham: Matrix nearness problems and applications. In: *Applications of Matrix Theory*, ed. by M.J.C. Glover, S. Barnett (Clarendon, Oxford 1989) pp. 1–27

22.39 L. Hubert, J. Meuleman, W. Heiser: Two purposes for matrix factorization: A historical appraisal, SIAM Rev. **42**, 68–82 (2000)

22.40 J.A. Atwell, B.B. King: Reduced order controllers for spatially distributed systems via proper orthogonal decomposition, Virginia Tech. ICAM **99-07-01** (1999)

22.41 S. Volkwein: *Proper Orthogonal Decomposition and Singular Value Decomposition, Tech. Rep. Institut für Mathematik 153* (Graz University, Graz 1999)

22.42 E. Anderson, Z. Bai, C. Bischof, S. Blackford, J. Demmel, J. Dongarra, J. Du Croz, A. Greenbaum, S. Hammerling, A. McKenney, D. Sorensen: LAPACK User's Guide (SIAM third edn. 1999)

22.43 N. Aubry: On the hidden beauty of the proper orthogonal decomposition, Theor. Comp. Fluid Dyn. **2**, 339–352 (1991)

22.44 E.A. Christensen, M. Brøns, J.N. Sørensen: *Evaluation of POD-based decomposition techniques applied to parameter-dependent non turbulent flows, DCAMM Rep. 573* (Technical University of Denmark, Arhus 1998)

22.45 G. Berkooz: *Turbulence, coherent structures, and low dimensional models*, Ph.D. Dissertation (Cornell University, Ithaca 1991)

22.46 F. Riesz, B.S. Nagy: *Functional Analysis* (Ungar, New York 1955)

22.47 G. Berkooz, P. Holmes, J.L. Lumley: The proper orthogonal decomposition in the analysis of turbulent flows, Annu. Rev. Fluid Mech. **25**, 539–575 (1993)

22.48 D. Rempfer, H.F. Fasel: Evolution of three-dimensional coherent structures in a flat-plate boundary layer, J. Fluid Mech. **260**, 351–375 (1994)

22.49 S. Sanghi: *Mode interaction models in near-wall turbulence*, Ph.D. Dissertation (Cornell University, Ithaca 1991)

22.50 R. Temam: *Infinite-Dimensional Dynamical Systems in Mechanics and Physics* (Springer, New York 1988)

22.51 A.C. Antoulas, D.C. Sorensen: *Approximation of Large-Scale Dynamical Systems: An Overview, Tech. Rep.* (Rice University, Houston 2001)

22.52 B.G. Allan: *A reduced order model of the linearized incompressible Navier–Stokes equations for the sensor/actuator placement problem, ICASE Rep. 2000-19* (NASA, Washington 2000)

22.53 N. Aubry, R. Guyonnet, R. Lima: Spatio-temporal analysis of complex signals: Theory and applications, J. Stat. Phys. **64**(3/4), 683–739 (1991)

22.54 J. Delville, L. Cordier, J.-P. Bonnet: Large-scale structure identification and control in turbulent shear flows. In: *Flow Control: Fundamental and Practices*, Lecture Notes Phys., Vol. 53, ed. by M. Gad-el-Hak, A. Pollard, J.-P. Bonnet (Springer, Berlin, Heidelberg 1998) pp. 199–273

22.55 M. Rathinam, L.R. Petzold: A new look at proper orthogonal decomposition, SIAM J. Numer. Anal. **41**(5), 1893–1925 (2001)

22.56 W.R. Graham, J. Peraire, K.Y. Tang: Optimal control of vortex shedding using low order models, Part 1: Open-loop model development, Int. J. Numer. Meth. Eng. **44**(7), 945–972 (1999)

22.57 J. Burkardt, M.D. Gunzburger, H.-C. Lee: *Centroidal Voronoi Tessellation-Based Reduced-Order Modeling of Complex Systems, Tech. Rep.* (Florida State University, Tallahassee 2004)

22.58 A. Iollo: Remarks on the approximation of the Euler equations by a low order model, INRIA Res. Rep. **3329**, 1–28 (1997)

22.59 A. Iollo, S. Lanteri, J.-A. Désidéri: Stability properties of POD-Galerkin approximations for the compressible Navier–Stokes equations, INRIA Res. Rep. **3589**, 1–30 (1998)

22.60 C.W. Rowley: *Modeling, simulation and control of cavity flow oscillations*, Ph.D. Dissertation (California Institue of Technology, Pasadena 2002)

22.61 R.B. Lehoucq, D.C. Sorensen, C. Yang: ARPACK Users' Guide: Solution of Large-Scale Eigenvalve Problems with Implicity Restarted Arnoldi Methods (SIAM 1998)

22.62 L. Sirovich: Turbulence and the dynamics of coherent structures, Part 1: Coherent structures, Q. Appl. Math. **45**(3), 561–571 (1987)

22.63 L. Sirovich: Turbulence and the dynamics of coherent structures, Part 2: Symmetries and transformations, Q. Appl. Math. **45**(3), 573–582 (1987)

22.64 L. Sirovich: Turbulence and the dynamics of coherent structures, Part 3: Dynamics and scaling, Q. Appl. Math. **45**(3), 583–590 (1987)

22.65 L. Cordier: *Etude de systèmes dynamiques basés sur la décomposition orthogonale aux valeurs propres (POD), Application à la couche de mélange turbulente et à l'écoulement entre deux disques contra-rotatifs*, Ph.D. Dissertation (Poitiers University, Poitiers 1996)

22.66 S. Herzog: *The large scale structure in the near-wall of turbulent pipe flow*, Ph.D. Dissertation (Cornell University, Ithaca 1986)

22.67 P. Moin, R.D. Moser: Characteristic-eddy decomposition of turbulence in a channel, J. Fluid Mech. **200**, 471–509 (1989)

22.68 J. Delville: Characterization of the organization in shear layers via the proper orthogonal decomposition, Appl. Sci. Res. **53**, 263–281 (1994)

22.69 J.P. Bonnet, D. Cole, J. Delville, M. Glauser, L. Ukeiley: Stochastic estimation and proper orthogonal decomposition: Complementary techniques for identifying structures, Exp. Fluids **17**, 307–314 (1994)

22.70 C.A.J. Fletcher: *Computational Techniques for Fluid Dynamics* (Springer, New York 1991)

22.71 D. Rempfer: Investigations of boundary layer transition via Galerkin projections on empirical eigenfunctions, Phys. Fluids **8**(1), 175–188 (1996)

22.72 R.D. Joslin, M.D. Gunzburger, R.A. Nicolaides, G. Erlebacher, M.Y. Hussaini: A self-contained, automated methodology for optimal flow control

validated for transition delay, ICASE Rep. **95-64**, 1–31 (1995)
22.73 J.O. Hinze: *Turbulence*, 2nd edn. (McGraw-Hill, New York 1975)
22.74 S. Sirisup, G.E. Karniadakis: A spectral viscosity method for correcting the long-term behavior of POD model, J. Comp. Phys. **194**, 92–116 (2004)
22.75 B.R. Noack, P. Papas, P.A. Monkewitz: The need for a pressure-term representation in empirical Galerkin models of incompressible shear flows, J. Fluid Mech. **523**, 339–365 (2005)
22.76 B. Galletti, A. Bottaro, C.-H. Bruneau, A. Iollo: Accurate model reduction of transient and forced wakes, Eur. J. Mech. B **26**(3), 354–366 (2007)
22.77 P. Sagaut: *Large-Eddy Simulation for Incompressible Flows – An Introduction* (Springer, Berlin, Heidelberg 2005)
22.78 G.S. Karamanos, G.E. Karniadakis: A spectral vanishing viscosity method for large eddy simulations, J. Comp. Phys. **162**, 22–50 (2000)
22.79 M. Bergmann: *Optimisation aérodynamique par réduction de modèle POD et contrôle optimal, Application au sillage laminaire d'un cylindre circulaire*, Ph.D. Dissertation (Institut National Polytechnique de Lorraine, Nancy 2004)
22.80 M. Couplet, C. Basdevant, P. Sagaut: Calibrated reduced-order POD-Galerkin system for fluid flow modelling, J. Comp. Phys. **207**, 192–220 (2005)
22.81 J. Borée: Extended proper orthogonal decomposition: A tool to analyse correlated events in turbulent flows, Exp. Fluids **35**, 188–192 (2003)
22.82 R.J. Adrian: On the role of conditional averages in turbulence theory. In: *Turbulence in Liquids*, ed. by G. Patterson, J. Zakin (Science, Princeton 1977) pp. 322–332
22.83 R.J. Adrian: Conditional eddies in isotropic turbulence, Phys. Fluids **22**, 2065–2070 (1979)
22.84 R.J. Adrian, P. Moin: Stochastic estimation of organized turbulent structure: Homogeneous shear flow, J. Fluid Mech. **190**, 531–559 (1988)
22.85 A. Papoulis: *Probability, Random Variables and Stochastic Theory*, 2nd edn. (McGraw-Hill, New York 1984)
22.86 R. Deutsch: *Estimation Theory* (Prentice-Hall, New York 1965) p. 269
22.87 R.J. Adrian, B.G. Jones, M.K. Chung, Y. Hassan, C.K. Nithianandan, A.T.C. Tung: Approximation of turbulent conditional averages by stochastic estimation, Phys. Fluids A **1**, 992–998 (1989)
22.88 D.R. Cole, M.N. Glauser, Y.G. Guezennec: An application of the stochastic estimation to the jet mixing layers, Phys. Fluids A **4**, 192 (1992)
22.89 T.C. Tung, R.J. Adrian: Higher-order estimates of conditional eddies in isotropic turbulence, Phys. Fluids **23**, 1469–1470 (1980)
22.90 H.L. Pécseli, J. Trulsen: A statistical analysis of numerically simulated plasma turbulence, Phys. Fluids B **1**, 1616–1636 (1989)
22.91 Y.G. Guezennec: Stochastic estimation of coherent structure in turbulent boundary layers, Phys. Fluids A **1**, 1054 (1989)
22.92 G.J. Brereton: Stochastic estimation as a statistical tool for approximating turbulent conditional averages, Phys. Fluids A **4**, 1046–2054 (1992)
22.93 T.G. Bagwell, R.J. Adrian, R.D. Moser, J. Kim: Improved approximation of wall shear stress boundary conditions for large eddy simulations. In: *Near Wall Turbulent Flows*, ed. by R. So, C.B. Speziale, B.E. Launder (Elsevier, Amsterdam 1993) pp. 265–275
22.94 I. Daubechies: *Ten Lectures on Wavelets* (SIAM, 1992)
22.95 M. Farge: Wavelet transforms and their applications to turbulence, Annu. Rev. Fluid Mech. **24**, 395–457 (1992)
22.96 S. Mallat: *A Wavelet Tour of Signal Processing* (Academic, San Diego 1998)
22.97 J.C. van den Berg (Ed.): *Wavelets and Physics* (Cambridge Univ. Press, Cambridge 1999)
22.98 D. Donoho, M.R. Duncan, X. Huo, O. Levi: Wavelab, http://www-stat.stanford.edu/ wavelab (1999)
22.99 J. Lewalle, J. Delville, J.P. Bonnet: Decomposition of Mixing Layer Turbulence in coherent structures and background fluctuations, Flow Turb. Comb. **64**, 301–328 (2000)
22.100 M.T. Schobeiri, K. Reid, J. Lewalle: Effect of unsteady wake passing frequency on boundary layer transition, experimental investigation and wavelet analysis, J. Fluids Eng. **125**, 251–266 (2003)